2017

Computational Fluid Dynamics Proof of Concept and Analysis of a Self-Powered Fontan Circulation

Marcus Ni
University of Central Florida

COMPUTATIONAL FLUID DYNAMICS PROOF OF CONCEPT AND ANALYSIS OF A SELF-POWERED FONTAN CIRCULATION

by
MARCUS NI

B.S. University of Central Florida, 2012
M.S. University of Central Florida, 2013

A dissertation submitted in partial fulfillment of the requirements
for the degree of Doctor of Philosophy
in the Department of Mechanical and Aerospace Engineering
in the College of Engineering and Computer Science
at the University of Central Florida
Orlando, Florida

Spring Term
2017

Major Professor: Alain J. Kassab

ABSTRACT

The Fontan circulation is a result of the last (third stage) surgical procedure to correct a single ventricle congenital cardiac disorder in children. Although the Fontan circulation has been successfully established in surgeries over the years, it is flawed and can lead in certain cases to pre-mature death. The main cause of this failure is due to increased pulmonary vascular resistance due to loss pulse pressure and blood flow. In healthy circulations, the heart pumps directly to the lungs, where as “Single Ventricle” patients must use a single sided heart to supply blood to the rest of the body before the lungs. Improvements to the Fontan circulation have been proposed, but they require extensive care or external devices. We propose a “Self-Powered” Fontan circulation that will inject energy into the pulmonary system by adding an injection jet shunt (IJS) directly from the heart. The IJS will provide the pulse pressure, blood flow, and entrainment that the pulmonary vascular system needs to function at a healthy level. The difference between a healthy and sick Fontan circulation is 3-5[mmHg] in the IVC. The goal of the IJS is to cause this 3-5[mmHg] pressure drop in the IVC. In the analysis of the Fontan, ascertaining energy losses due to flow jet impingements and flow mixing is critical. Moreover, in order to better understand surgical alternatives is it important to have a robust multi-scale 0D-3D CFD analysis tool that permits investigation of surgical alternatives in a virtual physics-based environment. To this end, a lumped parameter model (LPM) is tightly coupled at the time step level with a full 3D computational fluid dynamics (CFD) model. Using this model scheme, the Fontan test section is no longer being modeled by the LPM. Therefore, it is not limited by the 0D nature of the vascular resistance, capacitance, and inertia bed model. The CFD can take over at the area of interest which accounts for flow directionality and momentum transfer that the LPM is unable to capture. To efficiently calculate optimal IJS configurations, a closed loop steady state model was created to solve a simplified

Fontan circulation in 3D. Three models were created with several different optimized configurations, a synthetic model (average dimensions of 2-4 year-old Fontan patients), and two patient-specific models (10 and 24-year-old). The model configurations include changes in the IJS nozzle diameter and IJS placement along the pulmonary artery. These configurations are compared to a baseline model with no IJS. All three models suggest that the IJS helps to decrease IVC pressure while increasing pulse pressure and blood flow to the pulmonary system.

ACKNOWLEDGMENTS

Funded by the American Heart Association (AHA).

I would like to thank all my colleagues for all the contributions they made to this project. Rachel Quinn and Giovanna Rodriguez for the extraction of CHOP patient data from MRI scans. Nicolas Voce for his help with developing the ODE solver. Ray Prather for all his helpful insight and engineering knowledge that helped me solve this difficult problem. He would, on many occasions, stop his computational simulations so that I could run my own. Dr. Eduardo Divo for his influence in my decision to pursue a Ph.D. at UCF, and for his seemingly unmatched knowledge in his fields of research. Dr. William DeCampli for bringing this theoretical surgical approach to our research group and for his continued support in solving this complicated bio-engineering problem.

I would also like to thank my beautiful wife Madeleine Ni, my newborn son Jace Ni, my mother April Balmer, and the rest of my family for their unconditional love and support that gave me the drive to complete my greatest accomplishment thus far.

Last, but certainly not least, I would like to thank my dissertation advisor, Dr. Alain Kassab, for this incredible opportunity to work as his research assistant during my time at UCF. His guidance for all my research projects has been unmatched. His availability was unwavering, he always made time to help me with my project design. He has been the most influential person in my life since the day I asked him about engineering research. None of my academic achievements would have been possible without his influence and guidance. I strive to reach his level of excellence every day, and I look forward to continuing this effort. Thank you so very much!

TABLE OF CONTENTS

LIST OF FIGURES

LIST OF TABLES

LIST OF ACRONYMS / ABBREVIATIONS

BPM	Beats per Minute
C	Capacitance
CFD	Computational Fluid Dynamics
CHD	Congenital Heart Disease
CHOP	Children's Hospital of Philadelphia
CMA	Central Moving Average
CO	Cardiac Output
E	Energy
ECFO	Extracardiac Fontan Operation
EDP	End Diastolic Pressure
ESP	End Systolic Pressure
FP	Flow Pulsatility
FPS	Frames per Second
ICPC	Inferior Cavopulmonary Connection
IJS	Injection Jet Shunt
IVC	Inferior Vena Cava
L	Inductance
LPA	Left Pulmonary Artery
LPM	Lumped Parameter Model
MG	Momentum Gained
MR	Momentum Ration
NC	Noise Canceling
NES	No Entrainment Shunt
ODE	Ordinary Differential Equations
PA	Pulmonary Artery
PAP	Pulmonary Arterial Pressure
Po	Total Pressure
PP	Pressure Pulsatility
Ps	Static Pressure
PulP	Pulse Pressure
PVR	Pulmonary Vascular Resistance
Qp	Pulmonary Flow
Qs	Systemic Flow
R	Resistance
RPA	Right Pulmonary Artery
RVS	Right Ventricular Shunt
SCPC	Superior Cavopulmonary Connection
SVC	Superior Vena Cava
SVR	Systemic Vascular Resistance
TCPC	Total Cavopulmonary Connection
V	Velocity

CHAPTER 1: INTRODUCTION

The proposed project is at the interface of medicine and engineering and brings together computational fluid dynamics (CFD) and multi-scale modeling to analyze the hemodynamics of a proposed "self-powered" Fontan circulation, one driven by the functioning single ventricle itself, in patients with single ventricle congenital heart disease (CHD). "Single ventricle" anomalies account for one fourth of all congenital cardiac disorders. Not only is the mortality rate high, 50% by 20 years of age, the quality of life is quite low and the heath care expenses are unmanageable[1][2]. The Fontan circulation is established in the last (third stage) surgical procedure to correct a single ventricle CHD in children.

Although the Fontan circulation has been successfully established in surgeries over the years, it is flawed and can lead, in certain cases, to pre-mature death. Multiple causes of failure include **(1)** intrinsic ventricular dysfunction **(2)** elevated pulmonary vascular resistance, or **(3)** elevated inferior vena cava (IVC) pressure. These conditions lead to liver cirrhosis, protein-losing enteropathy, or plastic bronchitis [26][27][28]. In healthy circulations, the heart pumps directly to the lungs, whereas "Single Ventricle" patients must use a single sided heart to supply blood to the rest of the body with blood returning passively to the lungs driven by the global systemic pressure.

Many improvements to the Fontan circulation have been proposed, some design parameters include inferior cavopulmonary connection (ICPC) diameter and location, Y shaped ICPC, Glenn optimizations (Hemi-Fontan) [4][5][6][7][47][49]. These methods improve upon the original Fontan surgery, but do not significantly lower venus pressures in the lower bed. Mechanical assist devices that are designed to power the pulmonary system have also been proposed [39][40][41][42][43][61]. Theoretical mechanical applications have all been successful in dropping the IVC pressure back to

normal healthy values, about 8[mmHg], but there are issues. Some of the current issues include: **(1)** pumping happens in one direction only, **(2)** sometimes requires two pumps, **(3)** causes re-circulations induced by barriers, **(4)** suction at the pump inlet can cause collapse, **(5)** some are obstructive, and **(6)** they can't be shut off. These issues can lead to driveline infection, pulmonary embolisms, or even stroke if there is a fenestration present [39]. Benchtop and computational models of the Norwood and Glenn operations have also been presented in an attempt to further improve both the palliations [1][2][15][16][17][18][22][45][46][55].

An alternative solution is to inject energy into the Fontan system by tapping into the reserve mechanical energy of the native heart, a "self-powered Fontan". A simple modification is to place a shunt (injection jet shunt, IJS) leading from the aorta to the Fontan conduit, shown in Figure 1. In the analysis of the Fontan, ascertaining energy losses due to flow jet impingements and flow mixing is critical. Moreover, to understand surgical alternatives it is important to have a robust multi-scale 0D-3D CFD analysis tool that permits investigation of surgical planning in a virtual physics-based environment. To this end, a lumped parameter model (LPM) is tightly coupled at the time-step level with a full 3D CFD model. With this scheme, the total cavopulmonary connection (TCPC) is no longer modeled by the 0D LPM. CFD can resolve the area of interest, which accounts for flow directionality and momentum transfer that the LPM is unable to capture. Multi-scale models have been developed for the study of many hemodynamic applications. Hence, there has been several studies on the application of multi-scale models to these hemodynamic problems [14][19][20][21][23][48][56]. In the proposed IJS model, the pulmonary flow will be tuned to increase by 50%, which will have a direct effect on the pulmonary vascular resistance (PVR). Accurate PVR vs. flow models are not available because all existing studies include other responses. These include exercise[24][29][32][33][36][62] , oxygen inhalation [35][59], and

dobutamine stress[34]. Pulsatility, pulse pressure, and flow acceleration are also known to effect PVR [26][27][28][30][73]. The best available PVR model was extracted from the effect that dobutamine stress has on pulmonary flow [34]. Under low levels of dobutamine administration, PVR is not affected [57][58]. Unlike oxygen inhalation, which is known to cause the PVR to drop [59], and exercise, where PVR is directly affected by vasodilative chemicals (prostacyclin and nitric oxide) released by the pulmonary endothelium [29].

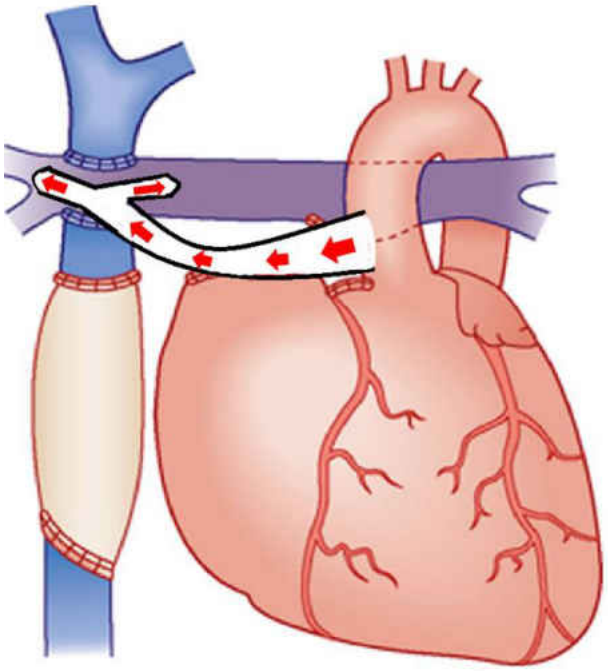

Figure 1: Injection Jet Shunt (IJS), Image Provided by Clinical Gate.

As a proof of concept, the IJS configuration was optimized to cause a maximized pressure drop at the IVC. Steady state studies were carried out in a CFD model that simplified the entire circulation system to quickly optimize nozzle diameter and nozzle location. These optimized IJS parameters were then implemented into 3 different models. A synthetic model, and two patient specific models. The synthetic model was built using average patient data [5][7][10][72], and the patient-specific models

were provided by the Children's Hospital of Philadelphia through MRI scans [53][54]. Baseline configurations were built for all three models which were tuned to the patient data. The TCPC pressure was then elevated to 16.5[mmHg] to simulate sick conditions for a Fontan circulation. These baseline models were then compared to several different optimized IJS configurations.

One of the most important requirements for this project was the ability for the multi-scale model to be used by the University of Central Florida for future research and advancements. A very thorough guide for the use and application of the multiscale model is provided, along with detailed model parameters. Solid model extraction, cluster use, and systematic instructions on how to set up the multiscale model are some of the inclusions.

CHAPTER 2: LITERATURE REVIEW

2.1 Fontan Circulation Behavior

The first successful Fontan operation was completed in 1968 [67], by Francis Fontan, to repair tricuspid atresia, which is a right ventricle malformation. In a Fontan circulation, the heart has one ventricle which pumps exclusively to the systemic circulation. The blood to pulmonary system flows passively at an elevated pressure [1][2][26]. The Fontan circulation has been successfully established in surgeries over the years, but it is flawed and can lead, in certain cases, to pre-mature death. Multiple causes of failure include intrinsic ventricular dysfunction, and elevated pulmonary vascular resistance. Secondary failure is elevated IVC pressure, which can cause liver cirrhosis, protein-losing enteropathy, and plastic bronchitis [38]. Despite major efforts to improve the palliation, survival rates have not significantly increased (1-2% between 2013 and 2015[28]).

Gewillig M. et al. [26][27][28][38] provided in depth knowledge of the Fontan circulation and its failures. The Fontan circulation creates abnormal operating conditions, which leads to underdevelopment of the pulmonary vasculature. PVR increases over time, which is attributed to lack of blood acceleration, lack of flow pulsatility, lack of cardiac through put with exercise, and overall pulmonary blood flow. Gewillig describes the pulmonary vasculature as a “dam” which needs to be addressed in sick Fontan patients. Fenestration is a method which bypasses the “dam” by returning IVC flow back to the right atrium. This improves cardiac output and reduces IVC flow congestion. However, oxygen saturation is decreased, and getting the right fenestration size has proven to be difficult. Too much return flow can cause high levels of cyanosis, and a fenestration that is too small may not reduce IVC congestion enough. Ventricular dysfunction is the other main failure component. Before the initial Norwood palliation, the ventricle is working 250% to 350% harder than a healthy patient. After the

Glenn, it goes down to 90%, and the Fontan further reduces workload to 50% to 80%. The initial development of the ventricle is overgrown, and is accustomed to seeing high preload. Once the Fontan palliation is applied, this overgrown ventricle is deprived of preload and will start to slowly decline along with cardiac output.

2.2 Multi-Scale Modeling Methods

CFD-LPM multi-scale models have been used to solve several different hemodynamic circulations. Quateroni et al. [14][20] provided the mathematical model required to solve these multi-scale models. Their iterative scheme has the LPM leading the CFD in time, and they focus on the Neuman boundary condition setup (pressures are passed to the CFD on all inlets and outlets). A tightly coupled multiscale model of a bifurcating vessel is provided as an example.

Esmaily-Moghadam et al.[56] go a step further by implementing different coupling boundary conditions (Neumann, Dirichlet, and mixed). The Dirichlet approach applies mass flows to all the CFD inlets and outlets. The mixed approach applies mass flows and pressures to the CFD boundaries. The Dirichlet approach is the least costly but loses information at the inlets due to velocity profile assumptions. Their coupled scheme had the CFD leading the LPM in time. Interface stability was achieved by designing the LPM to receive flows at capacitors and pressures at inductors.

Sankaran et al. [23] used a Neumann approach to model a patient specific aorta after bypass graft surgery. They developed an algorithm for choosing boundary condition parameters to match patient data, such as choosing capacitances that are proportional to the outlet areas, ($C \propto A$) [60].

Tightly coupled CFD-LPM multi-scale models are subject to backflow divergence issues at the coupled interface. Esmaily-Moghadam et al.[21] compared three different stabilization methods and made suggestions on improving them. Flow reversal is dictated by the pressure passed to the 3D model,

so these methods look to improve interface condition assumptions. The first stabilization method adds backflow stabilization terms for the Neumann boundaries. The second controls the velocity direction, and the third constrains velocity profiles using Lagrangian multipliers. Each method is effective, but there are problems with each model. Confining the velocity direction will directly affect the local flow field. The Lagrangian multipliers solve the local flow field disruption problem, but it is difficult to implement, tune, and requires more computation time. The outlet stabilization method can also alter local flow fields, but these alterations are shown to be minimal. For commercial CFD solvers, extending the model is the easiest form of backflow stabilization. Limitations include: **(1)** not being able to stabilize total flow reversal at the outlet, **(2)** the potential to change local hemodynamics, and **(3)** longer computation times due to extra meshing. To conclude, they found that the outlet stabilization method was the most robust, was the easiest to use, and required the lowest computational cost of the three methods tested. Esmaily-Moghadam et al. [19] also expand on these results by introducing a new preconditioning technique. This new stabilization technique reduces the computational cost and increases stability with different mesh sizes.

2.3 Norwood / Hybrid Norwood Modeling

Ceballos et al. [1] analyzed the hybrid Norwood procedure with distal aortic arch obstruction and a reverse-Blalock-Taussig shunt (RBTS) by using a loosely coupled LPM-CFD multi-scale model. They analyzed four models: with a 90% obstruction, without obstruction, with a RBTS, and without a RBTS. These studies found that the 4mm RTBS could compensate for 90% stenosis obstruction. Ceballos et al. [2] also analyzed the different effects that the RBTS diameter (3[mm], 3.5[mm], and 4[mm]) has on the Norwood hemodynamic circulation. Oxygen transport and oscillatory shear index was used to determine

that the 3.5[mm] RBTS was optimal. The 3.5[mm] RBTS had low shear rates compared to the 3[mm] and lower thrombosis risk than the 4[mm] model.

Bove et al. [16] compared the RBTS against right ventricle artery shunts (RVS) in Norwood circulations using CFD-LPM multi-scale modeling. They found that different RBTS diameter sizes negatively affected the hemodynamics more than the RVS diameters. Large RBTS diameters resulted in sick hemodynamic symptoms. RVS displayed adequate oxygen delivery for all diameters, and showed hemodynamic advantages over the RBTS. However, the damaging effects to the ventricle by implanting an RVS still need to be analyzed.

Hsia et al. [17] also compared RBTS and RVS approaches, along with hybrid Norwood applications. These models included an RBTS with a 3.5[mm] diameter, an RVS with a 5[mm] diameter, and a hybrid Norwood with a 7[mm] ductal stent and a 2[mm] pulmonary artery banding. The hybrid Norwood provided less oxygen to the systemic and cerebral beds, which suggests that the RBTS and RVS approaches should be preferred.

2.4 Glenn / Hemi-Fontan Modeling

Esmaily-Moghadam et al. [15] used multi-scale modeling to analyze an assisted bidirectional Glenn (ABG) circulation. The pulmonary system was assisted by attaching a shunt from the aorta to the SVC distal to the superior cavopulmonary connection (SCPC). A clip was applied to the shunt to cause a Ventruri effect within the shunt itself, proximal to the SVC. This assist shunt resulted in increased oxygen delivery, and increased ventricle workload, but caused SVC pressure to increase. Zhou et al. [66] validated these ABG computational models by analyzing the same circulation using an in vitro model (benchtop). They also found increased pulsatility, pulse pressure, pulmonary flow, and SVC pressure.

Shiavazzi et al. [18] used an LPM-CFD multi-scale model to simulate six patient-specific Glenn circulations with increasing levels of LPA stenosis. The LPM was tuned to match the image data from patients, and a 3D geometry was also extracted from this patient data. They applied increasing levels of stenosis to the LPA by using mesh morphing techniques. They recommended adding LPA arterioplasty to the SCPC procedure in patients with LPA stenosis above 65%.

The Hemi-Fontan is an alternative approach to the bidirection Glenn operation. Rather than disconnecting the SVC from the right atrium, the right atrium is reconstructed to attach to the pulmonary system. A baffle is used to redirect the SVC flow through this right atrium to pulmonary artery connection, displayed in Figure 2. Kung et al. [46] compared two patient specific cases of the Hemi-Fontan circulation using multi-scale modeling. They found that the same operation resulted in one of the patient models having 3 times the power loss than the other.

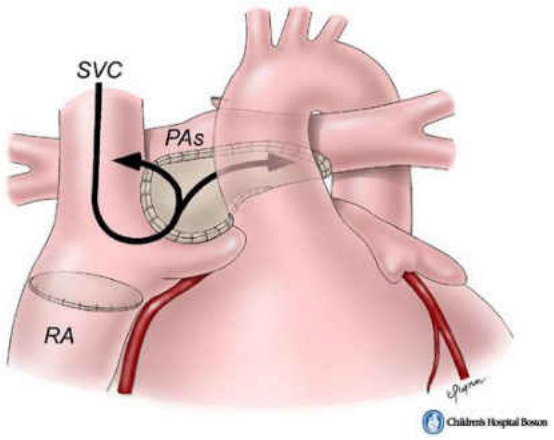

Figure 2: Hemi-Fontan Procedure. Picture Provided by Children's Hospital Boston.

2.5 Fontan Modeling

Alexi-Meskishvili et al. [4] performed a clinical study to determine the optimal Gore-Tex conduit size for extra cardiac Fontan operations (ECFO). They implanted different size diameter conduits in 20

patients, 1-16[mm], 3-18[mm], 8-20[mm], 5-22[mm], and 3-24[mm]. They recommended choosing conduit diameters that do not exceed the IVC diameter by 20%, minimizing the risk of thrombosis. IVC diameter has high variability and should be measured before selecting an appropriate conduit size. It is also recommended that the ECFO procedure is completed on the patient between the ages of 2-4 when the IVC to RPA distance is 60-80% of the adult size.

Itatani et al. [7] utilized CFD analysis to determine the optimum conduit size of ECFO procedures. A synthetic model was created using average patient data from 17 Fontan patients. The conduit size was then varied between 14[mm] and 22[mm]. The larger conduits caused large stagnation volumes and backward flow. The optimum conduit size was determined to be between 16[mm] and 18[mm] based on low energy loss and reduced flow stagnation.

Mardsen et al. [10] performed CFD analysis on the effects of exercise and respiration on the TCPC. They produced realistic hemodynamic data that was comparable to clinically measured data. The respiration model had a large effect on the exercise hemodynamics, and should be incorporated into future exercise models.

Hsia [6], de Leval [5], Mardsen [49], and Bove[47] looked to improve the Fontan hemodynamics by modifying the surgical procedure. CFD analysis was used to analyze the hemodynamic effects of different design parameters. These parameters included: **(1)** inferior cavopulmonary connection (ICPC) diameter, **(2)** ICPC location, **(3)** Y shaped ICPC, and **(4)** effects of the alternative Hemi-Fontan operation. All these parameters produced positive effects, but were not significant.

2.6 Assist Devices

Delorme et al. [40] used large eddy simulations to determine the effects of using a viscous impeller pump (VIP) within the Fontan circulation. The VIP was situated in the center of the TCPC to

reduce the swirl switch phenomenon due to the instabilities of the two impinging jets from the SVC and IVC. The VIP reduced IVC pressure at high levels of rotation (1000[rpm] to 2000[rpm]).

Shimizu et al. [61] used a rotational pump to assist the IVC flow. A multi-scale CFD-LPM approach was used to model a total assist pump (placed directly between the IVC and TCPC) and a partial assist pump (syphoned fluid from the SVC to the RPA). Both assist devices were successful in increasing pulmonary arterial pressure (PAP) and decreasing IVC and SVC pressure. However, the SVC flow was decreased.

Pekkan et al. [44] modeled ventricular assist devices for the Fontan circulation using a LPM. Three different types of VAD configurations were used to assist the pulmonary circulation. These types included: **(1)** IVC and SVC support, **(2)** RPA and LPA support, and **(3)** full TCPC support. IVC/SVC support caused higher pressures in the IVC because the Gore-Tex graft has low compliance. The LPA/RPA support caused graft collapse or buckling. They found that the full TCPC support was preferable due to its simplicity, ease of use, and one pump design.

Corno et al. [41] studied pulmonary support using animal (pigs), benchtop, and CFD models by using stimulated latissimus dorsi (LD) attached to the outside of the vessel wall. The LD provided 8-16 mmHg of pressure driving force to the compliant vessels. All their studies were successful in increasing pulmonary flow and decreasing IVC pressure, but flow obstruction caused severe limitations.

Valdovinos et al. [42] analyzed a benchtop model of a Fontan circulation with an external compression device powering the pulmonary system (a C-Pulse Heart Assist system). This external device lowers the risk of thrombus because of low blood contact. They measured the effect of adding and removing valves before and after the assist device. The IVC pressure was successfully lowered from 18[mmHg] to 8[mmHg].

Rodefeld et al. [39] summarized the powered Fontan research up to 2011. Since modifications to earlier stage palliations have failed to make a large impact of successful Fontan circulations, they suggest trying to find a way to make the 3-stage surgery into a one stage surgery. A one stage surgery would help reduce PVR and help with ventricular dysfunction (the ventricle is overloaded in the early stages). They suggest finding an "optimal assist device that would provide a 2-6[mmHg] energy input that would cause normal atrial filling, cardiac output, cerebral perfusion, oxygenation, and normal system pressure". Current mechanical issues caused by introducing pumps include: **(1)** only provides one way flow, **(2)** some require two pumps, **(3)** causes re-circulations (barriers), **(4)** suction at the inlet can cause collapse, **(5)** obstructive, and **(6)** can't be shut down. These mechanical issues lead to physiological issues such as **(1)** drive line infection, **(2)** pulmonary embolism, and **(3)** stroke, if a fenestration is present.

2.7 Pulmonary Vascular Resistance

Henain et al. [30] studied the effects of pulsatility on PVR by surgically implanting cavopulmonary shunts in 30 pigs. Measurements before and after surgery in the three control groups, (1) sham, (2) pulsatile, (3) and non-pulsatile, revealed that a lack of pulsatility elevated pulmonary arterial pressure and PVR.

Goldstein et al. [32] analyzed the relationship between PVR and diastolic function to exercise capacity in Fontan patients. Overall, PVR decreased with exercise, but in some patients, it remained constant. It was determined that the exercise limitations of Fontan patients are controlled by the PVR during peak exercise. Shachar et al. [24] also found that exercise, in 4 of their 5 Fontan patients, decreased PVR. However, the exact relationship that PVR has with exercise is still unknown. This is a

result of high variability in PVR response between the patients. Kung et al.[62] presented a PVR model of the Fontan circulation to account for exercise using the exercise studies above.

Reeves et al. [33] studied the distensibility of a normal human lung during exercise rather than just looking at total PVR. For isolated arterials, a one mmHg pressure will cause a two percent increase in vessel diameter. In fact, increasing flow pressure during exercise will dilate the lung vascular bed by 40%. They concluded that the distensibility of the lung arterioles contributes to high PVR reduction with increased pulmonary flow. Forton et al. [36] used Doppler echocardiography to measure the PVR, exercise capacity, pulmonary arterial pressure (PAP), and pulmonary flow of 26 healthy adult volunteers under different exercise conditions. They reported that the PVR decreased by about 40% at peak exercise in all exercise positions (supine, semi recumbent, and upright).

Naeije et al. [29] summarized the response of the pulmonary circulation during exercise. Some of these responses include: (1) ageing increases PVR, which will decrease cardiac output over time, (2) PVR is flow-dependent, (3) PVR decreases curvilinearly with increasing flow, and (4) the decrease in PVR during exercise is mainly caused by the release of vasodilators, such as prostacyclin and nitric oxide, by the pulmonary endothelium. PVR is a good indicator of the constriction or dilation of pulmonary vessels and detecting changes in the arteriolar vessel caliber.

Schmitt et al. [34] analyzed the response of PVR and collateral blood flow in 10 Fontan patients before and after the administration of dobutamine stress. Exclusion criteria for these patients included: fenestration, pulmonary artery stenosis, atrioventricular valve insufficiency, arrhythmias, protein-loss syndrome, thromboembolism, effusion, edema, or patients on beta blocker medications. Measurements were performed using MRI catheterization techniques during free breathing and during continuous infusion of 10 ug/kg per minute dobutamine. At 10 ug/kg per minute, dobutamine has no effect on PVR

[57]. Dobutamine effectively decreases systemic vascular resistance to increase cardiac output, which is an alternative method to simulate exercise stress in patients that are unable to perform adequately [58]. However, these results should not be directly correlated to physical exercise models. Overall, the increased cardiac output increased pulmonary flow which caused a decrease in PVR.

Rivera et al. [35] studied the relationship between pulmonary venus blood flow and PVR during free breathing and oxygen inhalation. The study group consisted of 18 patients with congenital heart disease and a left to right shunt. PVR and Qp/Qs were measured before and after 100% oxygen inhalation (10L/min oxygen mask) using catheterization and echocardiography. After oxygen inhalation, pulmonary flow increased and PVR decreased, but oxygen inhalation is known to also cause the PVR to decrease [59].

Petrofski et al. [73] provided a case study on mechanical ventricular support lowering PVR. An adult patient was suffering from severely elevated PVR and heart failure. After 24 hours of mechanical support to the systemic and pulmonary systems, the patient's PVR decreased from 13.8 [Wu] to 3.1 [Wu] (78% Drop). This allowed for a successful heart transplant without the need for a lung transplant.

The PVR vs. pulmonary flow relationship in Fontan patients is scarce, and consists of limited measurements. In all these cases, measurements were taken during rest and full stress. Ideally, there would also be measurements in between. Since this is not the case, a more useful relationship is PVR drop vs. pulmonary flow rise. The data from the research presented in this section is compiled and plotted in Figure 3.

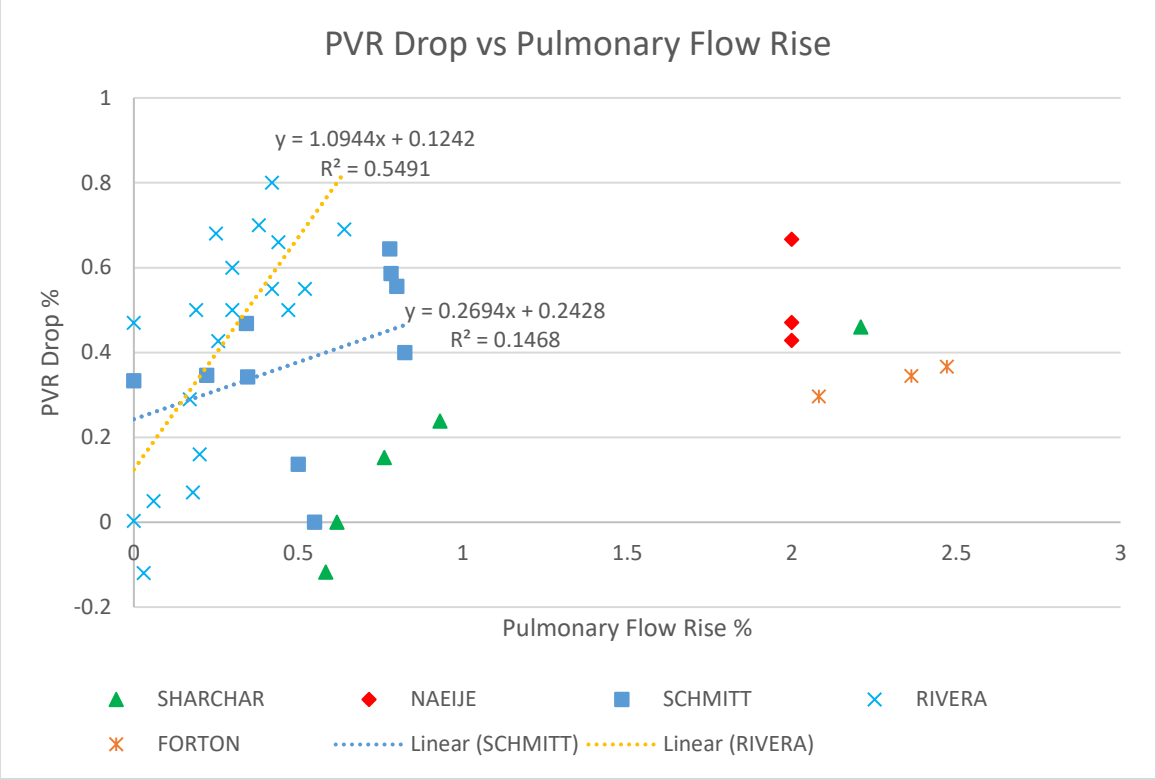

Figure 3: PVR Drop vs. Pulmonary Flow Rise.

2.8 Ejectors

Brahim et al. [69], Kandakure et al. [70], and Yadav et al. [71] studied the effects of liquid to gas mixing using ejectors in a convergent-divergent mixing chamber. To optimize mixing, entrainment, and mixing efficiency, they use design parameters such as nozzle diameter, throat to nozzle length, nozzle to throat area ratio, and primary to secondary flow ratio. Yadav observed that the ejector become less effective with low resistance models. As the resistance decreases, the required driving pressure also decreases, which results in lower entrainment rates [71].

Mujherjee et al. [68] analyzed the efficiency of liquid to liquid dispersion using ejectors. Decreases in efficiency are attributed to mixing, friction, and flow channel shape. They found that the energy loss could be minimized by choosing correct throat to nozzle area ratios and optimal primary to secondary

flow ratios, shown in Table 1. For the Fontan IJS (Injection Jet Shunt) being proposed, the throat diameter and Qp/Qs is restricted by patient physiology at 12[mm] and 1.5 respectively. This data suggests that the optimal IJS nozzle diameter should be between 2.25[mm] and 3.375[mm].

Table 1: Optimal Flow Ratio to Minimize Energy Loss [68]. φR(opt): Optimal Primary to Secondary Flow Ratio, Dn: Nozzle Diameter, Qp/Qs: Pulmonary to Systemic Flow Ratio.

Primary	Secondary	Density Ratio	Area Ratio	ϕR(opt)	Dn[mm]	Qp/Qs
Water	Kerosene	0.81	50.607	3.039	1.687	1.329
			28.434	1.97	**2.25**	**1.508**
			12.645	1.057	**3.375**	**1.946**
			7.111	0.678	4.5	2.475
Kerosene	Water	1.235	50.607	2.728	1.687	1.367
			28.434	1.785	**2.25**	**1.56**
			12.645	0.968	**3.375**	**2.033**
			7.111	0.623	4.5	2.605
Water	Paraffin	0.808	50.607	3.041	1.687	1.329
			28.434	1.971	**2.25**	**1.507**
			12.645	1.058	**3.375**	**1.945**
			7.111	0.679	4.5	2.473
Paraffin	Water	1.238	50.607	2.729	1.687	1.366
			28.434	1.783	**2.25**	**1.561**
			12.645	0.968	**3.375**	**2.033**
			7.111	0.623	4.5	2.605

CHAPTER 3: METHODS AND MODELING

3.1 Anatomical Model

3.1.1 Synthetic Anatomical Models

For the synthetic model, the TCPC was modeled using SolidWorks (Dassault Systemes) with average dimensions of a 2-4 year-old Fontan patient [3][5][7], shown in Figure 4. The modifications for each synthetic model configuration was then applied to the baseline synthetic model. The four synthetic model configurations include a(an) (1) baseline, (2) IJS, (3) no entrainment shunt (NES), and (4) IJS with pulmonary artery radius increase. The IJS intrudes into the pulmonary arteries and turns to orient its nozzles parallel to the flow direction of the pulmonary arteries, illustrated in Figure 5. To isolate IJS entrainment effects, a NES model, shown in Figure 5,was developed to augment pulmonary flow without entrainment. Increased pulmonary flow will also increase the cross-sectional flow area of the pulmonary arteries. The area expansion was modeled by increasing the pulmonary artery radius by 10.668%, shown in Figure 6.

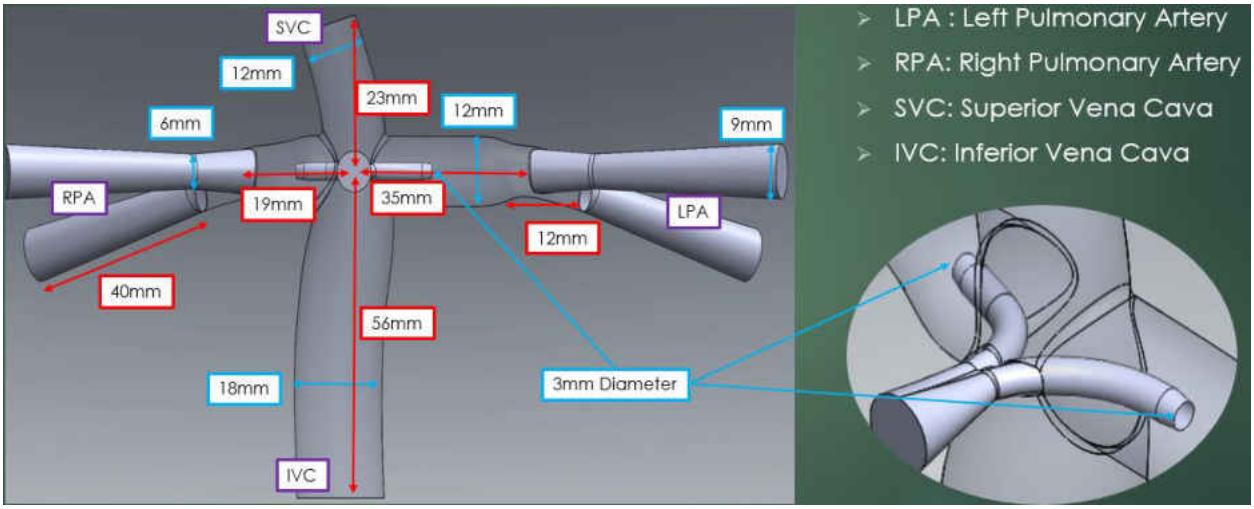

Figure 4: Powered Fontan Fluid Domain Model. SVC: Superior Vena Cava, IVC: Inferior Vena Cava, RPA: Right Pulmonary Artery, LPA: Left Pulmonary Artery

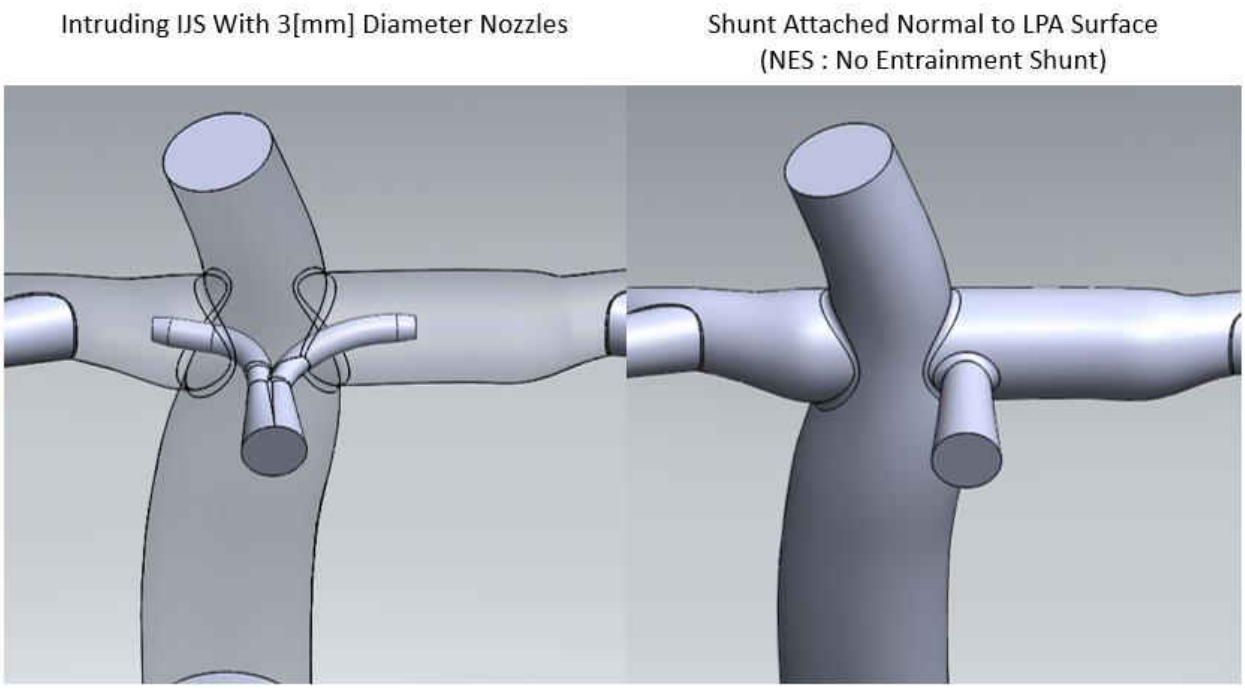

Figure 5: Synthetic Model Configurations. Left: IJS, Right: NES.

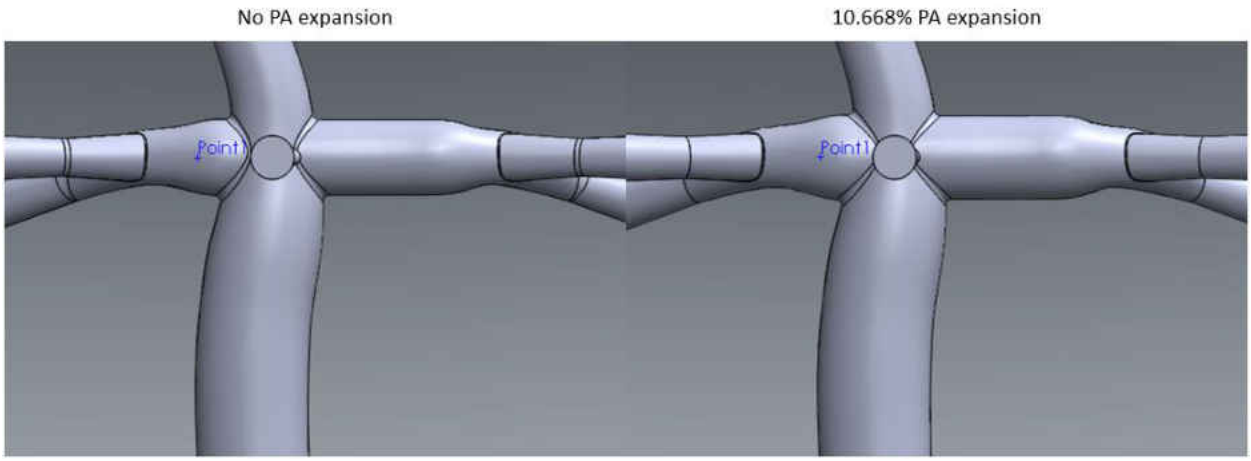

Figure 6: Synthetic Model Configurations. Left: Baseline, Right: 10.668% Pulmonary Expansion.

This 10.668% expansion was determined with the use of Poiseuille flow, $\frac{Qi}{Qf} \sim (\frac{ri}{rf})^4$, and assuming the pulmonary artery wall will expand to accommodate a flow increase of 50%. Where Q is the flow rate and r is the radius.

3.1.2 CHOP Anatomical Models

For the patient-specific models, the TCPC geometry is gathered through MRI scans, displayed in Figure 7. These scans are then converted to three dimensional models using the segmentation software MIMICS. The rough and jagged surfaces are smoothed using Blender as shown in Figure 8. The fluid region is then extracted from this smooth surface using SolidWorks. Cross-sectional curves are then used to cut the surface into several sections. The fluid region is then lofted across these curve cuts, illustrated in Figure 9. Both the synthetic and patient specific models underwent the same meshing procedures as outlined in section 3.3. The injection jet shunt (IJS), shown in Figure 4, was designed to provide the requisite jet velocity to achieve the desired momentum transfer as well as minimize the power losses. The IJS connection is tapered and connected in such a way that the incoming flow will transfer momentum to the slow-moving system. To maximize such gains, the IJS geometry was iteratively modified.

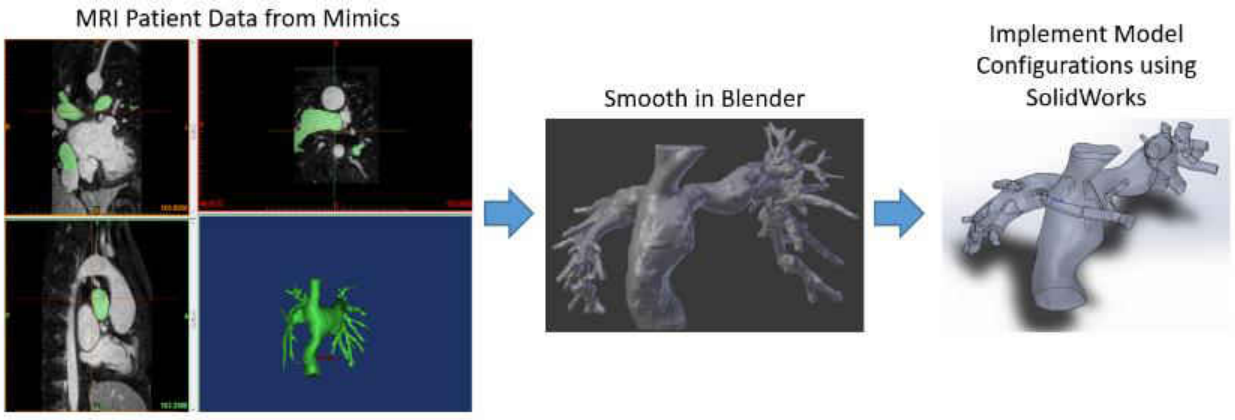

Figure 7: Procedure to Extract Solid Model Geometry from MRI Scans [13].

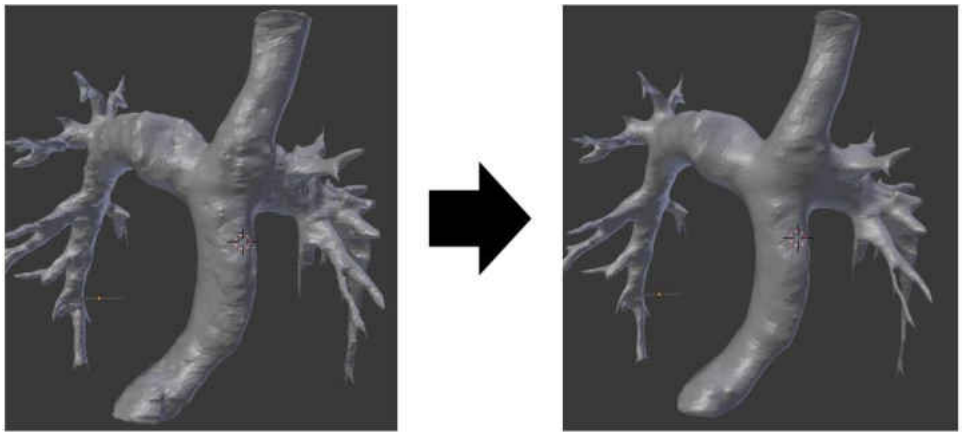

Figure 8: Smoothing of the CHOP-6 Model Using Blender. Left: Rough Model Imported from MRI Scans, Right: Blender Smoothed CHOP 6 Model.

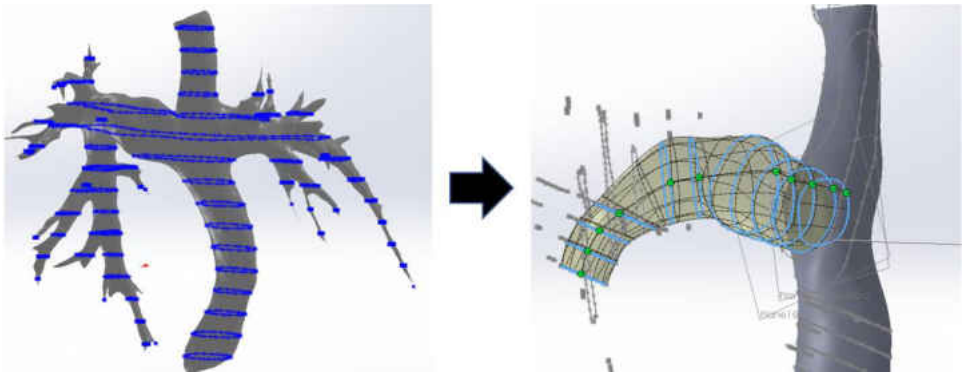

Figure 9: Fluid Region Construction on CHOP 6 Using SolidWorks. Left: Curve Cuts Using Curve Wizard. Right: Lofting Across the Curve Cuts.

CHOP-1 data was used to create two different IJS configurations. First was an intruding IJS, which is illustrated in Figure 10. The nozzle diameter was calculated using the optimal area ratio found in section 4.2. The IJS nozzle was placed at the center of the cross-sectional area of each pulmonary artery. The nozzle was also pointed in the direction parallel to the vessel walls. Overall dimensions of this configuration are illustrated in Figure 11. The second configuration was an "outer" IJS, shown in Figure 12. This IJS required an angle of attachment to the wall of the pulmonary artery. Hence, angles coincided with the patient-specific geometry by orienting the nozzle to eject as parallel to the flow as

possible without causing detrimental effects to the vessel walls. CHOP-4 and CHOP-6 are modeled using these same techniques in Figure 13 and Figure 14 respectively.

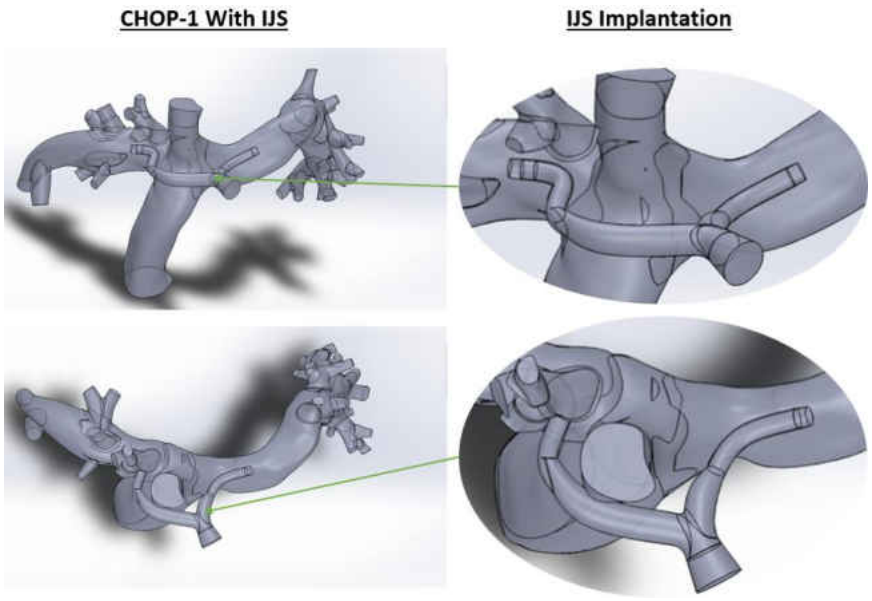

Figure 10: CHOP-1 with Inside IJS Configuration.

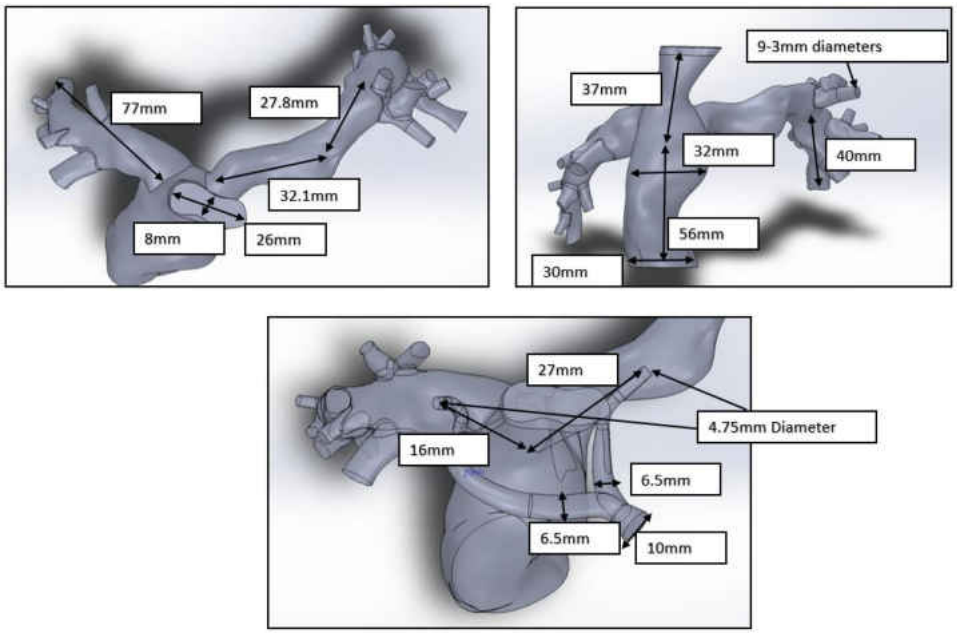

Figure 11: CHOP-1 Model Dimensions.

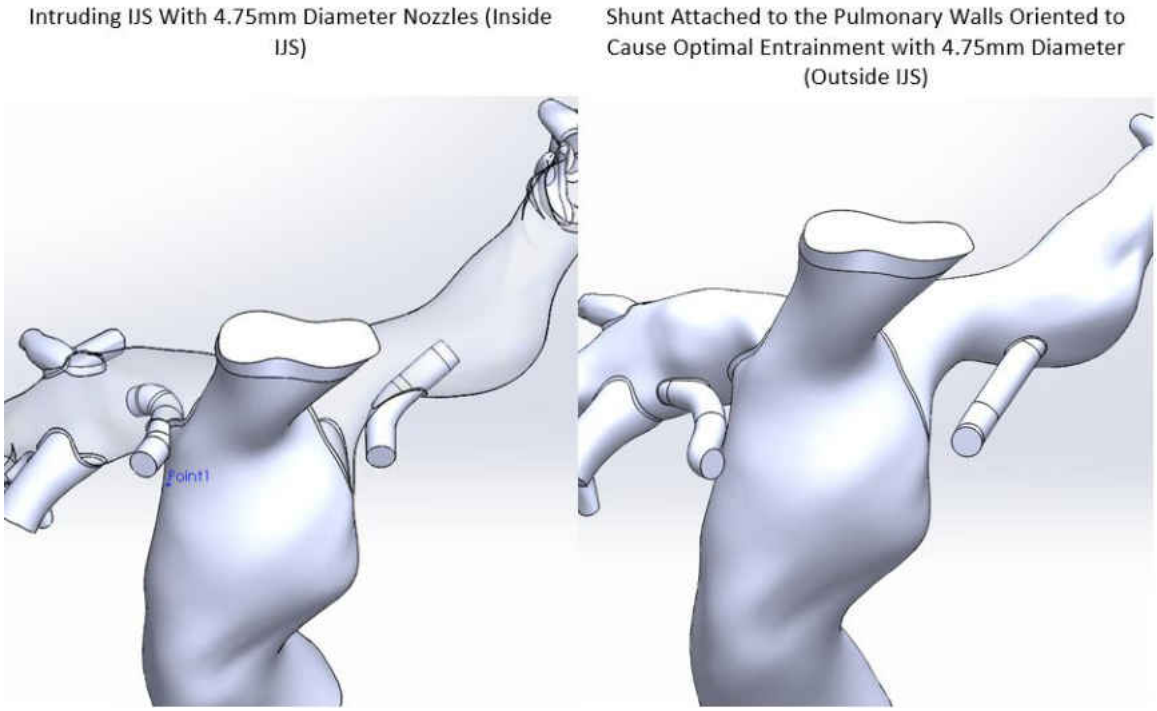

Figure 12: CHOP-1. Left: Inside IJS, Right: Outside IJS.

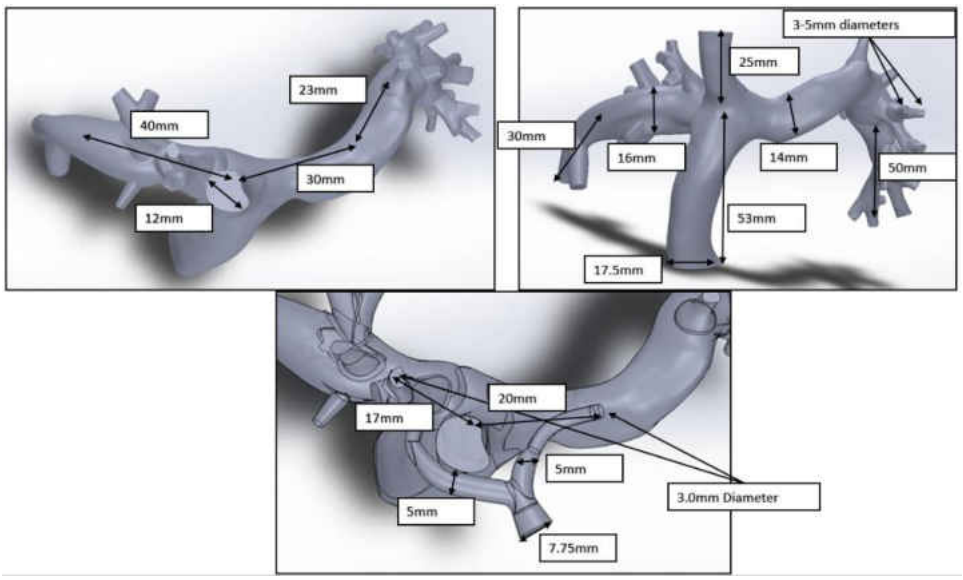

Figure 13: CHOP-4 Model Dimensions.

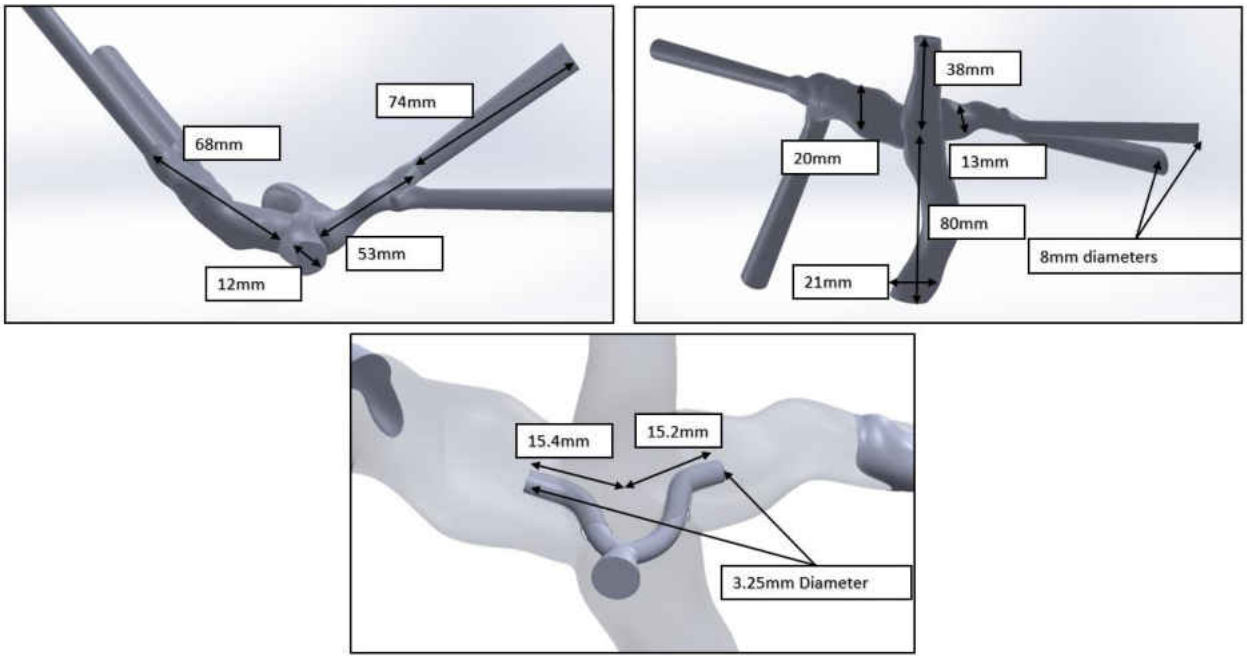

Figure 14: CHOP-6 Model Dimensions.

3.1.3 CHOP Flow Extraction from MRI Scans

The MRI data for the CHOP models also included flow rates for the SVC, IVC, LPA, and RPA. Medis is used to extract the flow data by taking a trace of the cross-sectional area of the vessel of interest, displayed in Figure 15. The IVC, SVC, LPA, and RPA flow rate wave forms from the CHOP-1 and CHOP-6 data are plotted in Figure 16 and Figure 17. The MRI data for the LPA and RPA flows did not immediately satisfy continuity. The LPA and RPA wave forms that are labeled with a "C" are the corrected wave forms that satisfy continuity.

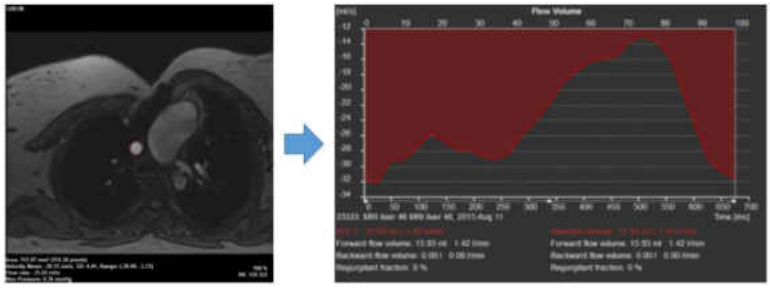

Figure 15: Flow Data Extraction from MRI Scans Using Medis.

The mean flow rates from this MRI data extraction is provided in Table 2. The mean pressures for the ventricle and the pulmonary artery are taken from patients with similar age and weight [34]. This data is then used to tune the LPM for each individual patient, section 4.4.

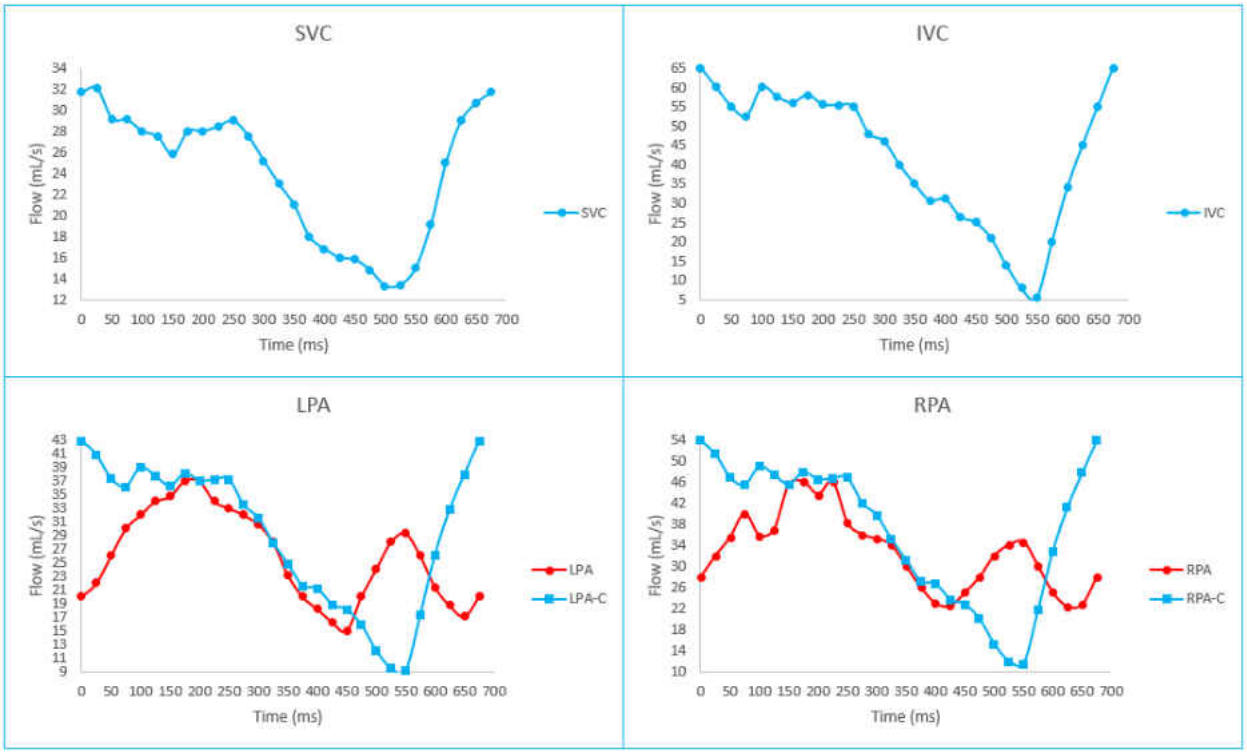

Figure 16: CHOP-1 MRI Flow Rate Data.

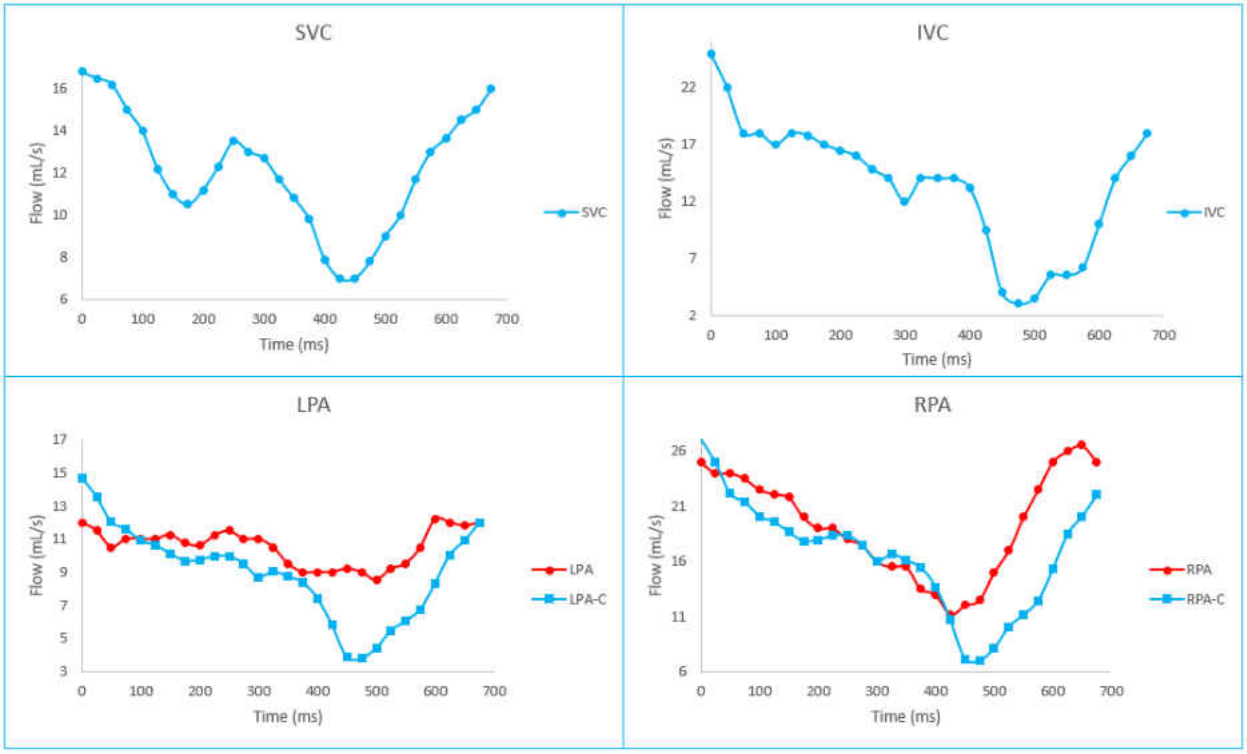

Figure 17: CHOP-6 MRI Flow Rate Data.

Table 2: Extracted Mean Flow Values from CHOP MRI Scans. BPM: Beats per Minute, L/min: Liters per Minute, RPA-C: Corrected RPA Flow, LPA-C: Corrected LPA Flow.

		kg	BPM	L/min	L/min	L/min	L/min	Seconds
Model	Age	Weight	Heart Rate	SVC	IVC	RPA-C	LPA-C	Heart Cycle
CHOP 1	24	91	89	1.420	2.500	2.211	1.757	0.674
CHOP 4	12	45.4	75	1.380	2.430	2.340	1.470	0.800
CHOP 6	10	28.8	88	0.680	0.790	0.517	0.953	0.682

Table 3: Mean Pressures of Fontan Patients with Similar Age and Weight [34]. EDP: End Diastolic Pressure, ESP: End Systolic Pressure, PAP: Pulmonary Arterial Pressure.

	mmHg	mmHg	mmHg
	EDP	ESP	PAP
CHOP 1	6.9+/-1.4	87.5+/-9.5	12.8+/-0.1
CHOP 4	7.3+/-1.7	105.0+/-14.0	12.7+/-0.5
CHOP 6	4.0+/-1.9	95.0+/-15.0	11.1+/-2.1

3.2 Cardiovascular Circuit: 0D Lumped Parameter Model

To begin, the cardiovascular system of a patient must be properly simulated. These simulations will help to determine the cardiovascular output of the whole system as well as the pressures and flow rates at every node in the circuit. This data is then used to create waveforms that can be compared to patient data that is available from many resources [6][7] [9][10][47][49][72]. The single ventricle Fontan circulation is simplified by splitting the system into several coupled beds. These beds are known as multi-degree of freedom Windkessel models, Figure 18, which consist of resistors, capacitors, and inductors; each of which can be time dependent [7]. To drive the system, the single ventricle heart bed consists of a time varying capacitor that acts as a pumping heart, shown in Figure 19.

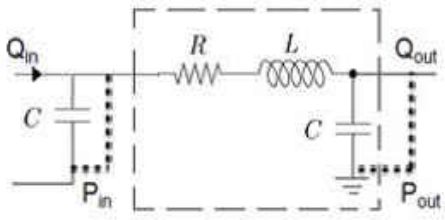

Figure 18: RLC Compartments Used for Vascular Beds.

This is the driving function that provides the pulsatile cardiac output. The reciprocal to the capacitance is the elastance function $E_n(t_n)$, which relates the pressure and volume during the cardiac cycle. The "double hill" normalized elastance function[1][2] is given as:

$$E(t) = (E_{max} - E_{min})E_n(t_n) + E_{min} \tag{3.2.1}$$

$$E_n(t_n) = \left[\frac{\left(\frac{t_n}{0.303}\right)^{1.32}}{1+\left(\frac{t_n}{0.303}\right)^{1.32}}\right]\left[\frac{1}{1+\left(\frac{t_n}{0.508}\right)^{121.9}}\right] \tag{3.2.2}$$

$$t_n = \frac{t}{t_c} \cdots t_c = \frac{60}{HR} \cdots HR = Heart\ Rate \tag{3.2.3}$$

To properly tune the circuit, these beds must interact with each other in a closed loop system, otherwise the resistor, capacitor and inductor values cannot be adjusted accordingly. Note that initial R-L-C values for the entire circuit, as well as E_{max} and E_{min} values, are found through previous research [1][2]. These values are then iterated upon until the proper wave forms have been reached, which is determined by comparing them to measured patient data as mentioned above. By tuning the circuit, the cardiovascular output and pressure wave forms are matched to measured patient data gathered from the models provided by Children's Hospital of Philadelphia (CHOP). This coupled problem becomes a system of linear ordinary differential equations that can be solved using 4th order adaptive Runge-Kutta methods.

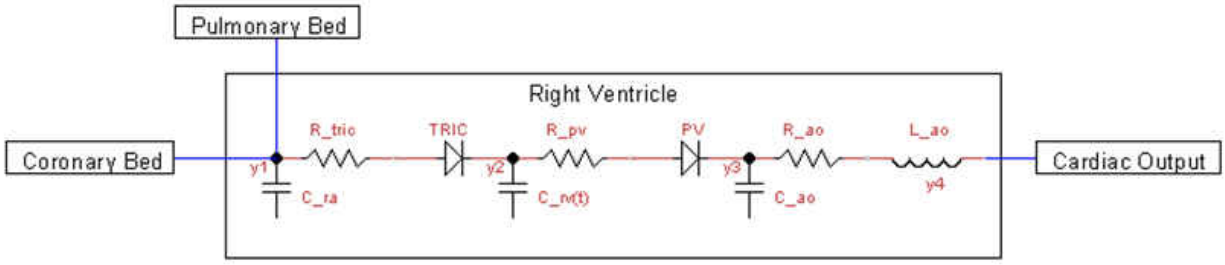

Figure 19: Electrical Bed for the Single Right Ventricle Heart.

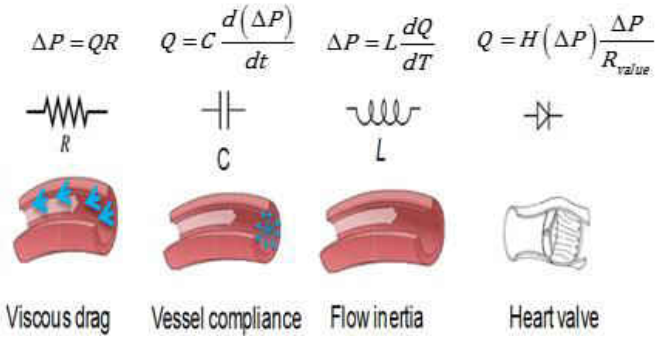

Figure 20: Hydraulic Analogy.

These differential equations are derived using the hydraulic analogies shown in Figure 20, along with the conservation of current (KCL) and voltage laws (KVL). As Figure 20 illustrates, the resistance, R[mmHg-s/ml], accounts for the static vascular resistance. The capacitance, C[ml/mmHg], accounts for the dynamic vascular compliance, and the inductance, L[mmHg s^2/ml], accounts for the inertial acceleration. The heart valves are modeled using diodes which are controlled using heavy step side functions that are dependent upon vascular pressure. The differential equations that govern the R-L-C compartments, from Figure 18, are as follows:

$$\Delta P = L\frac{dQ}{dt} + RQ \tag{3.2.4}$$

$$Q = C\frac{d(P)}{dt} \tag{3.2.5}$$

$$C = \frac{dV}{dP} \tag{3.2.6}$$

Where Q is the flow-rate, ΔP is the pressure difference and V is the volume. The complete closed loop diagram of the simplified Fontan circulation is shown in Figure 21. The full Fontan circuit is illustrated in Figure 22. The section that is circled and labeled “CFD” corresponds to the Fontan TCPC location. This section is modeled using resistances only. To calculate the test section resistances, the 3D section is subjected to steady state boundary conditions using CFD. These resistances are then back calculated using the tube flow relationships described by equations 7 through 9. Once these resistances are calculated, the iterative tuning process, illustrated in Figure 23, begins.

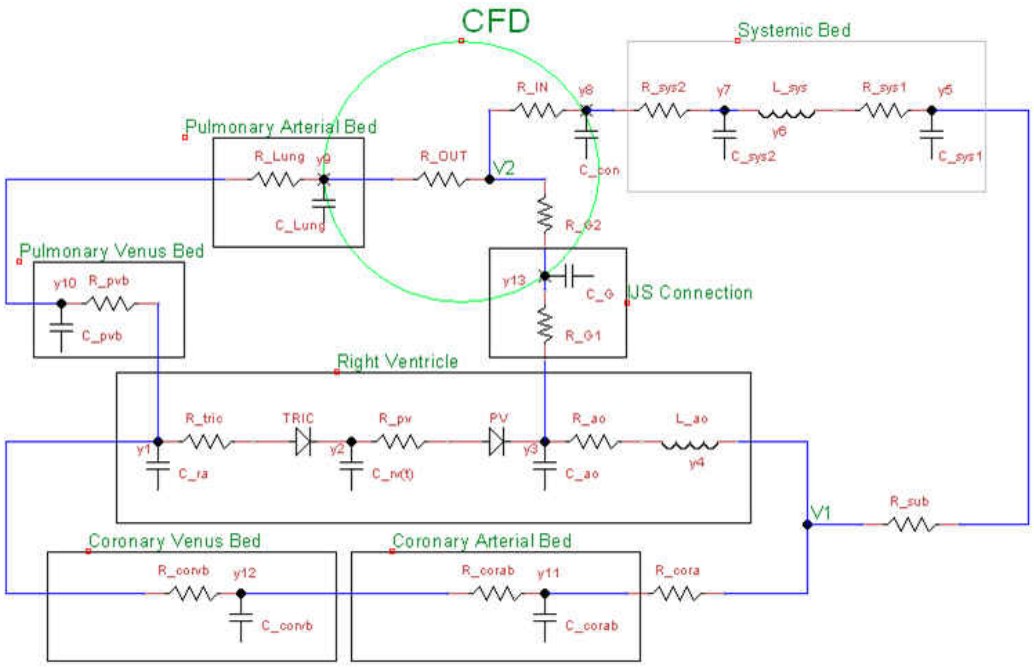

Figure 21: Complete Closed Loop Diagram of the Simplified Fontan Circulation.

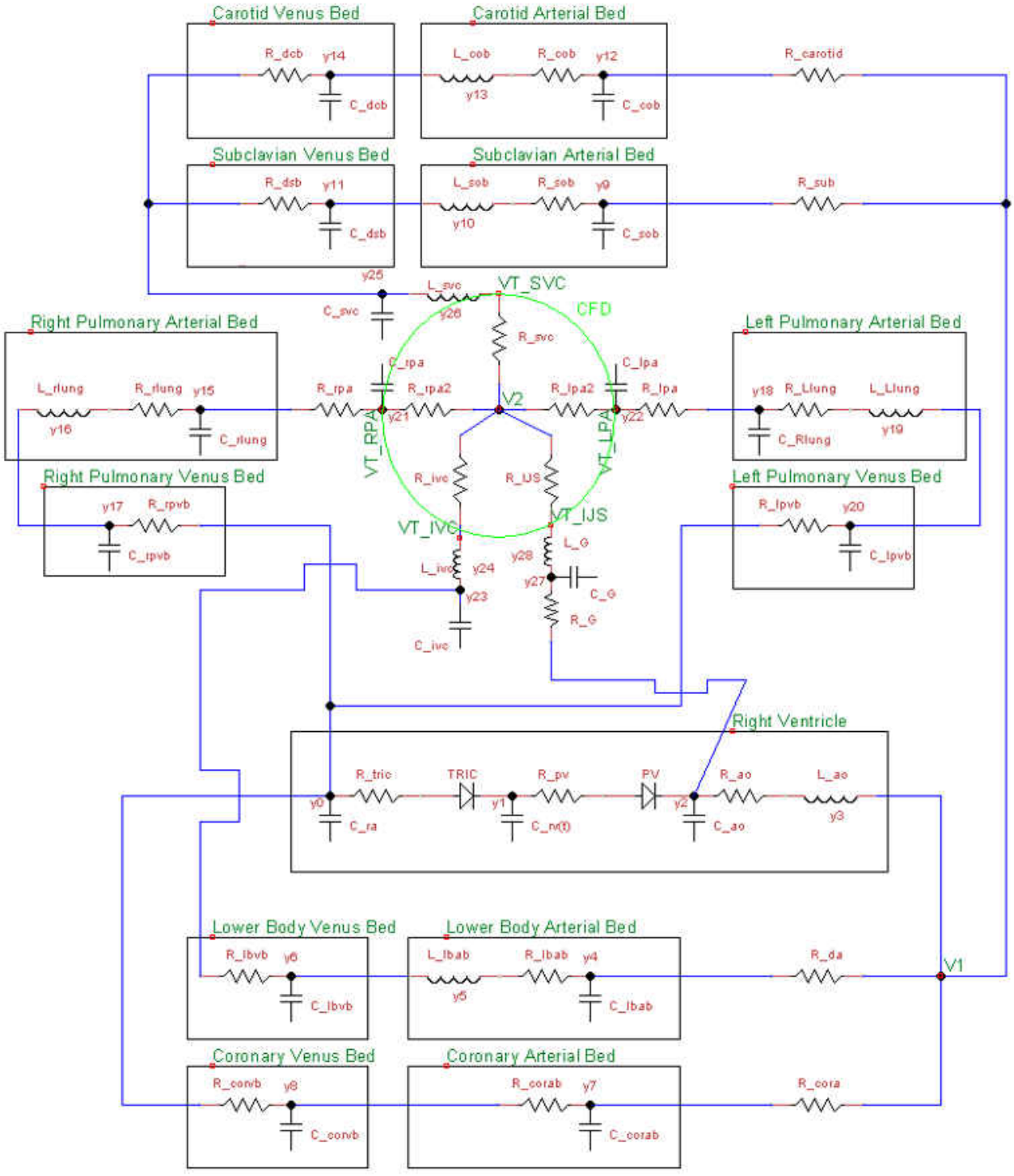

Figure 22: Complete Closed Loop Diagram of the Full Fontan Circulation.

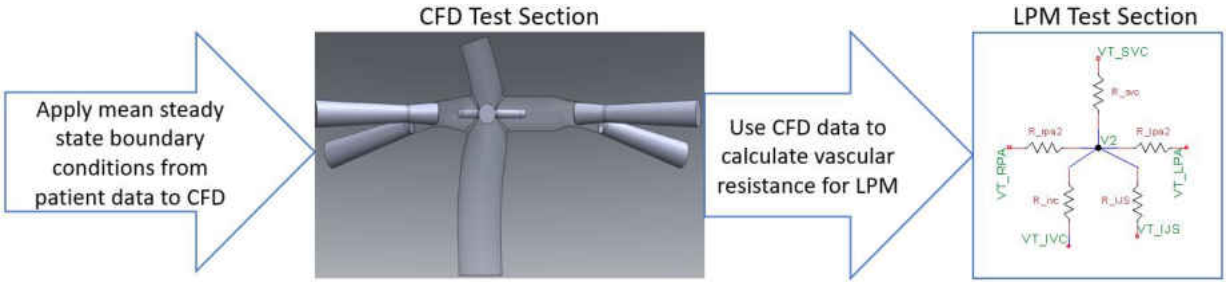

Figure 23: LPM Test Section Initialization.

$$\Delta p = RQ \tag{3.2.7}$$

$$Q = \frac{\pi \Delta p D^4}{128 \mu L} \cdots Volume\ Flow \left[\frac{mL}{s}\right] \tag{3.2.8}$$

$$R = \left[\frac{128 \mu L}{\pi D^4}\right]\left[\frac{1000}{133.322368}\right] \cdots Resistance \left[\frac{mmHg \cdot s}{mL}\right] \tag{3.2.9}$$

The parameters in the above equations are expressed in [mm] and [Pa-s]. The viscosity of blood, μ, is taken to be 0.004[Pa-s].

3.2.1 Pulmonary Vascular Resistance Model

The proposed IJS model will increase pulmonary flow by injecting energy into the pulmonary system using an IJS connected between the aorta and the pulmonary arteries. It is known that pulmonary vascular resistance (PVR) decreases curvilinearly with increasing pulmonary flow during exercise [29]. Thus, a PVR model is required to accurately simulate the pulmonary vasculature in the LPM. A robust model of the PVR vs. pulmonary flow relationship in Fontan patients is not available. The exercise PVR model includes effects other than increased pulmonary flow, such as increased systemic vascular resistance (SVR) and vasodilation of the pulmonary system caused by chemicals (prostacyclin and nitric oxide) being released by pulmonary endothelium during exercise. Schmitt et al. [34] isolates this effect by administering dobutamine to cause increased pulmonary flow in Fontan patients. At 10 ug/kg per minute, dobutamine has no effect on PVR [57]. Dobutamine effectively decreases systemic

vascular resistance to increase cardiac output, which is an alternative method to simulate exercise stress in patients that are unable to perform adequately [58]. To efficiently model the PVR vs. flow relationship, the PVR drop % is related to the pulmonary flow rise %, shown in Figure 24. A 50% increase in pulmonary flow (Qp/Qs = 1.5) is the physiological limit for a left-to-right shunt. Hence, the PVR drop is approximated by the response of the 4 patients with pulmonary flow rises close to 50% (circled in Figure 24). The average PVR drop between these patients is ~57%, therefore a 60% PVR drop is used in all the PVR models presented.

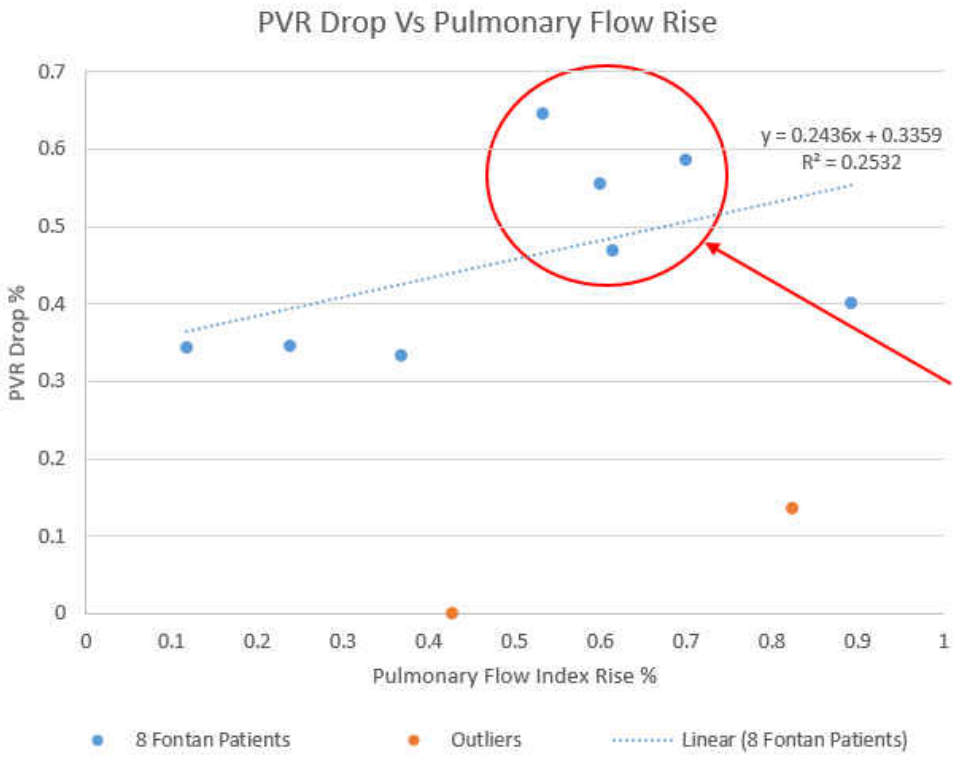

Figure 24: PVR Drop as a Function of Pulmonary Flow Rise [34].

3.3 CFD Solver and Fluid Domain Meshing

Synthetic geometry models are created in SolidWorks as described in section 3.1. Patient specific models are captured using MRI-scans along with MIMICS. These models are then imported into Blender

for smoothing modifications. Smoothed patient-specific models are then imported into Star-CCM+, which is a commercial multi-physics finite volume based computational fluid dynamics solver developed by CD-Adapco [12]. The fluid domain is modeled as an incompressible Newtonian fluid with blood density and viscosity material properties. The flow field solution is obtained by solving the Navier-Stokes equations of mass and momentum as shown here:

$$\nabla \cdot \overline{V} = 0 \ \cdots \ mass \tag{3.3.1}$$

$$\rho \frac{\partial \overline{V}}{\partial t} + \rho(\nabla \cdot \overline{V})\overline{V} = -\nabla p + \mu \nabla^2 \overline{V} \ \cdots \ momentum \tag{3.3.2}$$

These equations consist of the velocity field $\overline{V}$, and the pressure field p. The blood density, ρ, is $1060 \left[\frac{kg}{m^3}\right]$, and the blood viscosity, μ, is $0.004[Pa \cdot s]$. Star-CCM+ solves these equations using an unsteady implicit solver with a second order time discretization and second order up winding. The boundary conditions at the all the inlets (SVC, IVC, and IJS) are given as a mass flow rate inlets (Dirichlet). The boundary conditions at the exits (RPA, and LPA) are given as pressures (Neumann). These boundary conditions are calculated using the 0D lumped parameter model. The wall conditions are modeled as non-compliant due to a recent study showing small differences between compliant and non-compliant models [11]. As for proper time step selection, the Courant number (equation 3) needs to be close to one to obtain time accurate solutions with slow velocity fields (less than 0.2[m/s]).

$$Courant\ Number = \frac{u \cdot \Delta t}{\Delta x} \tag{3.3.3}$$

The procedure used to determine this time step was to first calculate an expected velocity based on the volumetric flow rate, and back calculate the needed time step, which is also based on the mesh size. With this combination of mesh size and velocity, the optimal time step is close to 0.002 seconds. The fluid domain is meshed using tetrahedral elements with a base mesh size of 0.7[mm]. The boundary

layers are treated by using 4 prism layers with a growth rate of 1.3. The CHOP-1 model, shown in Figure 25, contains close to 3 million cells. This mesh size was chosen to keep the time step relatively low as compared to the heart rate of a single ventricle Fontan patient of 120[bpm] [8]. This time step was chosen to be 1/200th of the heart cycle for each model.

Figure 25: Tetrahedral Mesh of the CHOP-1 Model.

Mesh convergence was completed for each model by monitoring the pressures at the inlets and the mass flow at the outlets. The cell count for all the included models are presented in Table 4.

Table 4: Converged Mesh Cell Counts for All Models.

Model	Number of Cells/Elements
Simple Entrainment (Prelim Study)	
Simple Entrainment (Inside Jet)	604872
Simple Entrainment (Outside Jet)	427136
Synthetic	
Synthetic (IJS Inside)	9595568
Synthetic (NES)	7187368
CHOP-1	
CHOP-1 (IJS Inside)	2537397
CHOP-1 (IJS Outside)	2334799
CHOP-6	
CHOP-6 (IJS)	2162445

3.4 Tight Coupling of the Lumped Parameter and CFD Model

The coupling of the CFD and lumped parameter models in previous applications [1][2] have been at the cycle level, “loose coupling”. Hence, the update occurs once every heart cycle. In the loose coupling case, the lumped parameter model is completely closed and its resistances at the area of interest are updated after the CFD cycle is complete. Due to the nature (momentum transfer) of the proposed application, the lumped parameter model (LPM) is insufficient because of its 0D nature. LPM fails to capture momentum transfer, but where LPM fails, CFD exceeds. To properly capture the momentum transfer, the update must occur at every time step. This is referred to as “tight coupling” [20][23][14][56].

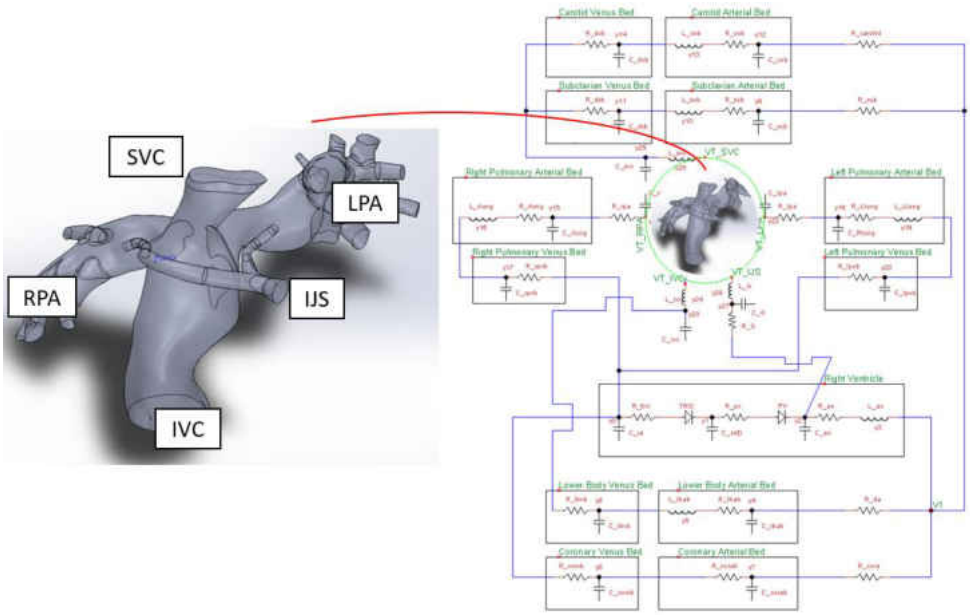

Figure 26: Tightly Coupled Baseline Model. Updates Occur at the Interface Between the LPM and CFD.

The area of interest is removed from the LPM and replaced with the CFD model as shown in Figure 26. The LPM is now open and completely dependent upon the CFD. They are connected at the inlets and exits of the CFD model which are labeled as VT_SVC, VT_IVC, VT_LPA, VT_RPA, and VT_IJS. The tightly coupled scheme is illustrated in Figure 27. In this scheme, the CFD leads the LPM in time and the boundary conditions are relaxed from the CFD to the LPM.

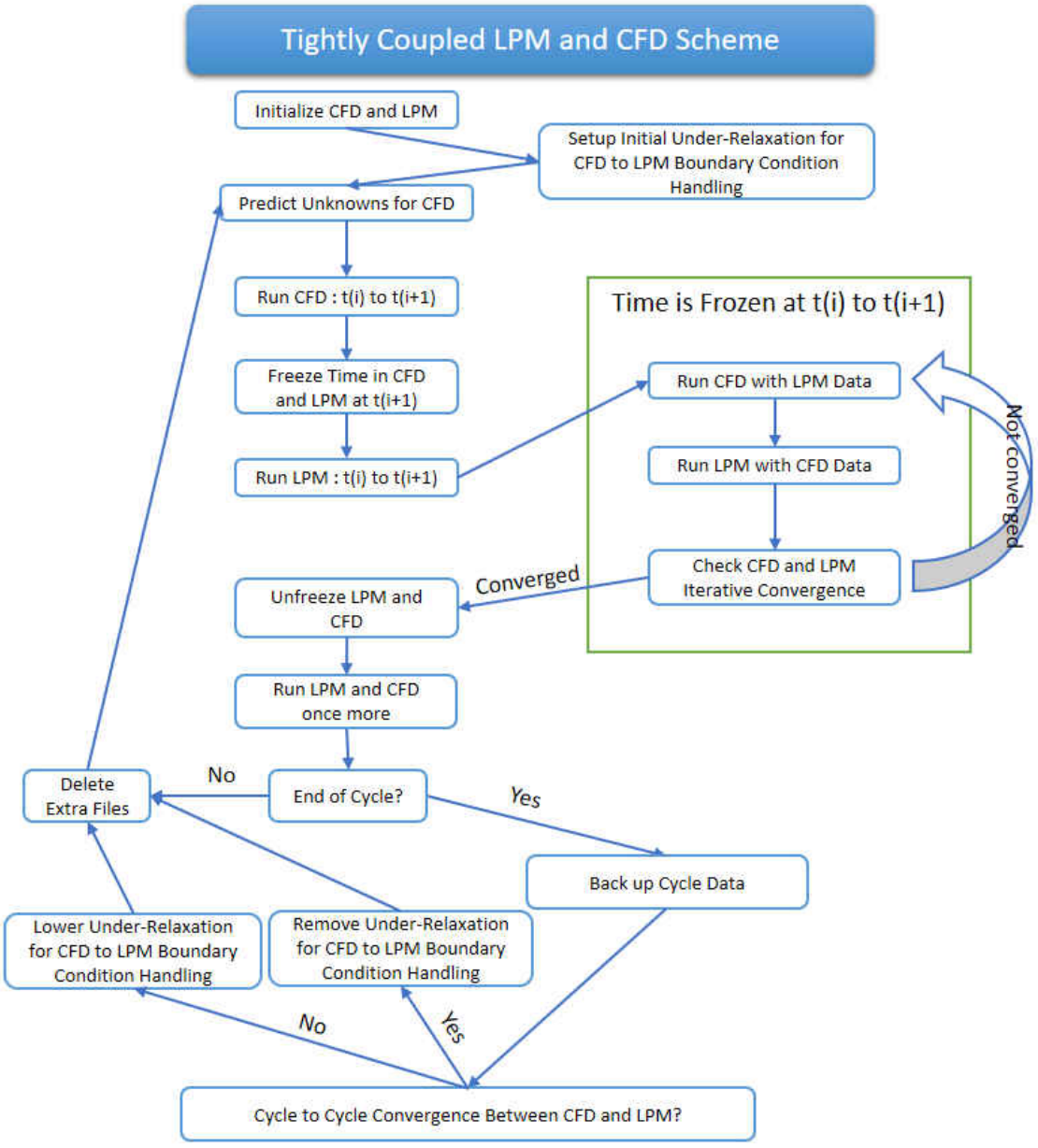

Figure 27: Tightly Coupled Scheme for CFD-LPM Modeling Using Commercial CFD Software. t: Time, i: Iteration.

Rather than taking the full value from the CFD, it is damped based on the previous cycle values. This "boundary condition relaxation" is calculated by linearly interpolating between the previous value and the new calculated value, equation 1. This damping is slowly removed after every complete cycle until

the LPM and CFD have converged to a stable solution. Convergence is measured using normalized least squares on the LPM-CFD boundary values, equations 2 and 3.

$$y_r = \left(y_c - y_p\right) * R\% + y_p \tag{3.4.1}$$

$$\epsilon_{cycle} = \sum_{i=0}^{N} \sum_{t=0}^{M} \frac{\left|CFDx_i^t - LPMx_i^t\right|^2}{\varphi_i^2} \tag{3.4.2}$$

$$\epsilon_{time-step} = \sum_{i=0}^{N} \frac{|pCFDx_i - nCFDx_i|^2}{\varphi_i^2} + \sum_{i=0}^{N} \frac{|pLPMx_i - nLPMx_i|^2}{\varphi_i^2} \tag{3.4.3}$$

Where y is the boundary condition value, R% is the relaxation parameter, r is the relaxed value, p is the previous cycle value, c is the current cycle value, N is the number of boundaries, M is the number of time steps, φ_i is the normalization of the i^{th} boundary value, x is the boundary value, p are the previous values, and n is the new calculated values.

3.4.1 Choosing Parameters at the Interface Between the LPM and CFD Models

When coupling LPM and CFD models, choosing the proper interface parameters will increase stability. When passing flow rates (Dirichlet) to the LPM, the interface should be connected by a capacitor. When passing pressures (Neumann)to the LPM, the interface should be connected by an inductor [20][23][56]. Choosing proper capacitance values are also important for the stability of the multi-scale model. The C values should be proportional is the area of the inlet/outlets, $C_{LPM}[m^4] \propto A_{CFD}[m^2]$ [23]. The C values should then be iterated upon to provide proper wave forms and mean values. Opposite interface coupling will cause the pressure/flow at the coupled surface to oscillate and rapidly diverge [56].

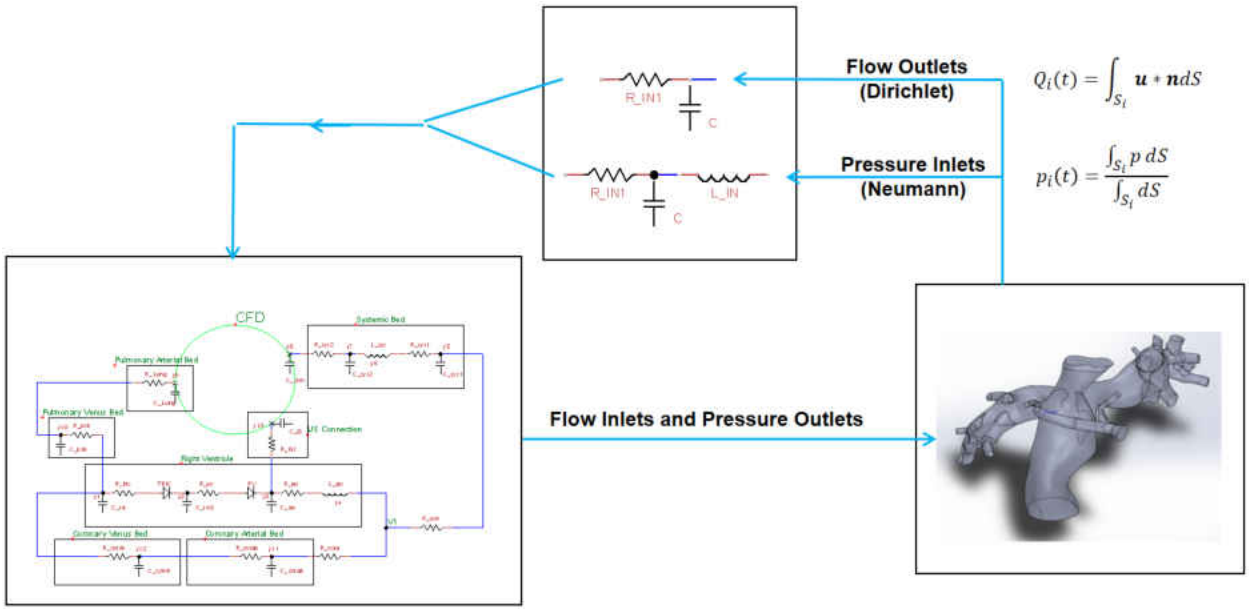

Figure 28: Interface Parameter Selection. Q: Flow Rate, p: Pressure, u: Velocity Vector, n: Normal Surface, S: Surface.

3.4.2 Boundary Condition Prediction

For the CFD to lead the LPM in time, initial guesses for the boundary conditions are required. For each time step, the initial guess is calculated by using linear extrapolation, equation 4, based on the previous cycle.

$$y_n^{i+1} = a_{n-1} x_n^{i+1} + b_n \tag{3.4.4}$$

$$a_{n-1} = \frac{y_{n-1}^{i} - y_{n-1}^{i+1}}{x_{n-1}^{i} - x_{n-1}^{i+1}} \tag{3.4.5}$$

$$b_n = y_n^{i} - a_{n-1} x_n^{i} \tag{3.4.6}$$

Where y is the boundary condition value, x is time, i is the current time step, and n is the current cycle.

3.4.3 Interface Stabilization

As the CFD passes information from the interface to the LPM, it is relaxed to reduce large changes that could potentially cause the LPM to diverge. The LPM to CFD information transfer is not relaxed, and

receives treatment for noisy data. Backflow stabilization at the multiscale model interface is required because the driving pressure drop within CFD model (test section) is orders of magnitude below the interface pressure, even flow being split by a bifurcation is highly dependent on the boundary conditions rather than the 3D model [19]. First, the open loop LPM is stabilized by matching the interface to the initialized CFD flow field. The interface conditions for the LPM are slowly changed over several cycles until they match the CFD interface conditions using a "settling wave technique", illustrated in Figure 29. This is achieved by using the same linear interpolation function in equation 1, and increasing the %R value from 0 to 1.

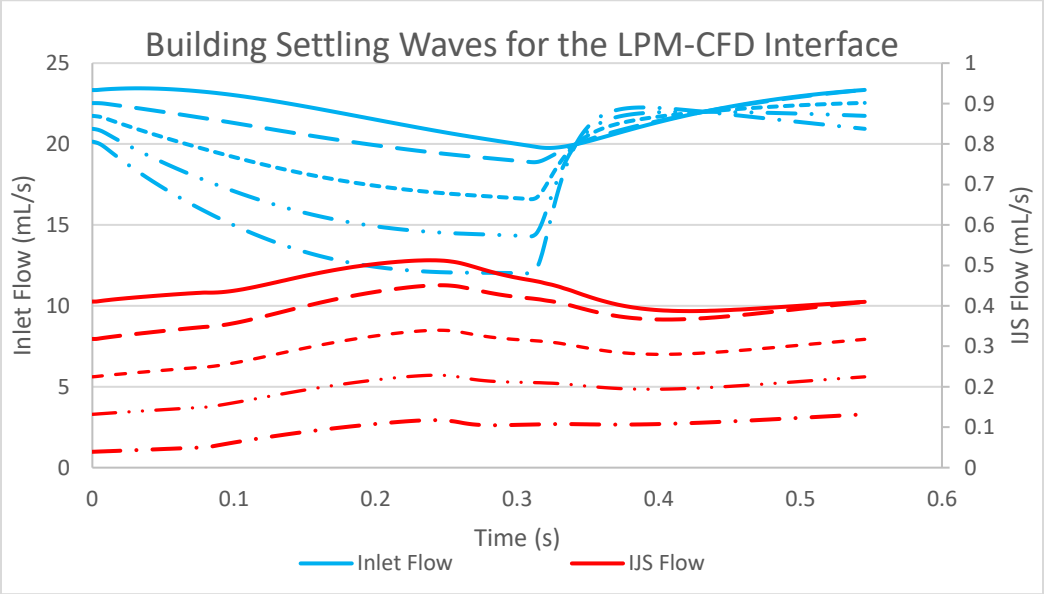

Figure 29: Settling Waves for CFD-LPM Stabilization.

Second, the noise in the CFD data is canceled out by using a central moving average (CMA) (equations 7 to 11), and a noise canceling (NC) technique in conjunction, shown in Figure 30. The NC technique utilizes the slope of the percent difference (SPD) in equation 12. SPD values above a tolerance, δ, are removed and replaced by a quadratic interpolation between the nearest values below δ. The CMA takes over for SPD values below a tolerance ε. Tolerances δ and ε are determined by the

acceptable slope changes for each individual boundary condition. An example it provided in the Appendix.

$$i = 0 : C_0 = \frac{X_0 + X_1}{2} \tag{3.4.7}$$

$$i = 1 : C_1 = \frac{X_0 + X_1 + X_2}{3} \tag{3.4.8}$$

$$i = 2, 3, \ldots n-3 : C_i = \frac{X_{i-2} + X_{i-1} + X_i + X_{i+1} + X_{i+2}}{5} \tag{3.4.9}$$

$$i = n-2 : C_{n-2} = \frac{X_{n-3} + X_{n-2} + X_{n-1}}{3} \tag{3.4.10}$$

$$i = n-1 : C_{n-1} = \frac{X_{n-2} + X_{n-1}}{2} \tag{3.4.11}$$

$$SPD = \frac{|X_i - X_{i-1}| + |X_i - X_{i+1}|}{avg\Delta X_i} \tag{3.5.12}$$

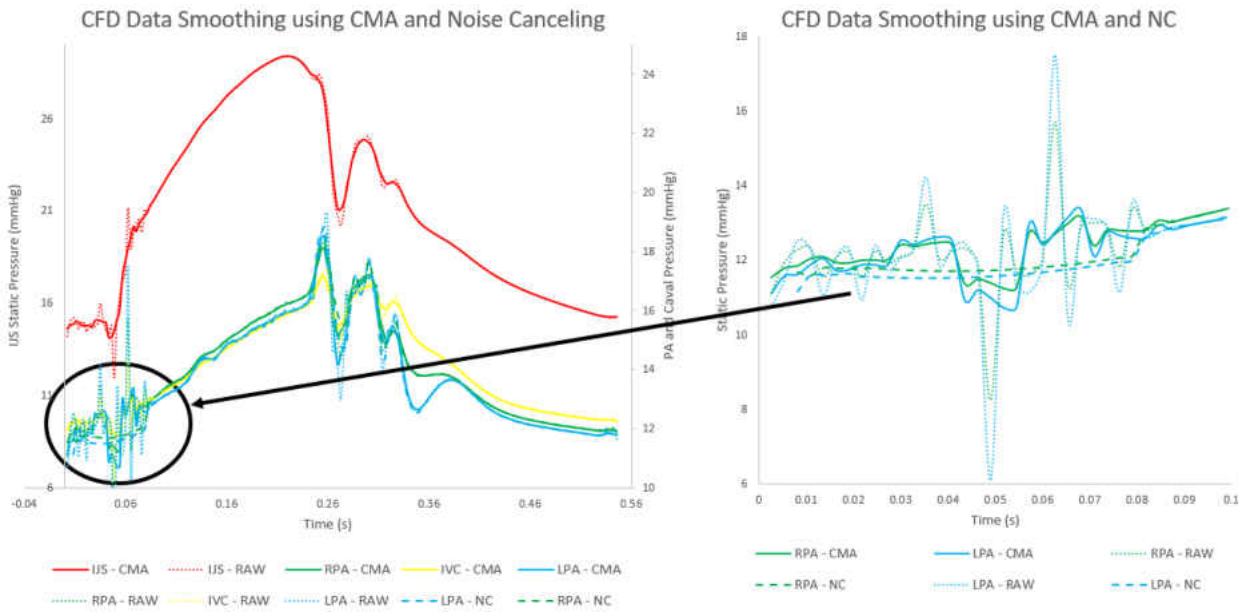

Figure 30: Central Moving Average (CMA) and Noise Cancelation (NC), RAW: Raw Data from CFD.

Since the pressures at the CFD outlets are much larger than the overall driving pressure of the TCPC, special attention at the pressure outlets is required. To prevent complete flow reversal, the outlet pressures are related to each other to force them to remain flow exits.

3.4.4 StarCCM+ Freeze Time

"Freeze time" is a StarCCM+ option that will keep the solution at the current time step while still allowing the user to change the boundary conditions. During the multi-scale model algorithm, StarCCM+ will save two boundary condition values, the initial guess, and the final converged value. An example of this tool is provided in Figure 31.

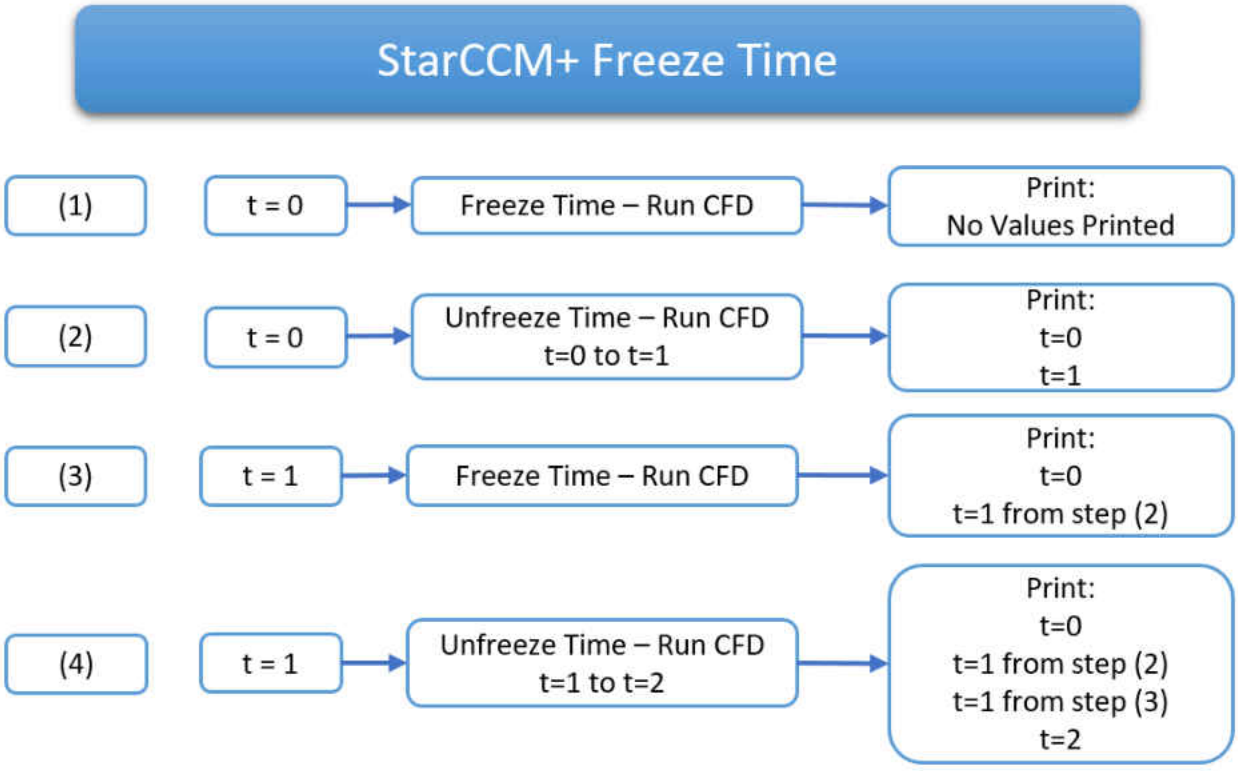

Figure 31: StarCCM+ Freeze Time Example.

CHAPTER 4: RESULTS AND DISCUSSION

4.1 Tube Entrainment Flow Study

Similar to Venturi fluid jets, like the one in Figure 32 [44], we hypothesized that an entrainment jet would cause a suction (pressure drop) at the main inlet [68][69][70][71]. To this end a simple 3D CFD model was created to study pressure changes caused by flow entrainment. A solid model was created in SolidWorks and the mesh was created in StarCCM+.

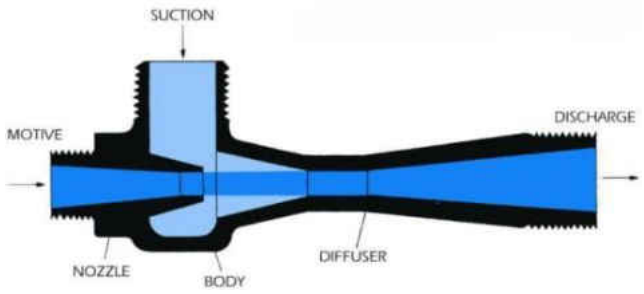

Figure 32: Venturi Fluid Jet [44].

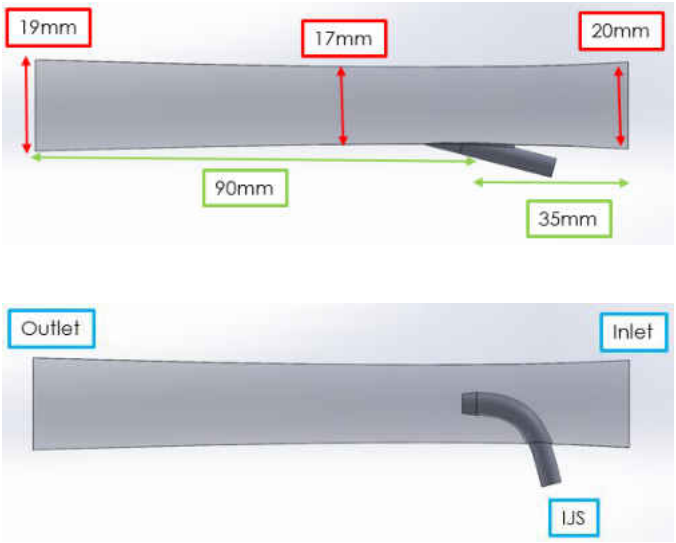

Figure 33: Tube Entrainment Geometry, Top: Outer IJS, Bottom: Inner IJS.

The inlet and outlet diameter are 20[mm] and 19[mm] respectively, the nozzle is 4.75[mm] in diameter, and the length of the model is 125[mm], displayed in Figure 33. The blood density and viscosity were set to 1060[$\frac{kg}{m^3}$] and 0.004[Pa-s] respectively. The boundary conditions consisted of a stagnation pressure inlet, mass flow inlet (entrainment nozzle), and static pressure outlet.

Table 5: Tube Entrainment Results. Po: Stagnation Pressure, Ps: Static Pressure, Q: Flow Rate.

	Boundary Conditions				CFD Calculation				
	mmHg	mmHg	mmHg	L/min	mmHg	L/min	L/min	mmHg	
	Ps Drop Inlet	Po Inlet	Ps Outlet	Q IJS	Ps Inlet	Q Outlet	Q Inlet	Ps IJS	Qout/Qin
Baseline	-	15.045	15	0	15.025	1.179	1.179	-	1
Inner IJS	0.013	15.045	15	0.585	15.012	2.017	1.431	16.392	1.409
Outer Wall IJS	0.01	15.045	15	0.585	15.015	2.091	1.506	15.641	1.388

Three simulations were completed, **(1)** a baseline simulation with no flow through the entrainment inlet, **(2)** an inner IJS model with the IJS nozzle in the center of the flow area, **(3)** and an outer IJS attached to the outside wall at a low angle with respect to the flow direction. The boundary condition setup and calculations are provided in Table 5. The entrainment inlet caused a static pressure drop of ~0.013[mmHg] at the main inlet, and was maximized using the inner IJS over the outer IJS configuration. Static pressure and velocity contours of the entrainment simulations are provided in Figure 34 through Figure 38. There is a clear observation of decreased static pressure within the tube, especially where the flow has high velocity due to the entrainment inlet. In both configurations, the IJS shows small signs of flow obstruction. For the intruding IJS, there is flow recirculation behind the intruding jet, shown in Figure 37. The external jet causes high shear where it impinges on the opposite wall, displayed in Figure 38. In conclusion, the inner IJS entrainment inlet caused a larger pressure drop at the main inlet.

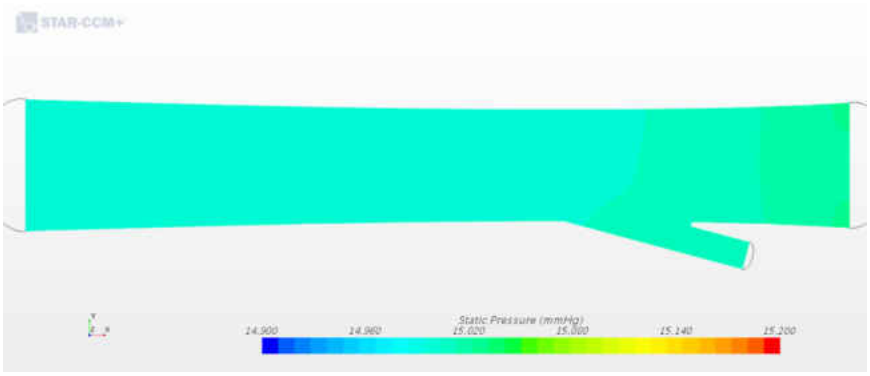

Figure 34: Contours of Static Pressure – No Entrainment.

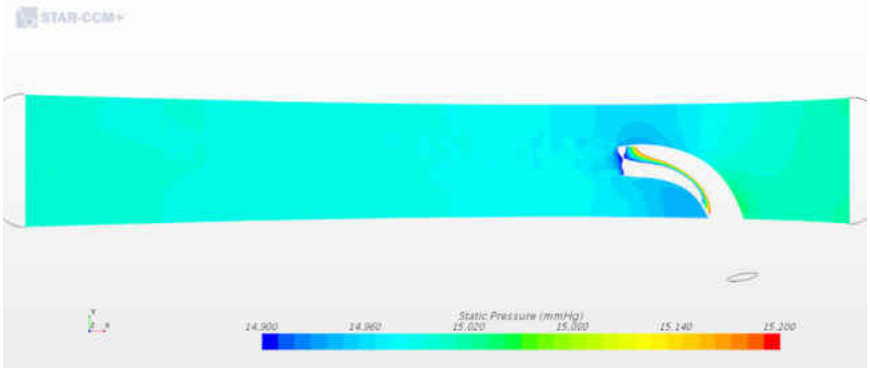

Figure 35: Contours of Static Pressure – Inner IJS.

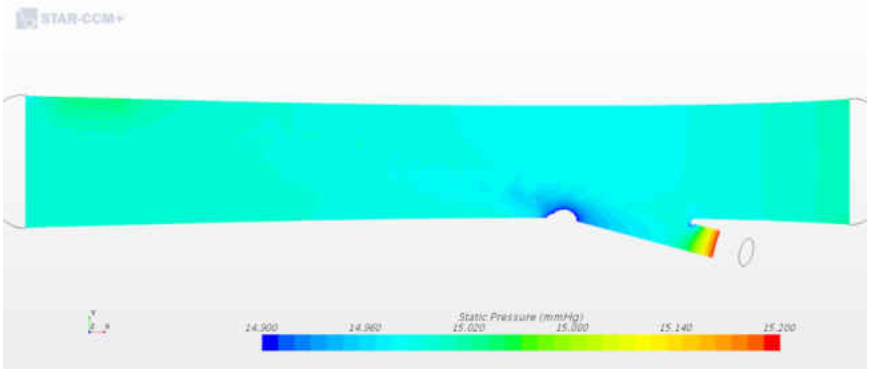

Figure 36: Contours of Static Pressure Outer IJS.

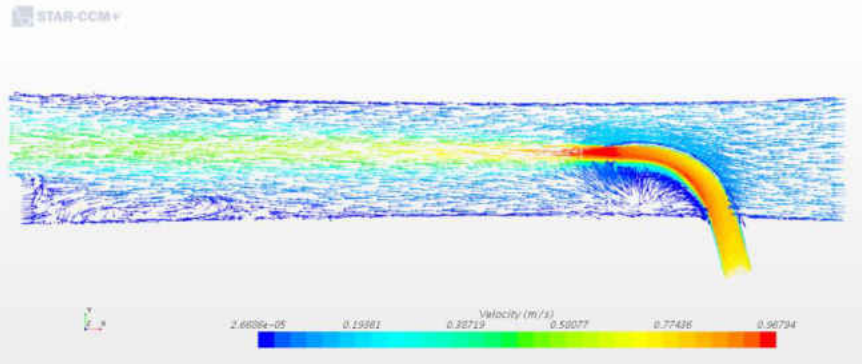

Figure 37: Velocity Vector Magnitude – Inner IJS.

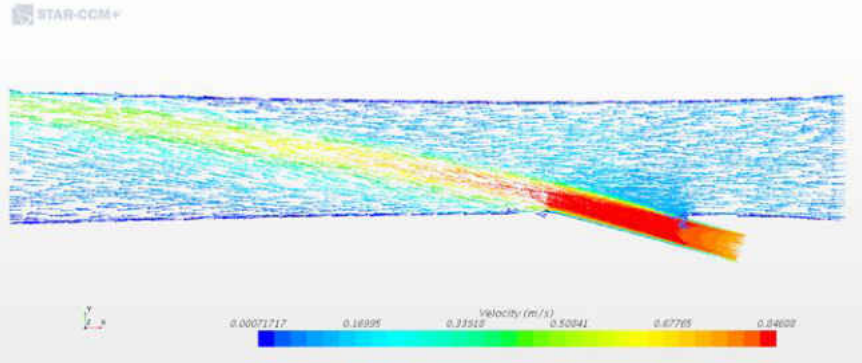

Figure 38: Velocity Vector Magnitude – Outer IJS.

4.2 Closed Loop Steady State Optimization Model

Full multi-scale unsteady models require extensive computer resources and calculation time. In these cases, the optimal injection jet shunt (IJS) shape and positioning is unknown, and the computer resources and calculation time was limited. To reduce the amount of full multi-scale unsteady simulation calculations, a steady state model was created to find the optimal geometry and position of the injection jet shunt within the Fontan circulation. Optimization of the IJS parameters was based on maximizing static pressure drop in the IVC. A 3D model of the Fontan circulation was created using SolidWorks, shown in Figure 39. The total cavopulmonary connection (TCPC) was modeled using average measurements from Fontan patients, shown in Figure 4, [3][5][7].

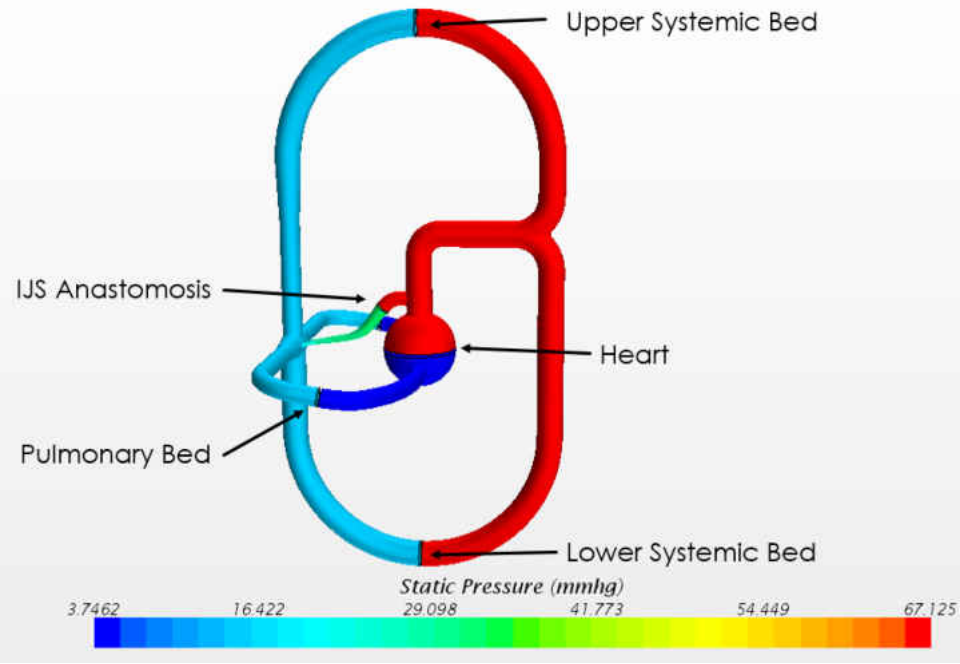

Figure 39: 3D Model of the Closed Loop Steady State Model.

The CFD model was created in StarCCM+. The model was assumed to be incompressible, steady state, Newtonian, and laminar. The density of blood was set at 1060[$\frac{kg}{m^3}$] and the viscosity was set to 0.004[Pa-s]. To model the rest of the hemodynamic circulation, porous walls were used to simulate vascular resistance for the angle of anastomosis of the IJS to the aorta, pulmonary bed, upper systemic bed, and lower systemic bed, shown in Figure 39. The heart was modeled by using a mass flow inlet and a pressure outlet. The mass flow inlet controlled cardiac output, and the pressure outlet controlled the reference pressure. A tetrahedral mesh, displayed in Figure 40, converged to the values shown in Table 6. The optimal Venturi ratio from Table 11 is also included in these simulations.

Table 6: Closed Loop CFD Mesh Details.

Section	Fontan	Low Heart	Top Heart	IVC-Porous	SVC-Porous	LPA-Porous	RPA-Porous
Cells	538224	302000	308503	2469	2431	1275	1269

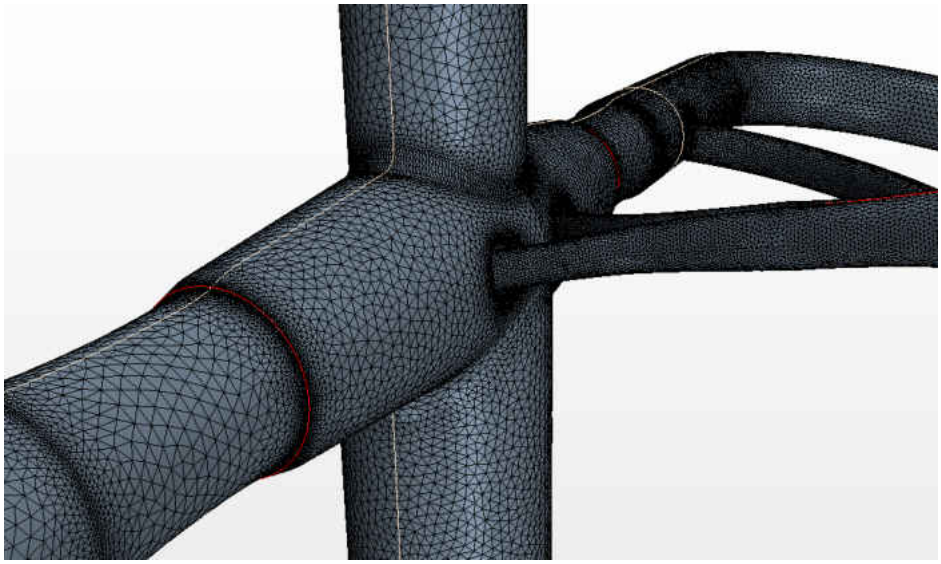

Figure 40: Tetrahedral Mesh of Fontan Section with IJS in StarCCM+.

The system parameters (porous walls, IVC pressure, mass flow inlet, and pressure outlet) were tuned to match average Fontan circulation patient data. Since the model is steady state, these values were taken at the mean, displayed in Table 7.

Table 7: Closed Loop Guiding System Conditions.

	Target	Actual
Cardiac Output	2.1[L/min]	2.1[L/min]
Atrium Pressure	7.0[mmHg]	7[mmHg]
IVC Pressure	16.5[mmHg]	16.43[mmHg]

To find optimum IJS nozzle size, the diameter was varied between 1[mm] and 5[mm] with 1[mm] increments. The baseline model (no IJS) was compared against these different IJS nozzle diameter models. To isolate the effect that IJS entrainment has on IVC pressure, the cardiac output was

kept at 2.1[L/min]. The results are displayed in Table 8. The optimum nozzle distance from the TCPC is presented in Table 9.

Table 8: Nozzle Size Optimization Results. IVC: Inferior Vena Cava, Ps: Static Pressure, Qs: Systemic Flow, Q-IJS: Injection Jet Flow, Q-CO: Cardiac Output, Qp/Qs: Pulmonary to Systemic Flow Ratio, Q-SVC: Superior Vena Cava Flow, Q-IVC: Inferior Vena Cava Flow.

	mmHg	mmHg	mmHg	L/m	L/m	L/m		L/m	L/m
Model	IVC	Low Heart	IVC Ps Drop	Qs	Q-IJS	Q-CO	Qp/Qs	Q-SVC	Q-IVC
Baseline	16.430	7.000	0.000	2.100	0.000	2.100	1.000	0.656	1.435
1mm	16.430	7.000	-0.010	1.960	0.125	2.085	1.064	0.000	0.000
2mm	15.700	7.000	0.720	1.520	0.570	2.090	1.375	0.477	1.052
3mm	15.510	7.000	0.910	1.090	1.010	2.100	1.927	0.351	0.831
4mm	16.030	7.000	0.390	1.230	0.889	2.119	1.723	0.382	0.820
5mm	16.180	7.000	0.240	1.160	0.920	2.080	1.793	0.369	0.803

Table 9: Nozzle Distance from TCPC Results. IVC: Inferior Vena Cava, Ps: Static Pressure, Qs: Systemic Flow, Q-IJS: Injection Jet Flow, Q-CO: Cardiac Output, Qp/Qs: Pulmonary to Systemic Flow Ratio, MR: Momentum Ratio, MG: Momentum Gained.

	mmHg	mmHg	L/min	L/min	L/min	-	-	kg-m/s^2
3mm Results	Ps-IVC	Ps-Drop	Qs	Q-IJS	Q-CO	Qp/Qs	MR	MG
Nozzle Distance From TCPC Connection								
10mm from TCPC	15.908	0.512	1.340	0.760	2.100	1.567	0.304	0.366
15mm from TCPC	15.859	0.561	1.347	0.752	2.099	1.559	0.312	0.370
20mm from TCPC	15.908	0.512	1.324	0.776	2.101	1.586	0.289	0.362

From these results, it was observed that the 3mm diameter nozzle had the optimal effect on IVC pressure drop at 0.910[mmHg]. This result is much lower than the anticipated goal of a 4-5[mmHg] IVC pressure drop; however this steady state model does not account for pulsatility and PVR reduction due to increased pulmonary flow [26][28][34]. The optimum nozzle distance from the TCPC was determined to be 15[mm]. This closed loop steady state model was also used to investigate different approaches to reduce IVC pressure with a 3mm diameter nozzle for the IJS. These approaches are detailed in the following sections, and the results are compiled in Table 10 and Table 12. All these models include the optimal 3mm diameter IJS, optimal 15[mm] nozzle to TCPC distance and 0.19 Venturi area ratio from Table 11.

4.2.1 *Offset of the IVC by 50% Toward the LPA*

To reduce flow impingement and energy losses from the SVC and IVC connection to the pulmonary arteries, the IVC is not anastomosed colinearly with the SVC. Instead, it is offset from the SVC toward the LPA. In this test case, the offset is 50%, illustrated in Figure 41 and Figure 46. The pressure drop in the IVC was improved to 0.920[mmHg], shown in Table 10, as compared to 0.910[mmHg] without the offset.

Figure 41: Offset of the IVC by 50% toward the LPA.

4.2.2 *An IVC Return to the Atrium (Fenestration)*

Another remedy for reducing IVC pressure is letting a portion of the systemic flow bypass the pulmonary system by connecting the IVC to the atrium. This procedure is known as “fenestration”. This model was created by adding a shunt between the IVC and atrium, shown in Figure 42. This shunt also contained a porous wall that controlled the amount of return flow from the IVC to the atrium. The results, in Table 10, include an “IVC-Return” and an “IVC-Return Tuned” model. The “IVC-Return” model contained no porous resistance in the return shunt. To find the required return flow to cause a significant pressure drop in the IVC, the “IVC-Return Tuned” model had a porous wall within the return

shunt. Its resistance was tuned to cause a pressure drop in the IVC close to ~3.2[mmHg]. The calculated return flow was 0.287[L/min].

Figure 42: IVC Return to the Atrium.

4.2.3 A Pulmonary Return to the Atrium

IVC pressure can also be reduced by adding a pulmonary return system to the atrium. The model was created by adding return shunts from both the RPA and LPA distal to the IJS, shown in Figure 43. This is not a known procedure, but this system will remove the extra mass injected into the system from the IJS to cause higher pressure drops and entrainment effects. Three different setups were used in these simulations. The “PA – Return” model had no porous resistance in the return shunts, the “PA – Return – Tuned” model tuned the porous resistance in the return shunts to cause a ~3.2 mmHg IVC pressure drop, and the “PA – Return – No IJS” model removed the IJS to isolate the pulmonary return effect. The calculated return flow was 0.285[L/min], which is close to the 0.287[L/min] required for the IVC return model, displayed in Table 10. Moving the return to the pulmonary arteries from the IVC did not have a significant effect on return flow, but it did positively affect the hemodynamic flow field, shown in Figure 48. The “PA – Return – No IJS” model reinforced the IJS entrainment effects calculated

in Table 8. Removing the IJS caused the IVC pressure to increase from 13.15[mmHg] to 14.01[mmHg], which is approximately the 0.910[mmHg] pressure drop caused by the 3[mm] IJS.

Figure 43: Pulmonary Return to the Atrium.

The next set of pulmonary return calculations took into consideration the increased cardiac output caused by adding a left to right shunt. The pulmonary to system flow ratio (Qp/Qs) was tuned to 1.5, and the Qs was tuned to 2.1[L/min]. The four model setups included a “PA – Return” model that had no porous resistance in the return shunt, a “ PA – Return – Comparison” model that used the same porous resistance calculated in the previous “PA – Return – Tuned” model, a new “PA – Return – Tuned” model with a porous resistance tuned to reduce IVC pressure by ~3.2[mmHg], and a “PA – Return – No IJS” model with no IJS to isolate the entrainment effect from the return flow. With an increase in cardiac output and Qp/Qs of 1.5, the required return flow was 1.325[L/min], which is larger than the flow of the IJS at 1.068[L/min], displayed in Table 10. The isolated IJS entrainment caused a ~0.56[mmHg] IVC pressure drop, down from the ~0.90[mmHg] found in the previous calculations.

Table 10: Effect of Different Approaches to Reduce IVC Pressure. IVC: Inferior Vena Cava, Ps Drop: Static Pressure Drop in IVC, Qs: Systemic Flow, Q-IJS: Injection Jet Flow, Q-CO: Cardiac Output, Qp/Qs: Pulmonary to Systemic Flow Ratio, Q-SVC: Superior Vena Cava Flow, Q-IVC: Inferior Vena Cava Flow, Q-Return: Return Flow to Atrium, Return R: Porous Resistance Used to Control Return Flow.

	mmHg	mmHg	L/m	L/m	L/m		L/m	L/m	L/m	kg/m^4
3mm Results	Ps-IVC	Ps Drop	Qs	Q-IJS	Q-CO	Qp/Qs	Q-SVC	Q-IVC	Q-Return	Return R
Baseline - No IJS	16.420	0.000	2.100	0.000	2.1	1.000	0.656	1.435	0.000	0.000
IJS - No Mods	15.510	0.910	1.090	1.000	2.09	1.917	0.351	0.757	0.000	0.000
IJS - 50% Offset	15.500	0.920	1.090	0.995	2.085	1.913	0.348	0.758	0.000	0.000
IVC - Return	8.320	8.100	1.102	0.993	2.095	1.901	0.354	0.772	1.067	0.000
IVC - Return - Tuned	13.130	3.290	1.101	0.993	2.094	1.902	0.348	0.757	0.287	80.000
PA - Return	9.590	6.830	1.090	1.004	2.094	1.921	0.348	0.755	0.823	0.000
PA - Return - Tuned	13.150	3.270	1.101	0.993	2.094	1.902	0.348	0.759	0.285	46.000
PA - Return - No IJS	14.015	2.405	2.102	0.000	2.102	1.000	0.666	1.448	0.299	46.000
Cardiac Input Increased to 3.15 L/min and IJS Tuned to Qp/Qs = 1.5										
Pa - Return	12.813	3.607	2.077	1.052	3.129	1.506	0.655	1.433	1.379	0.000
Pa - Return Comparison	21.419	-4.999	2.074	1.065	3.139	1.514	0.655	1.428	0.439	46.000
Pa - Return - Tuned	13.212	3.208	2.073	1.068	3.141	1.515	0.654	1.426	1.325	0.250
Pa - Return - No IJS	13.771	2.649	3.126	0.000	3.126	1.000	0.985	2.152	1.406	0.250

4.2.4 Venturi Effects by Reducing Pulmonary Artery Flow Area

To create a Venturi effect within the Fontan circulation, the pulmonary arteries were given a small reduction downstream from the IJS nozzles, shown in Figure 44. This reduction was measured as a Venturi area ratio which is given in equation 1.

$$(\text{Original Area} - \text{Venturi Area}) / \text{Original Area} \qquad (4.2.1)$$

Figure 44: Venturi Effect by Reducing Pulmonary Artery Flow Area.

In these Venturi optimization simulations a different approach to boundary condition setup was used, the pressure drop method. Rather than imposing a mass flow inlet and pressure outlet for the heart, a pressure drop of 64[mmHg] was imposed between the upper and lower heart. Pressure drops were also used to simulate vascular beds rather than porous walls. The big difference between the two approaches was the ability to control cardiac output, which was difficult in the pressure drop method. The Qp/Qs was also controlled by pressure drops, which is labeled as "IJS Kick" in Table 11, and they were tuned to cause a Qp/Qs of 1.5 in the Venturi cases.

Table 11: Venturi Results with 3mm Diameter IJS Nozzle. V: Venturi, Qj: IJS Flow, Qs: Systemic Flow, Qco: Cardiac Output, Qp: Pulmonary Flow, IVC Shift: IVC Pressure After Shifting Relative to the Reference Pressure, Ps Drop: IVC Static Pressure Drop, Venturi Ratio: (Original Area – Venturi Area) / Original Area, IJS Kick: Pressure Drop Imposed in the IJS Shunt.

	L/min	L/min	L/min		mmHg	mmHg		mmHg
	Qj	Qs	Qco	Qp/Qs	IVC Shift	Ps Drop	Venturi Ratio	IJS Kick
No IJS	0.000	2.180	2.180	1.000	17.854	-	-	-
1.5 mm	0.379	2.600	2.979	1.146	17.723	0.131	-	-
2.0 mm	0.819	3.205	4.024	1.256	17.566	0.288	-	-
2.5 mm	1.363	3.519	4.882	1.387	17.425	0.429	-	-
3.0 mm	2.060	4.280	6.340	1.481	17.230	0.624	-	-
4.0 mm	2.810	3.690	6.500	1.762	17.490	0.364	-	-
2.5 mm V	1.365	3.583	4.948	1.381	17.390	0.464	0.438	-
2.5 mm V	1.440	3.762	5.202	1.383	17.357	0.497	0.438	5.000
2.5 mm V	1.512	3.966	5.478	1.381	17.321	0.533	0.438	10.000
2.5 mm V	1.380	3.790	5.170	1.364	18.132	-0.278	0.438	-
2.5 mm V	1.651	4.110	5.761	1.402	17.230	0.624	0.438	20.000
3.0 mm V	2.070	4.080	6.150	1.507	17.232	0.622	0.438	-
3.0 mm V	2.402	4.689	7.091	1.512	17.096	0.758	0.438	15.000
3.0 mm V	2.070	4.210	6.280	1.492	17.507	0.347	0.306	-
3.0 mm V	2.091	3.965	6.056	1.527	17.014	0.840	0.190	-
3.0 mm V	2.407	4.736	7.143	1.508	17.014	0.840	0.190	15.000

The first section of Table 11 lists the outcomes of different IJS nozzle diameters, which comes to the same conclusion as Table 8. The 3[mm] diameter nozzle out performs the others by creating the largest pressure drop in the IVC. The second part of Table 11 lists the outcomes of the Venturi simulations. These include the 2.5[mm] diameter IJS nozzles, which was second best, and the 3[mm]

diameter nozzles. It was observed that the 3[mm] diameter nozzles still outperformed the 2.5[mm] nozzles with Venturi effects, so the optimization of the area ratio was reduced to 3[mm] diameter nozzles only. The best area ratio was found to be 0.19 for the 3[mm] nozzle. This Venturi area ratio is included in all the tests mentioned in this section.

4.2.5 Reduction in Pulmonary Vascular Resistance (PVR)

An interaction not initially realized was the relationship between PVR and pulmonary flow. The exact relationship between these two parameters is not well known. What is known, is with increased pulmonary flow, the PVR will decrease, [27][28][29][34][38]. Five models were created to find the IVC pressure reduction due to PVR decrease and IJS flow entrainment. One was the baseline (No PVR reduction), and the other 4 were trials to find what PVR reduction was required to cause a ~3.2[mmHg] IVC pressure drop. The PVR was required to drop by 70% to cause a 3.282[mmHg] IVC pressure drop, shown in Table 12. With a Qp/Qs of 1.5, the dobutamine PVR model predicts a 60% PVR drop, shown in Figure 24.

4.2.6 Reduction in PVR to Isolate Entrainment Effects from the IJS

The last set of models used PVR reduction to isolate the IJS entrainment effect. First a baseline model was calculated at a cardiac output of 3.1[L/min], which is the expected outcome of adding an IJS to the baseline model. The PVR was then decreased in the baseline model to match the target IVC pressure of 16.5[mmHg]. This effectively isolates the IJS effect when it is inserted into the Fontan. The IJS entrainment causes a 1.041[mmHg] IVC pressure drop. This is similar to the pulmonary return and diameter optimization calculations of a 0.91[mmHg] pressure drop, shown in Table 12.

Table 12: PVR Reduction and Entrainment Effects of Steady State Model. PVR: Pulmonary Vascular Resistance, PVR-Red: PVR Reduction %, IVC: Inferior Vena Cava, Ps Drop: Static Pressure Drop in IVC, Qs: Systemic Flow, Q-IJS: Injection Jet Flow, Q-CO: Cardiac Output, Qp/Qs: Pulmonary to Systemic Flow Ratio, MR: Momentum Ratio, MG: Momentum Gained.

Baseline Model with Reduction in PA Resistance to Achieve 3 mmHg Pressure Drop in IVC										
	mmHg	mmHg	kg/m^4	-	L/min	L/min	L/min	-	-	kg-m/s^2
3mm Results	Ps-IVC	Ps-Drop	PVR	PVR-Red	Qs	Q-IJS	Q-CO	Qp/Qs	MR	MG
IJS - No PVR Reduction	26.908	-10.488	2.300E+07	NA	2.073	1.068	3.141	1.515	0.358	0.850
IJS - PVR Reduction	9.330	7.090	2.300E+06	90.000	2.073	1.068	3.141	1.515	0.361	0.858
IJS - PVR Reduction	11.891	4.529	5.300E+06	76.957	2.072	1.067	3.139	1.515	0.358	0.850
IJS - PVR Reduction	13.138	3.282	6.750E+06	70.652	2.072	1.068	3.140	1.515	0.357	0.849
IJS - PVR Reduction	21.984	-5.564	1.725E+07	25.000	2.074	1.064	3.138	1.513	0.360	0.849
Resistance Reduction in the Pulmonaries to Match Previous IVC Pressure with Increased Blood Flow										
No IJS Baseline	27.857	-11.437	2.300E+07	0.000	3.127	0.000	3.127	1.000	-	-
No IJS - 59% PVR Reduction	16.426	0.000	9.430E+06	59.000	NA	3.136	0.000	3.136	-	-
IJS - 59% PVR Reduction	15.385	1.041	9.430E+06	59.000	NA	2.072	1.069	3.141	0.359	0.855

4.2.7 Pulmonary Artery Expansion

Actual pulmonary arteries are not rigid, in fact they expand with increasing flow and pressure. To simplify this effect, without implementing fluid structure interaction (FSI), the pulmonary artery radius was extended by 10.668% all the way to the atrium of the heart. This 10.668% expansion was determined with the use of Poiseuille flow, $\frac{Qi}{Qf} \sim (\frac{ri}{rf})^4$, and assuming the pulmonary artery wall will expand to accommodate a flow increase of 50%. Where Q is the flow rate and r is the radius. Expanding the pulmonary arteries dropped the IVC pressure by 3.970[mmHg], but this expansion effectively reduced the PVR as well, shown in Table 13.

Table 13: Expansion of Pulmonary Artery Radius by 10.668% Results. Ps: Static Pressure, IVC: Inferior Vena Cava, Ps Drop: Static Pressure Drop in IVC, PVR-Red: PVR Reduction %, Qs: Systemic Flow, Q-IJS: Injection Jet Flow, Q-CO: Cardiac Output, Qp/Qs: Pulmonary to Systemic Flow Ratio, MR: Momentum Ratio, MG: Momentum Gained, EE: Energy Efficiency, EL: Energy Loss.

	mmHg	mmHg	-	L/min	L/min	L/min	-	-	kg-m/s^2	-	mW
3mm Results	Ps-IVC	Ps-Drop	PVR-Red	Qs	Q-IJS	Qco	Qp/Qs	MR	MG	EE	EL
10.668% Pulmonary Artery Radius Increase											
IJS - No PA Expansion	15.385	1.041	59.000	2.072	1.069	3.141	1.516	0.359	0.855	0.718	42.187
IJS - PA Expansion	12.450	3.970	59.000	2.077	1.068	3.145	1.514	0.325	0.855	0.677	41.917
No IJS - PA Expansion	13.300	3.120	59.000	3.115	0.000	3.115	1.000	-	-	0.986	1.324
NES - PA Expansion	13.636	2.784	59.000	2.038	1.115	3.152	1.547	0.074	0.398	0.728	34.338

4.2.8 Flow Field Comparison

The flow fields of these steady state simulations were also studied by observing the velocity streamlines and static pressure along the fluid domain in the baseline IJS (Figure 45), 50% offset (Figure 46), IVC return (Figure 47), and pulmonary return (Figure 48) models. As expected, the 50% offset model (Figure 46) successfully reduces flow impingement and recirculation at the SVC to IVC connection as compared to the collinear connection (Figure 45). The IVC return reduces recirculation in the IVC, but the RPA and LPA still show signs of recirculation, displayed in Figure 47. The pulmonary return reduced swirl and circulation in the LPA and RPA by siphoning off the extra energizing flow, illustrated in Figure 48.

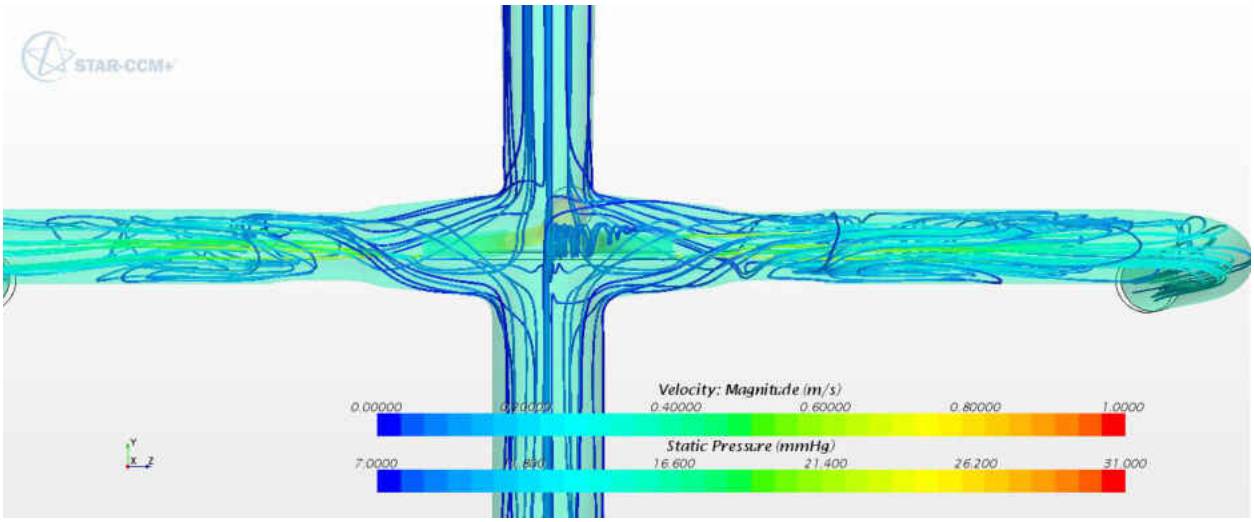

Figure 45: Baseline IJS Flow Field.

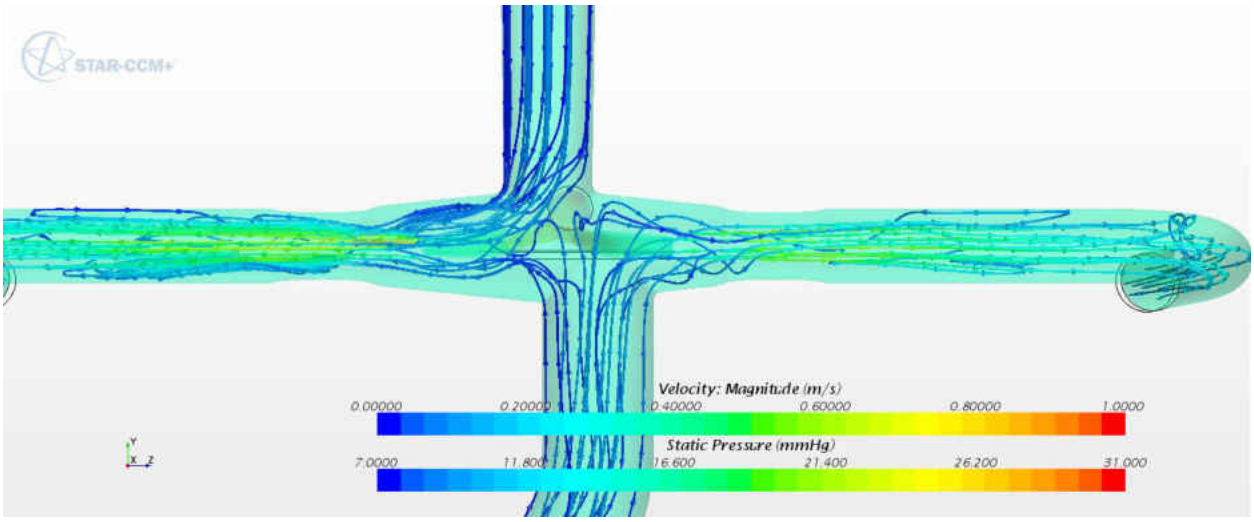

Figure 46: 50% Offset Flow Field.

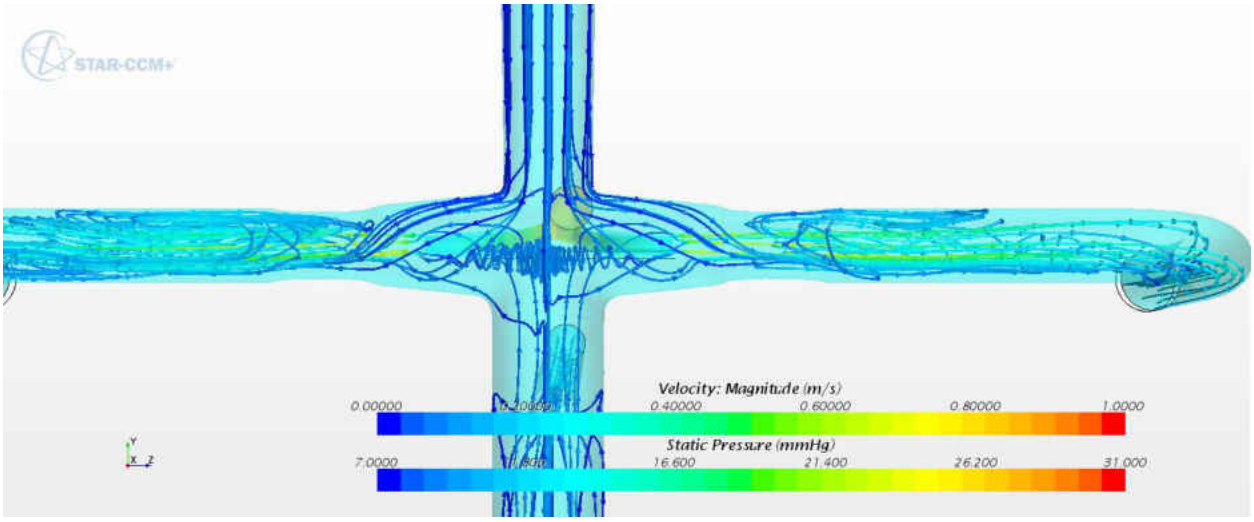

Figure 47: IVC Return (Fenestration) Flow Field.

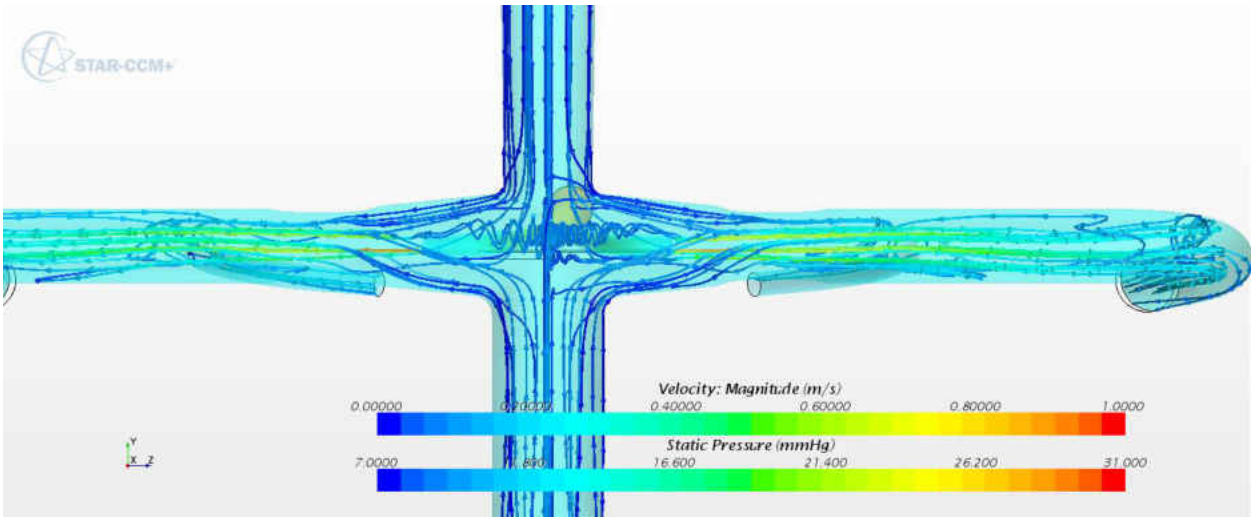

Figure 48: Pulmonary Artery Return Flow Field.

4.3 Simple IJS Model for Multi-Scale Model Development

During the development of the multi-scale model, a simplified Fontan IJS circuit was created to speed up the debugging and testing process. The simplified IJS LPM was trimmed from 28 ODEs to 12 ODEs, illustrated in Figure 21, and tuned to Fontan physiological values, shown in Table 14. The 3D model for the CFD was also simplified from a three inlet (IVC, SVC, IJS) two outlet (RPA, LPA) system, to a two inlet (IVC+SVC, IJS) one outlet (LPA+RPA) system, shown in Figure 49. The multi-scale model successfully converged to a stable solution after 17 heart cycles, shown in Figure 50. IJS flow was then increased to confirm stability within the multi-scale model algorithm. As expected the pressure pulsatility rises significantly, shown in Figure 51.

Table 14: Simple IJS Mean Values

Simple IJS Mean Values					
Cardiac Output	2.211	L/min	Graft Flow	0	L/min
LPA Flow	1.046	L/min	Coronary Flow	0.143	L/min
RPA Flow	1.046	L/min	TCPC Pressure	16.283	mmHg
IVC Flow	1.278	L/min	IVC/SVC Split	1.584	
SVC Flow	0.806	L/min	QP/QS	1	

Figure 49: Simplified IJS 3D Geometry for CFD.

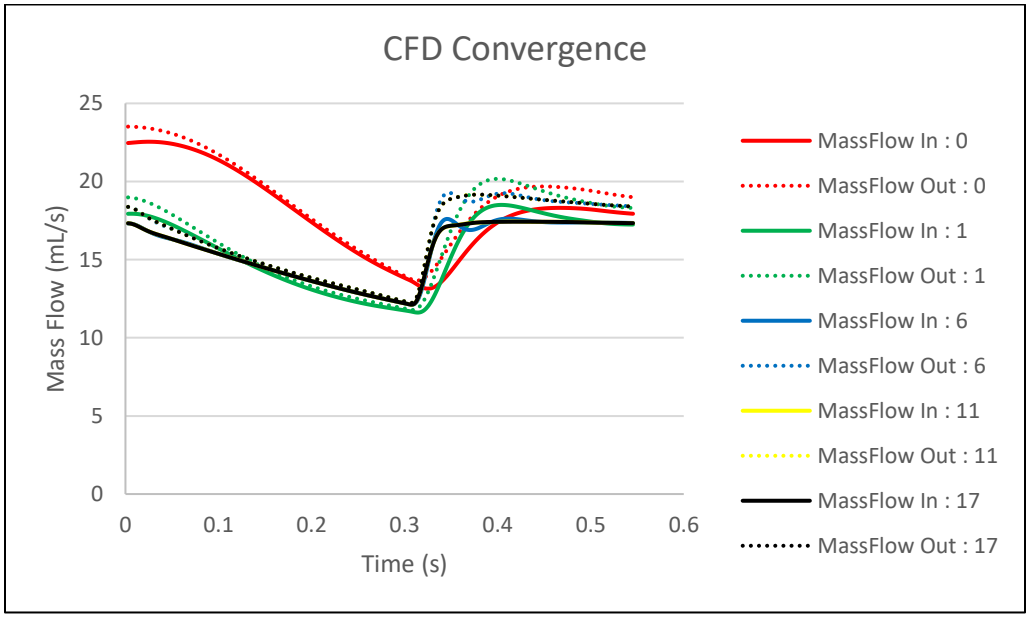

Figure 50: Convergence of the Simplified IJS Model. 0: Cycle 0, 1: Cycle 1, etc.

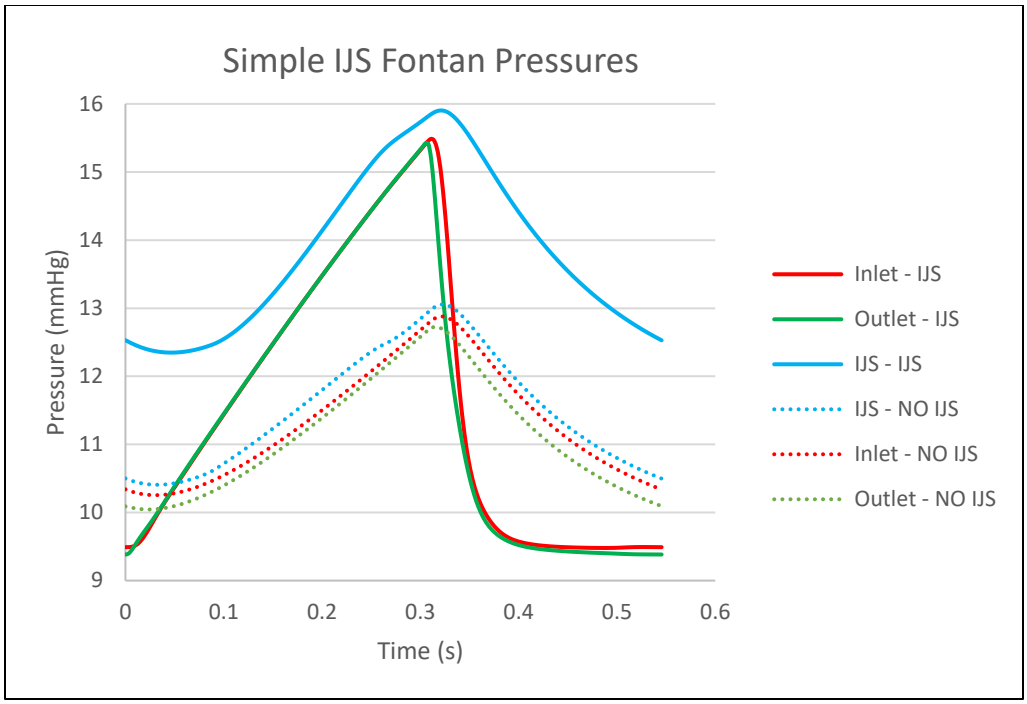

Figure 51: Simplified IJS Pressures.

4.4 Lumped Parameter Model Tuning

The LPM for each model is tuned to the physiological cardiac output and pressure wave forms. This procedure is explained in section 3.2. The converged LPM results for the synthetic model are shown in Figure 52 through Figure 54. The heart wave forms were tuned to match pressures from documented patient data in Table 3. The wave forms of the heart pressures are compared against physiological wave forms in Figure 52. The LPM was also tuned to closely match aorta flow wave forms, displayed in Figure 53, and TCPC wave forms, shown in Figure 54. In the TCPC, the flow rates are offset from the pressures. The max flow rates occur during diastole, and flow rates are at a minimum during systole. This phenomenon was captured by the LPM. This same procedure was carried out in all the CHOP models. However, the CHOP models also have detailed flow data captured by the MRI scans from section 3.1.3.

The capacitance and inductance values throughout the circuit are modified to match up with the MRI flow wave forms for the CHOP-1 and CHOP-6 models in Figure 55.

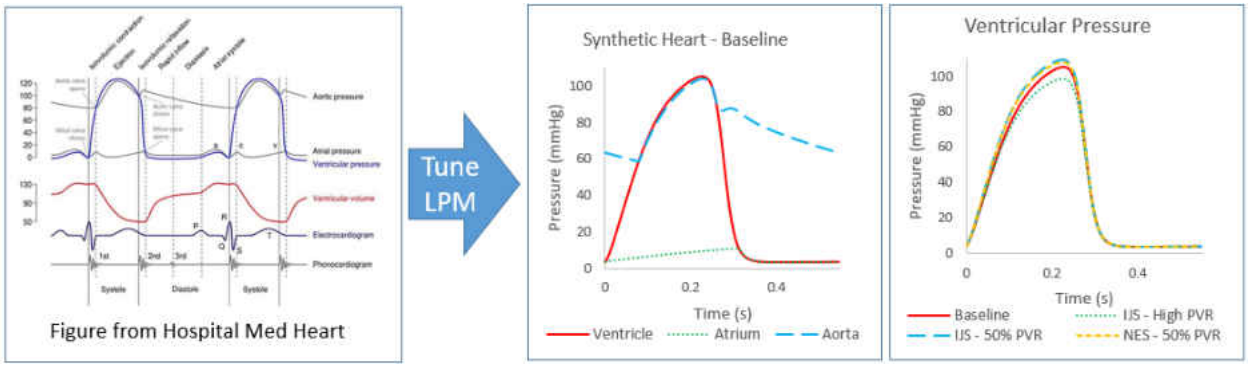

Figure 52: Synthetic Model Tuned Heart Wave Forms. Left: Heart Pressures from Hospital Med Heart, Right: Tuned LPM Heart Pressures.

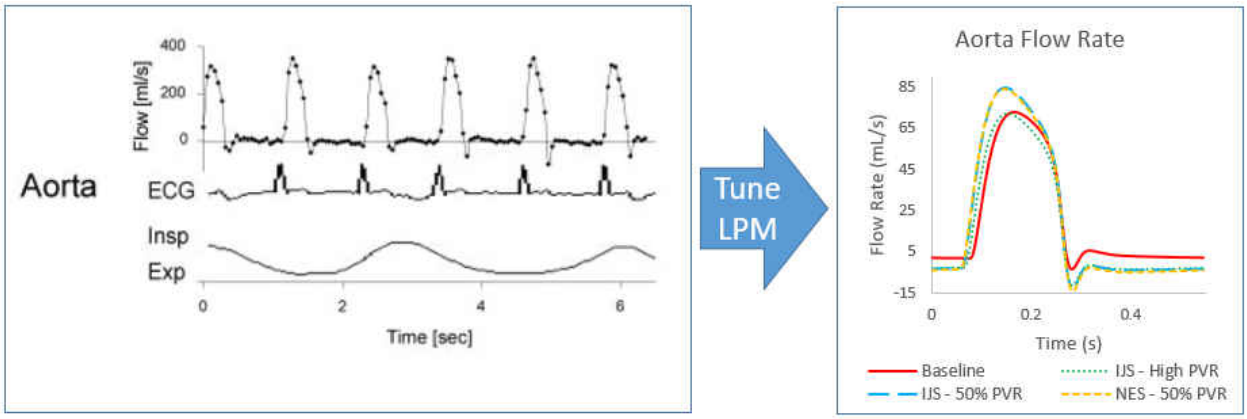

Figure 53: Synthetic Model Tuned Aorta Flow Wave Forms. Left: MRI Data from Fontan Patient [72], Right: Tuned LPM Aorta Flow Rates.

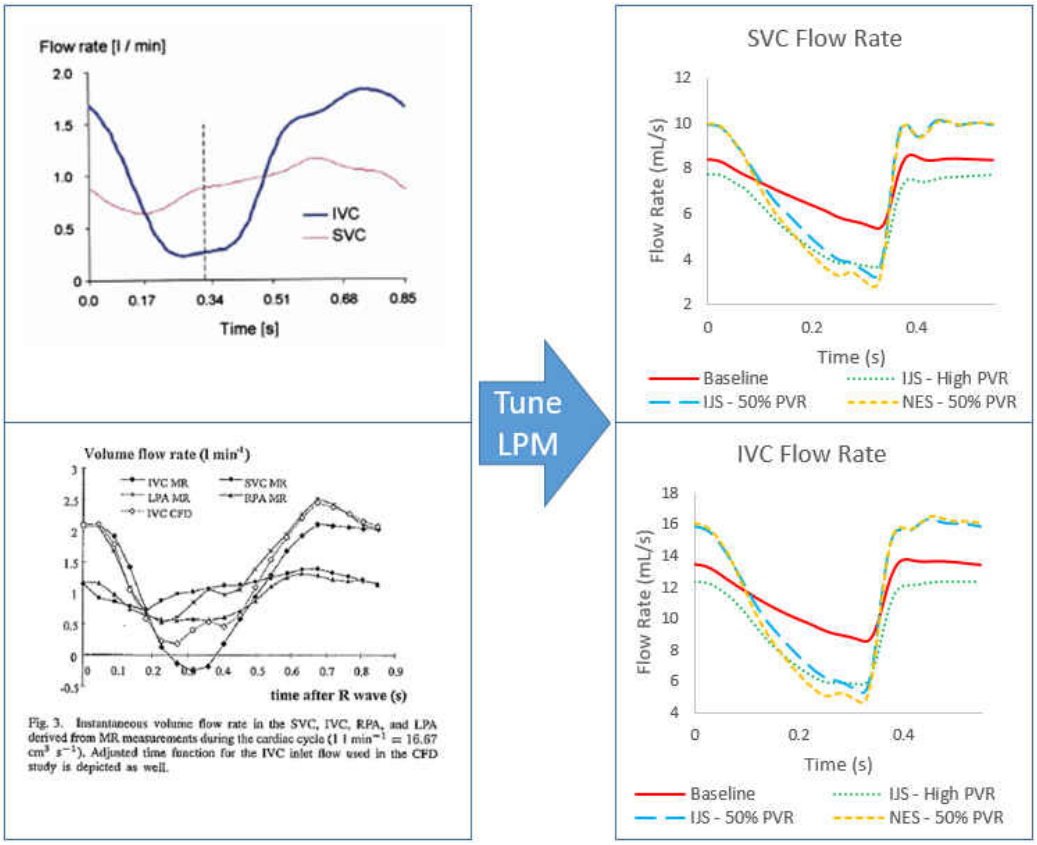

Fig. 3. Instantaneous volume flow rate in the SVC, IVC, RPA, and LPA derived from MR measurements during the cardiac cycle (1 l min^{-1} = 16.67 cm^3 s^{-1}). Adjusted time function for the IVC inlet flow used in the CFD study is depicted as well.

Figure 54: Synthetic Model Tuned TCPC Flow Wave Forms. Top Left: IVC and SVC Flow Rates of a Fontan Circulation [54], Bottom Left: TCPC Flow Rates of a Fontan Circulation [3], Right: SVC and IVC Flow Waves Forms from the Tuned Converged LPM Circuit.

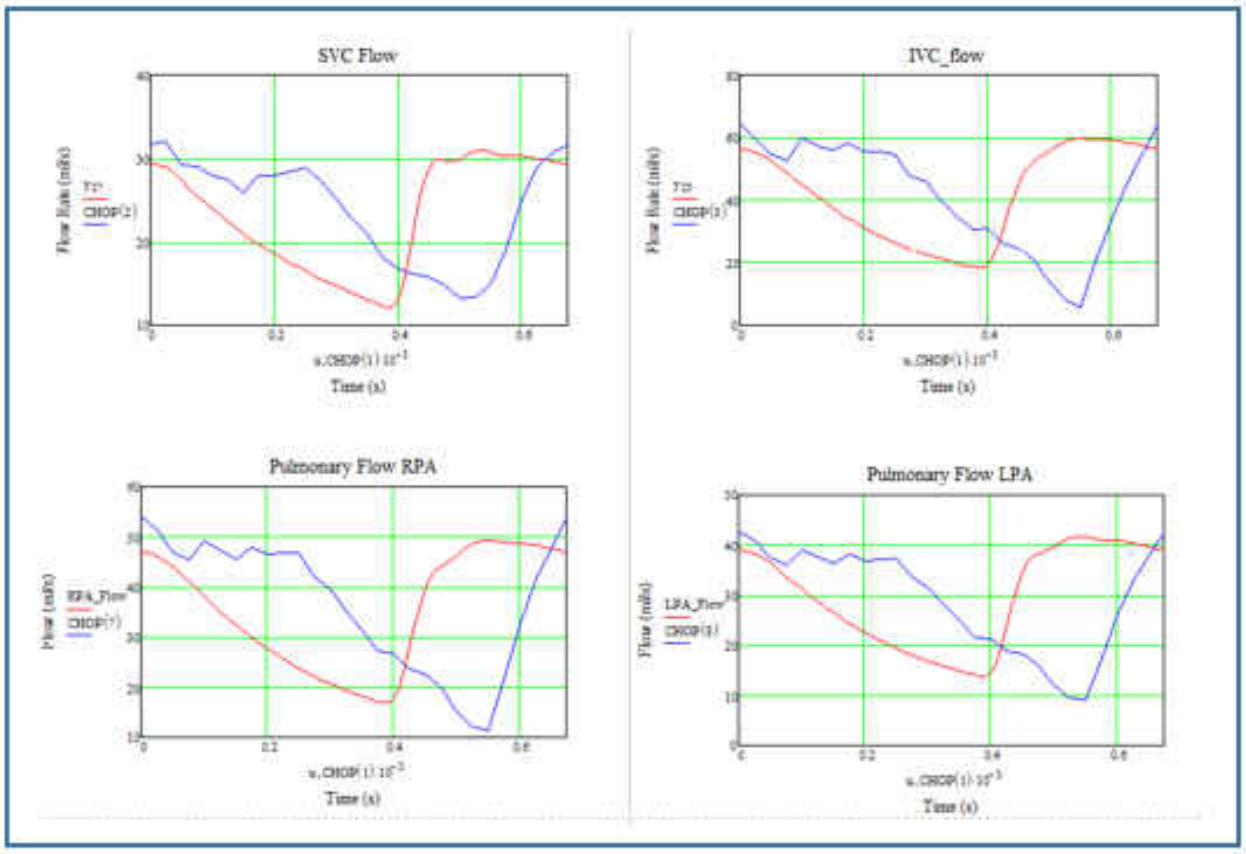

Figure 55: LPM (Red) to CHOP-1 MRI (Blue) Flow Rate Tuning Comparison.

4.5 Synthetic Simulation

Five configurations for the synthetic model were analyzed using multi-scale analysis. The five configurations are a baseline, an IJS with no PVR reduction, an IJS, a NES, and an IJS with pulmonary expansion model. The converged CFD and LPM boundary conditions for the 5 synthetic models are illustrated in Figure 56 and Figure 57.

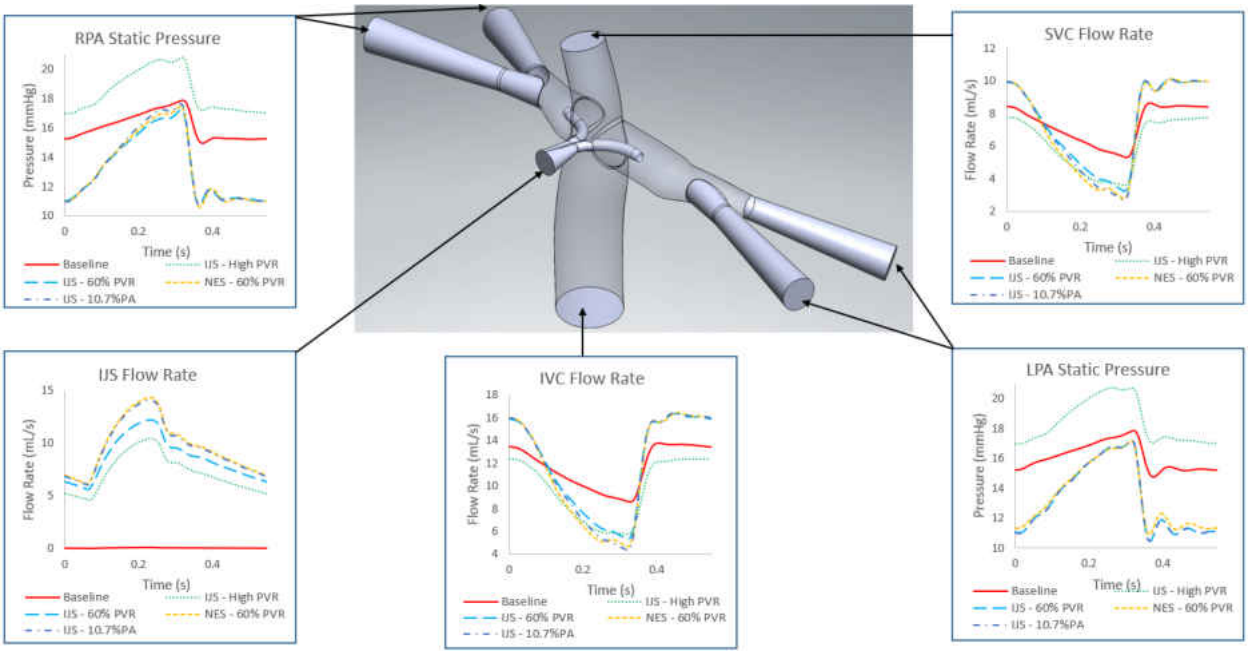

Figure 56: Synthetic Model: Converged CFD Boundary Conditions.

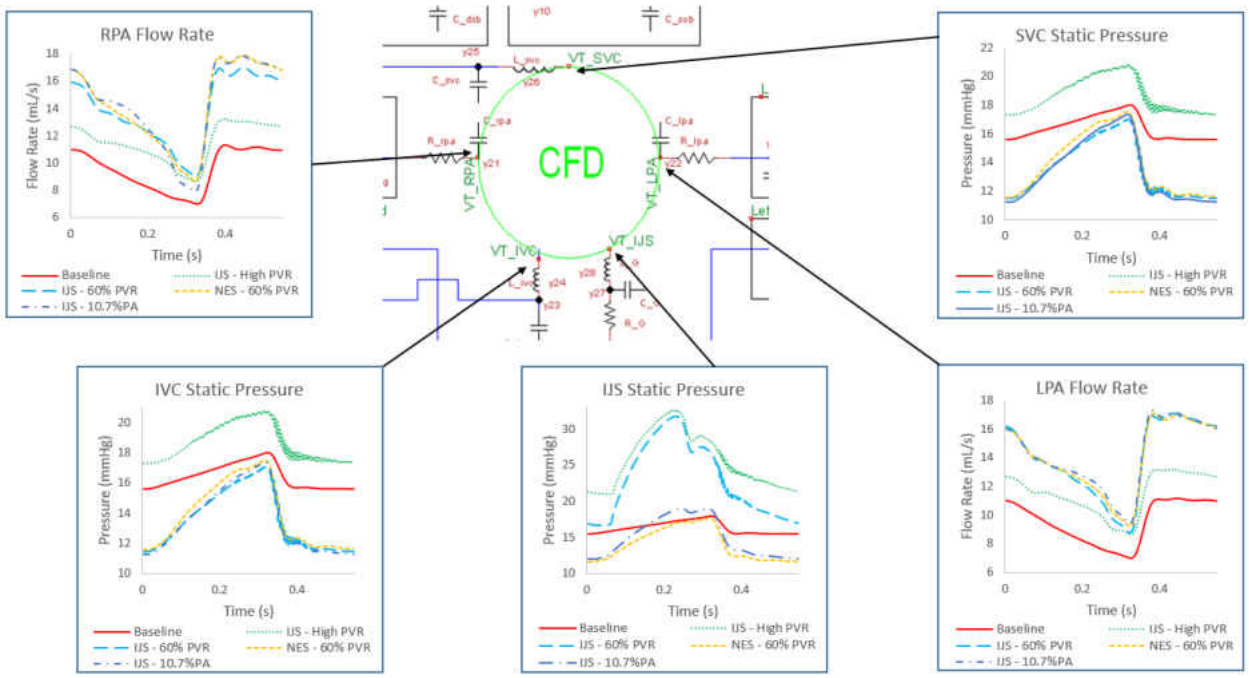

Figure 57: Synthetic Model: Converged LPM Boundary Conditions.

Velocity streamlines for peak systole, early diastole, mid diastole, and late diastole are compared against the baseline model in Figure 59 to Figure 62. During peak systole, the IJS flow is at its maximum and causes some flow re-circulation proximal to the nozzle tip. This is a result of the rigid walls constraining the flow of an incompressible fluid. This phenomenon severely hinders the entrainment effect. The overall pulmonary expansion model was created to help alleviate the rigid wall constriction. However, the pulmonary artery expansion model also exhibits this behavior. To accurately capture the full entrainment effect, the walls need to expand dynamically with flow. This phenomenon can be captured by using fluid structure interaction (FSI) and assuming the walls are not rigid. The IJS also benefits the system by directing the flow of the SVC and IVC toward the pulmonary arteries away from the TCPC. The NES, that was attached to the outside wall perpendicular to the flow direction, caused large re-circulations and stagnation flow regions in the TCPC.

Increased wall shear stress (WSS) can also cause energy losses resulting in lower entrainment efficiency. The WSS of the IJS model is compared against the NES model for peak systole, early diastole, mid diastole, and late diastole in Figure 58. The NES and IJS configurations both cause high levels of shear stress concentrations around 200[dyne/cm^2]. Since normal average physiological values are about 20[dyne/cm^2] [74], this is cause for concern.

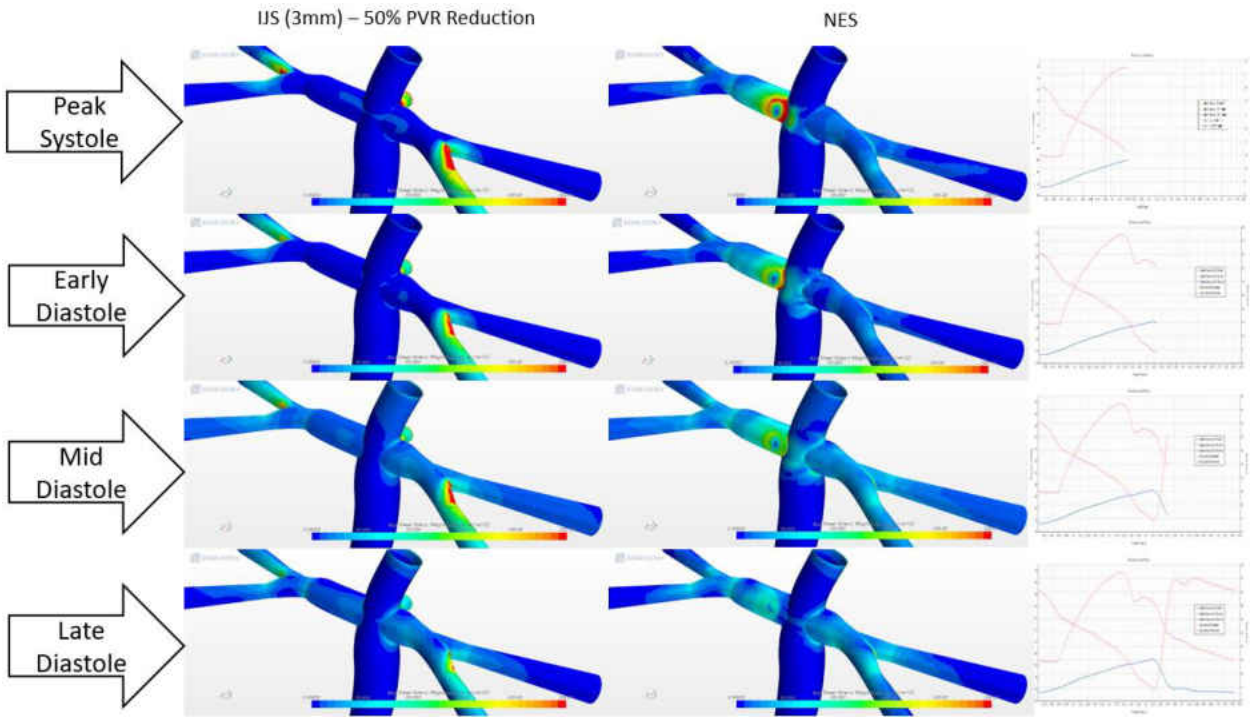

Figure 58: Synthetic Model: Wall Shear Stress Comparison Between the IJS and NES.

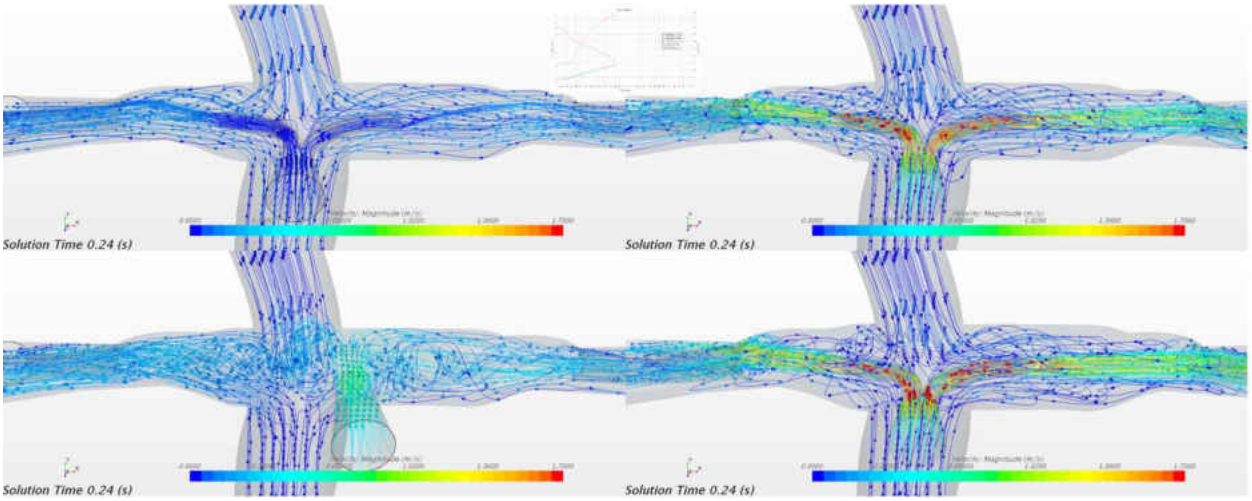

Figure 59: Synthetic Model: Velocity Streamlines at Peak Systole. Top Left: Baseline, Top Right: IJS, Bottom Left: NES, Bottom Right IJS with 10.7% Pulmonary Artery Expansion.

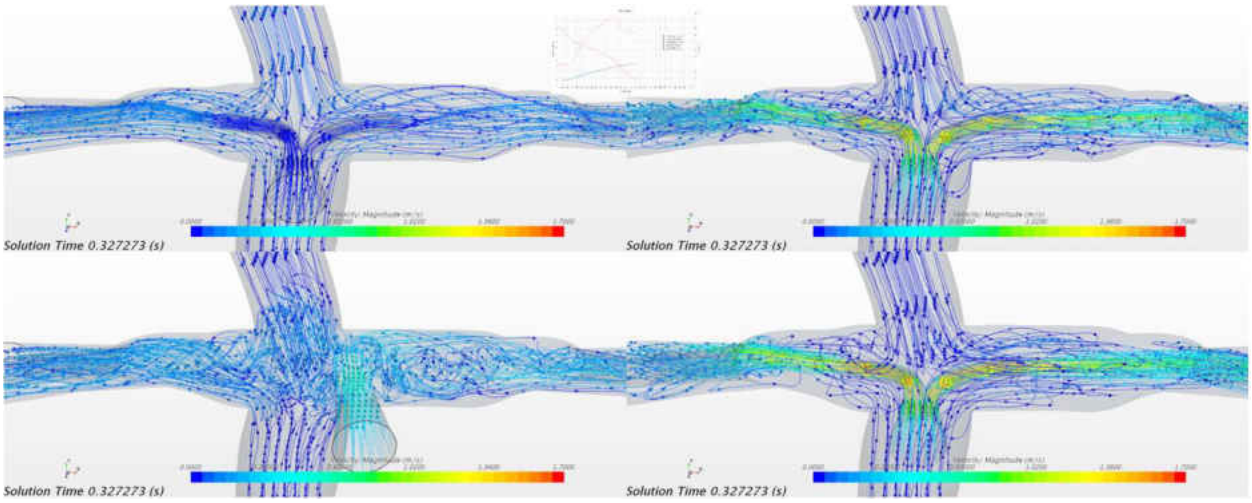

Figure 60: Synthetic Model: Velocity Streamlines at Early Diastole. Top Left: Baseline, Top Right: IJS, Bottom Left: NES, Bottom Right IJS with 10.7% Pulmonary Artery Expansion.

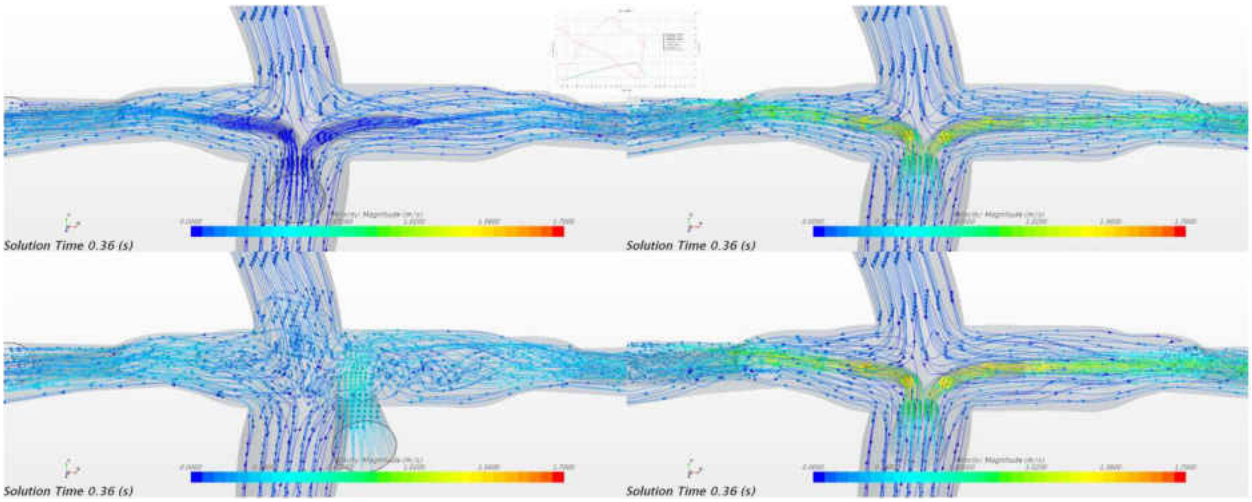

Figure 61: Synthetic Model: Velocity Streamlines at Mid Diastole. Top Left: Baseline, Top Right: IJS, Bottom Left: NES, Bottom Right IJS with 10.7% Pulmonary Artery Expansion.

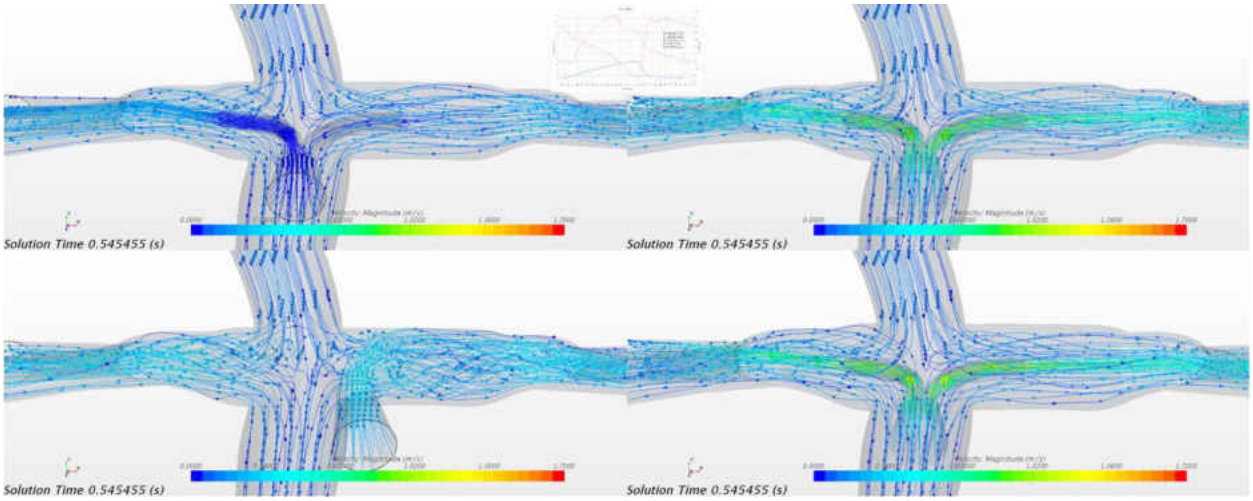

Figure 62: Synthetic Model: Velocity Streamlines at Late Diastole. Top Left: Baseline, Top Right: IJS, Bottom Left: NES, Bottom Right IJS with 10.7% Pulmonary Artery Expansion.

4.6 CHOP-1 Simulation

Three configurations for the CHOP-1 model were analyzed using multi-scale analysis. The three configurations are a baseline, an inner IJS, and an outer IJS model. The converged CFD and LPM boundary conditions for the CHOP-1 models are displayed in Figure 63 and Figure 64. LPA Velocity streamlines for peak systole, early diastole, mid diastole, and late diastole for each CHOP-1 configuration are displayed in Figure 65 to Figure 68. The RPA velocity streamlines are displayed in Figure 69 to Figure 72. Like the synthetic results, the flow shows signs of flow recirculation upstream of the nozzle caused by the rigid walls. High levels of swirl are apparent in the baseline model due to the changing direction of the LPA. The inner and outer IJS alleviate this swirl by entraining the flow parallel to the vessel wall. In the RPA, the outer IJS comes in at a low angle, but still impinges upon the opposite wall downstream, which causes recirculation that the inner IJS does not create. The WSS is plotted for peak systole, early diastole, mid diastole, and late diastole in Figure 73 to Figure 76. As expected, the outer IJS causes stress concentrations, 200[dyne/cm^2], directly across from the nozzle during peak systole. During diastole, there is no significant difference between the three configurations.

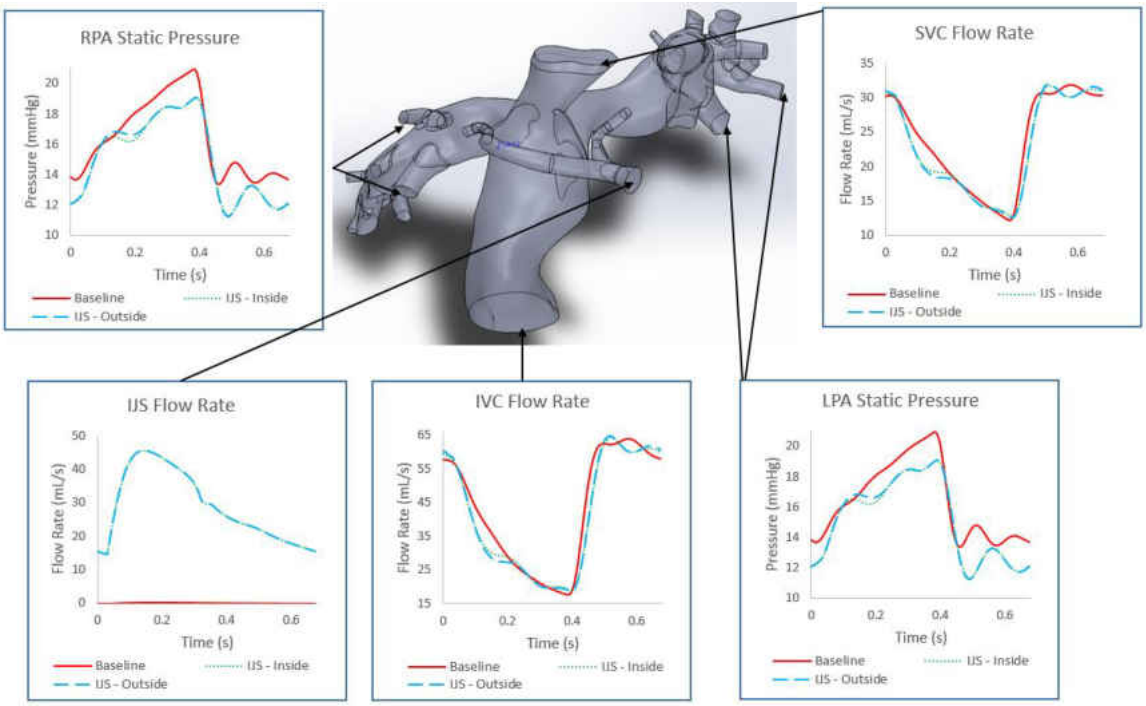

Figure 63 CHOP-1 Model: Converged CFD Boundary Conditions.

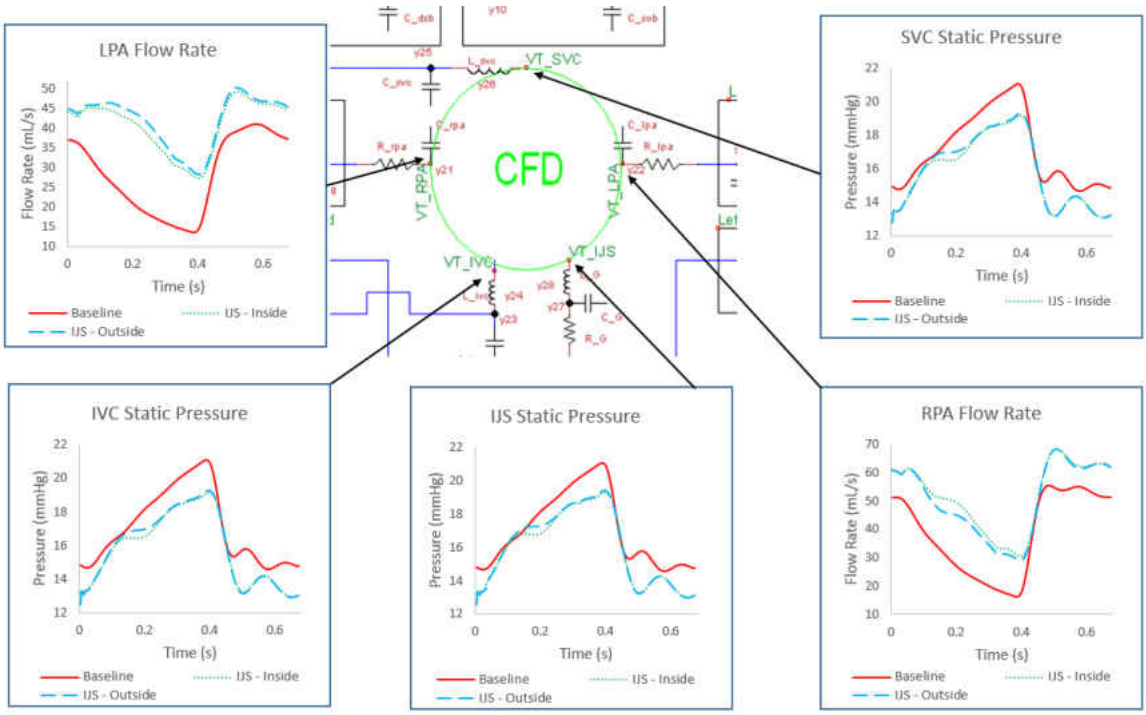

Figure 64 CHOP-1 Model: Converged LPM Boundary Conditions.

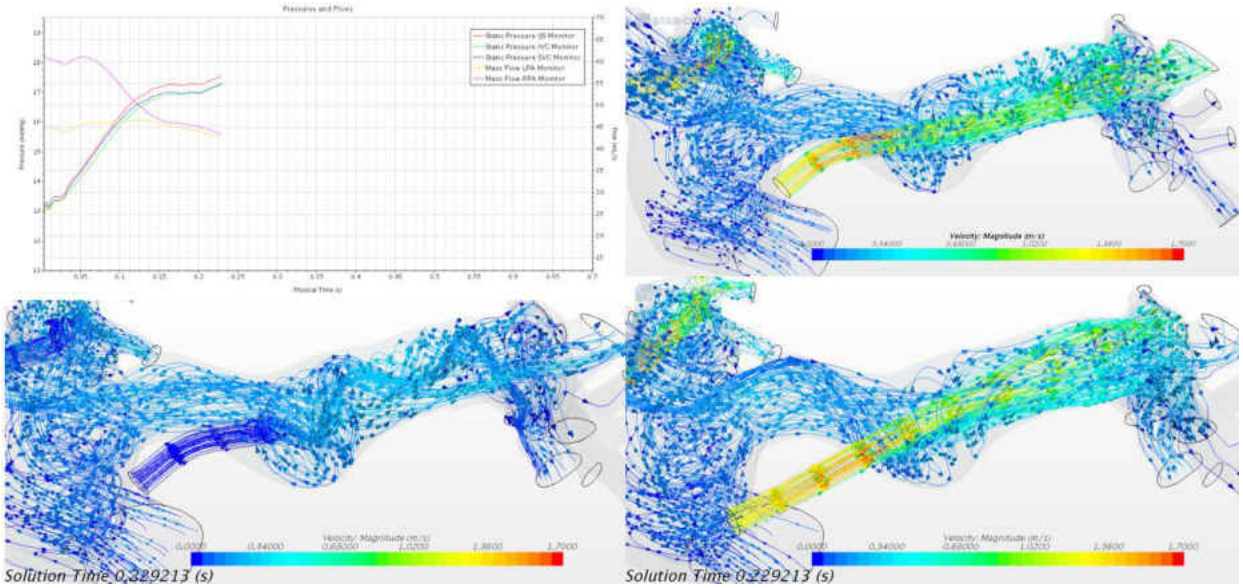

Figure 65: CHOP-1 Model: LPA Velocity Streamlines at Peak Systole. Left: Baseline, Top Right: Inner IJS, Bottom Left: Outer IJS.

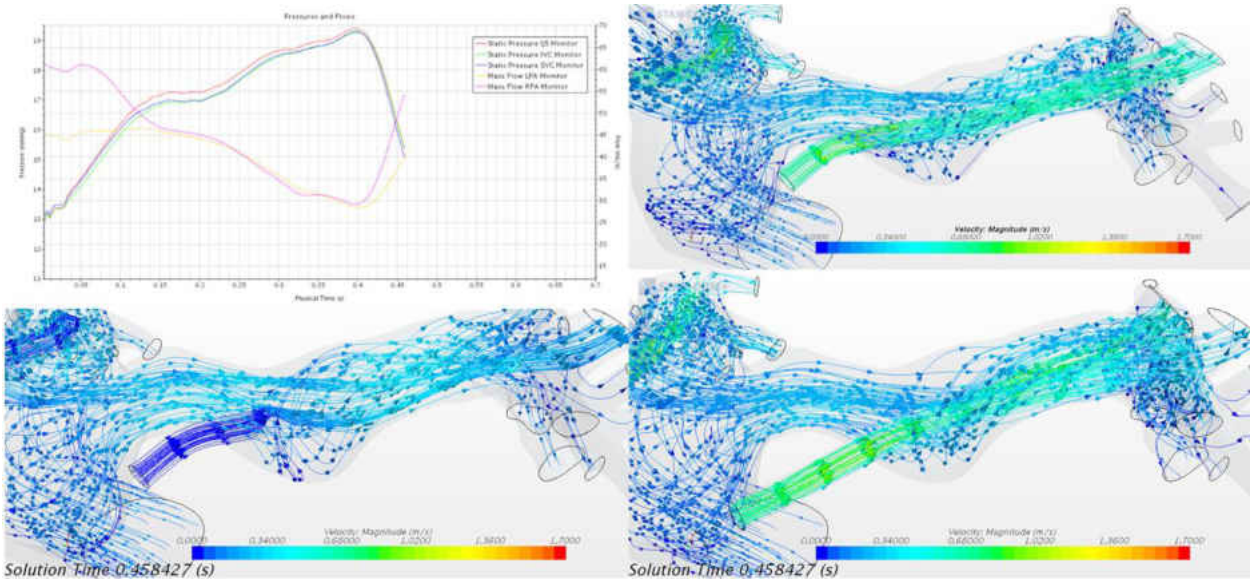

Figure 66: CHOP-1 Model: LPA Velocity Streamlines at Early Diastole. Left: Baseline, Top Right: Inner IJS, Bottom Left: Outer IJS.

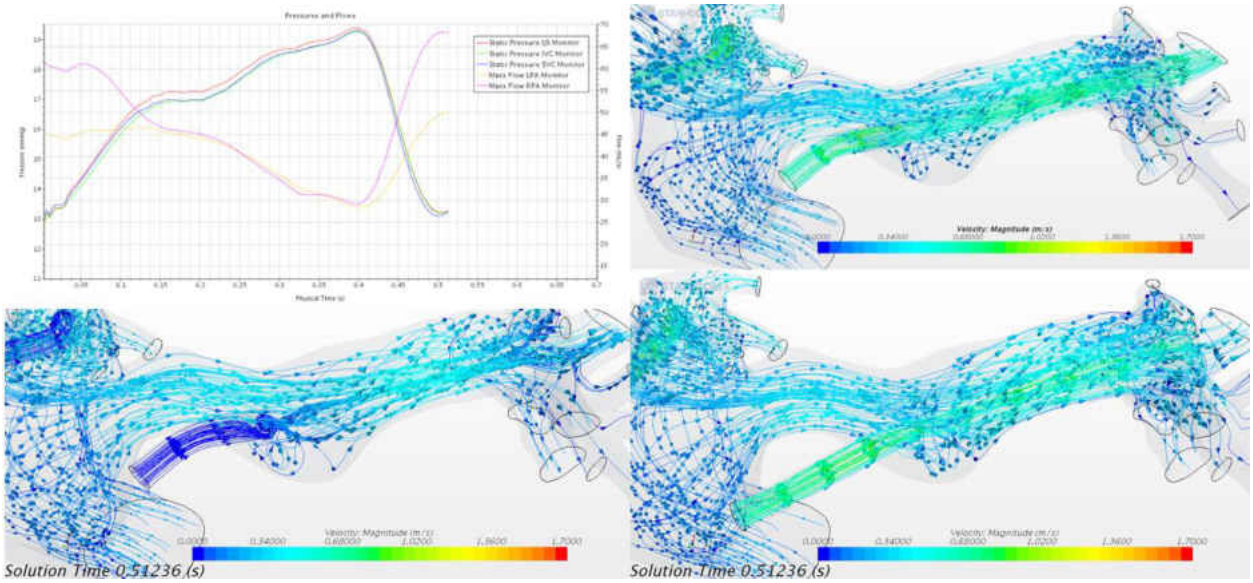

Figure 67: CHOP-1 Model: LPA Velocity Streamlines at Mid Diastole. Left: Baseline, Top Right: Inner IJS, Bottom Left: Outer IJS.

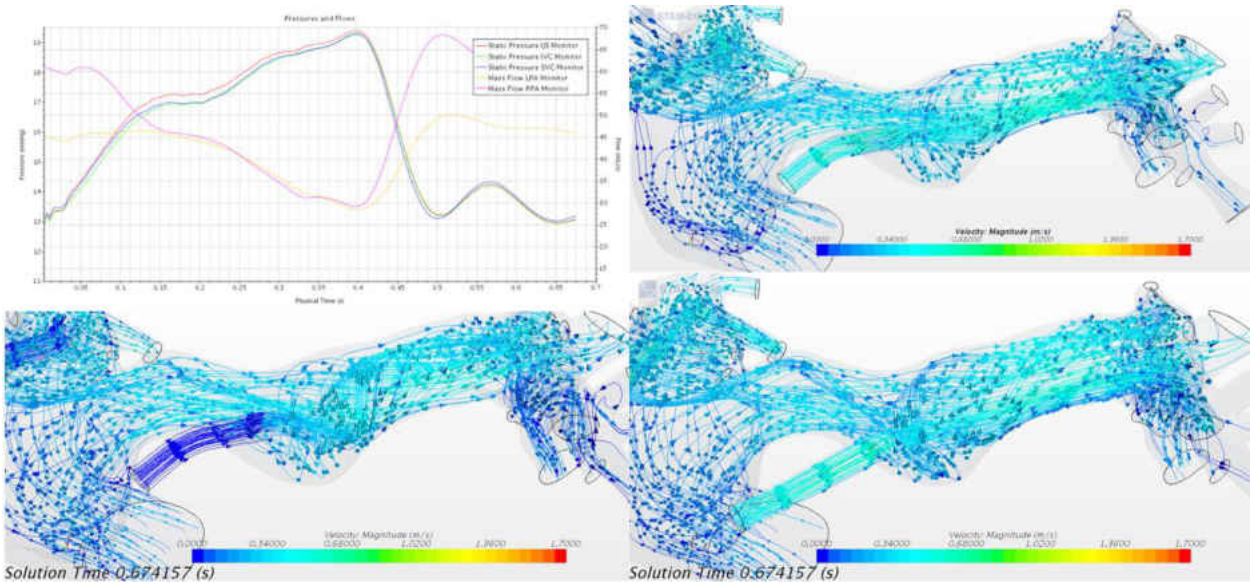

Figure 68: CHOP-1 Model: LPA Velocity Streamlines at Late Diastole. Left: Baseline, Top Right: Inner IJS, Bottom Left: Outer IJS.

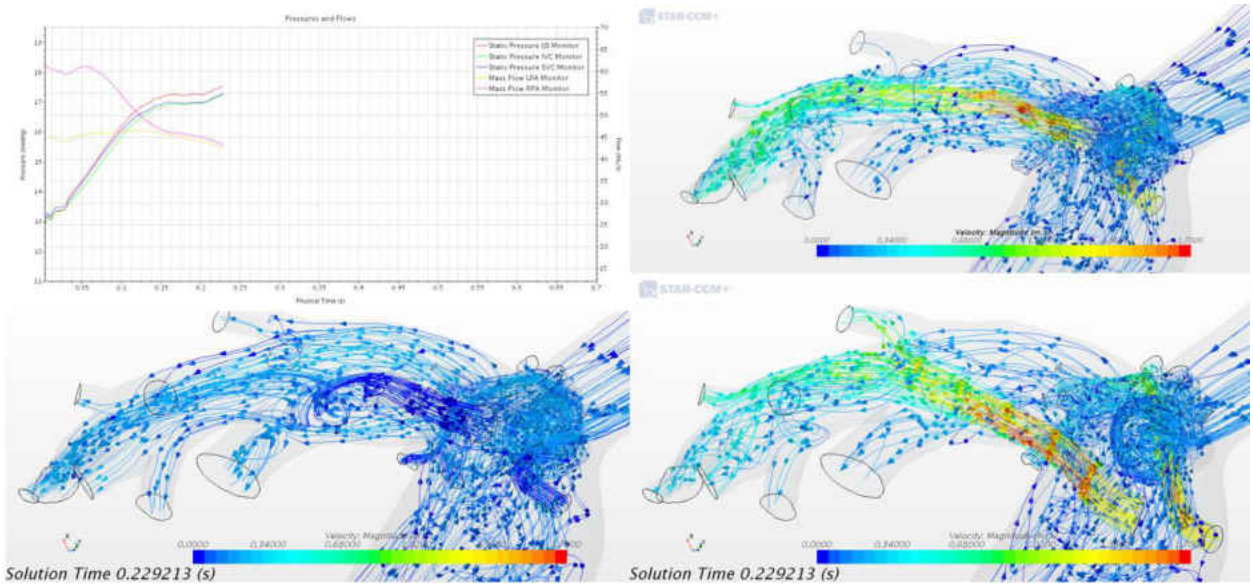

Figure 69: CHOP-1 Model: RPA Velocity Streamlines at Peak Systole. Left: Baseline, Top Right: Inner IJS, Bottom Left: Outer IJS.

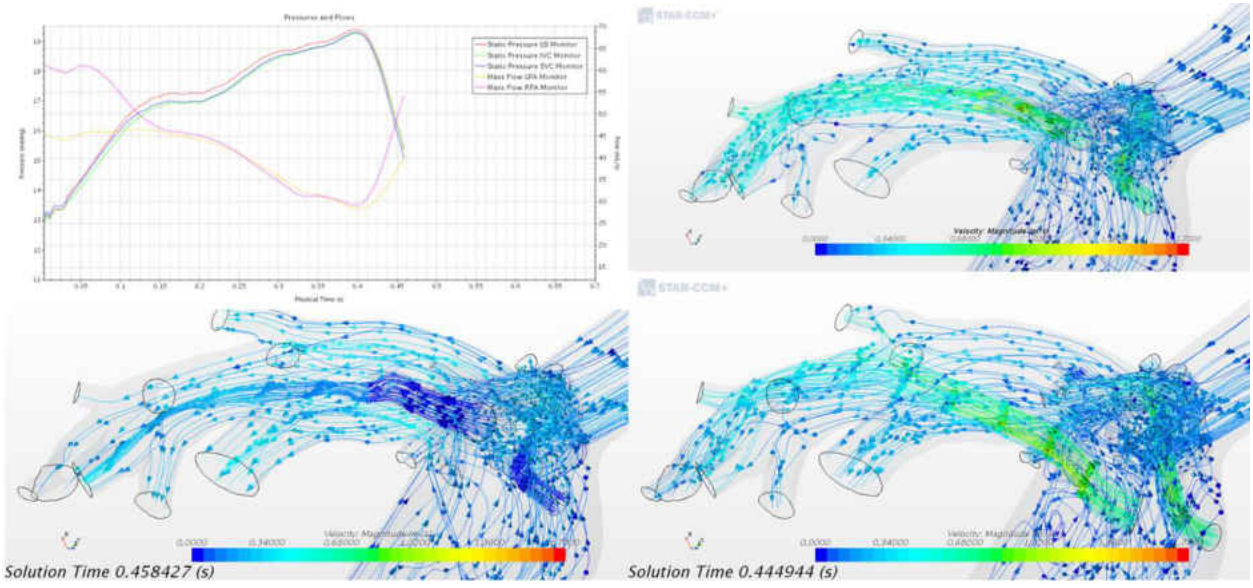

Figure 70: CHOP-1 Model: RPA Velocity Streamlines at Early Diastole. Left: Baseline, Top Right: Inner IJS, Bottom Left: Outer IJS.

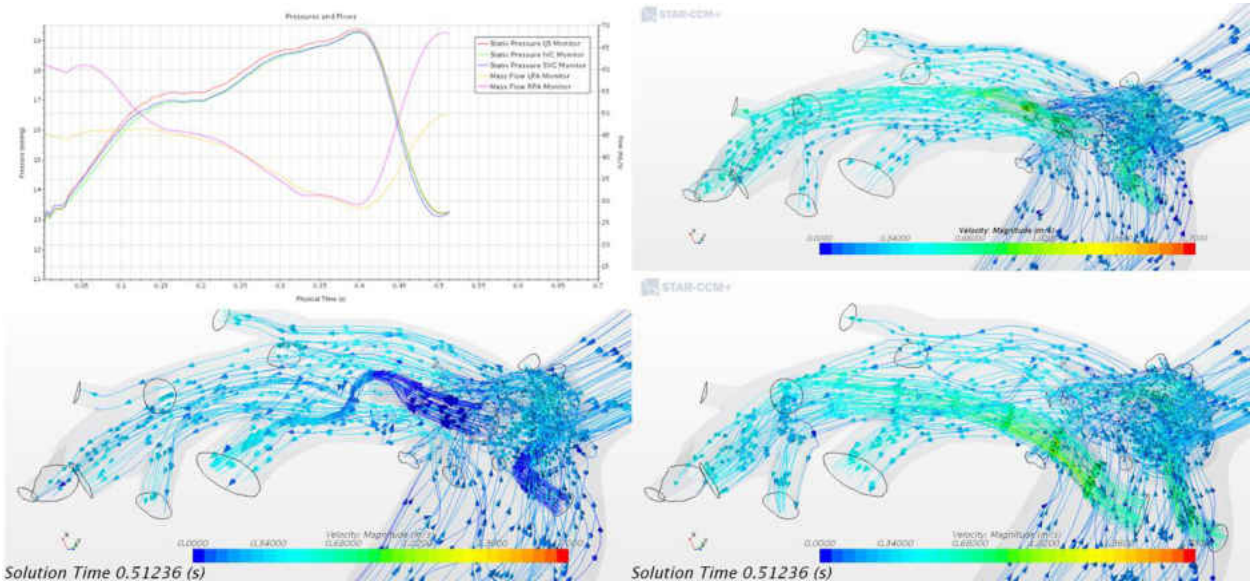

Figure 71: CHOP-1 Model: RPA Velocity Streamlines at Mid Diastole. Left: Baseline, Top Right: Inner IJS, Bottom Left: Outer IJS.

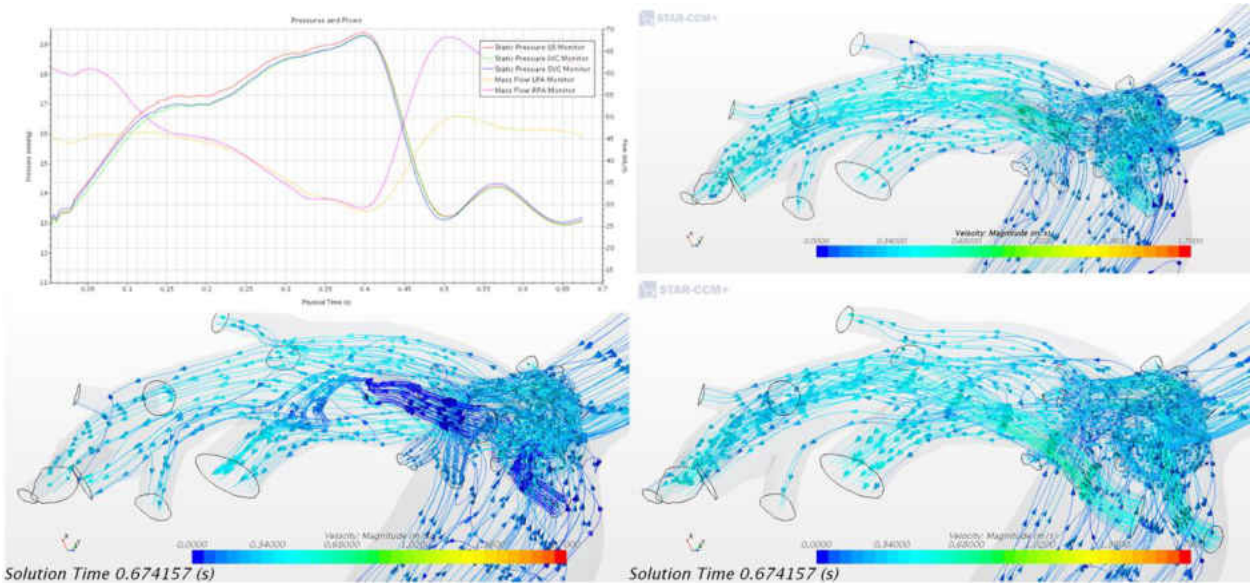

Figure 72: CHOP-1 Model: RPA Velocity Streamlines at Late Diastole. Left: Baseline, Top Right: Inner IJS, Bottom Left: Outer IJS.

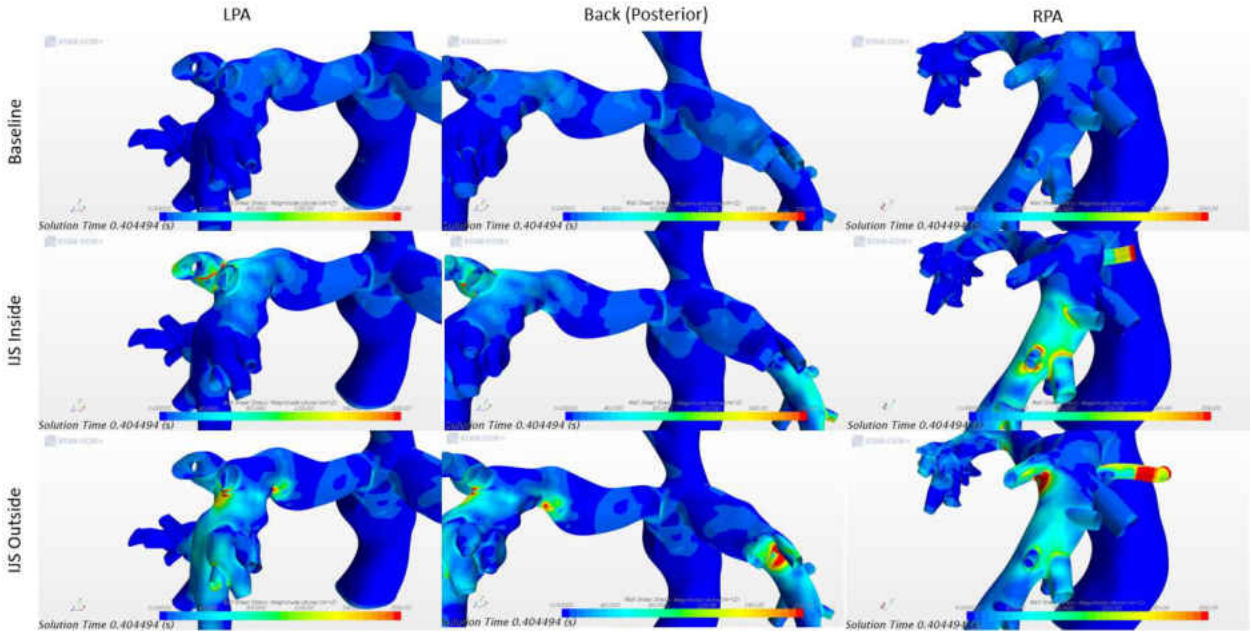

Figure 73: CHOP-1 Model: Wall Shear Stress at Peak Systole.

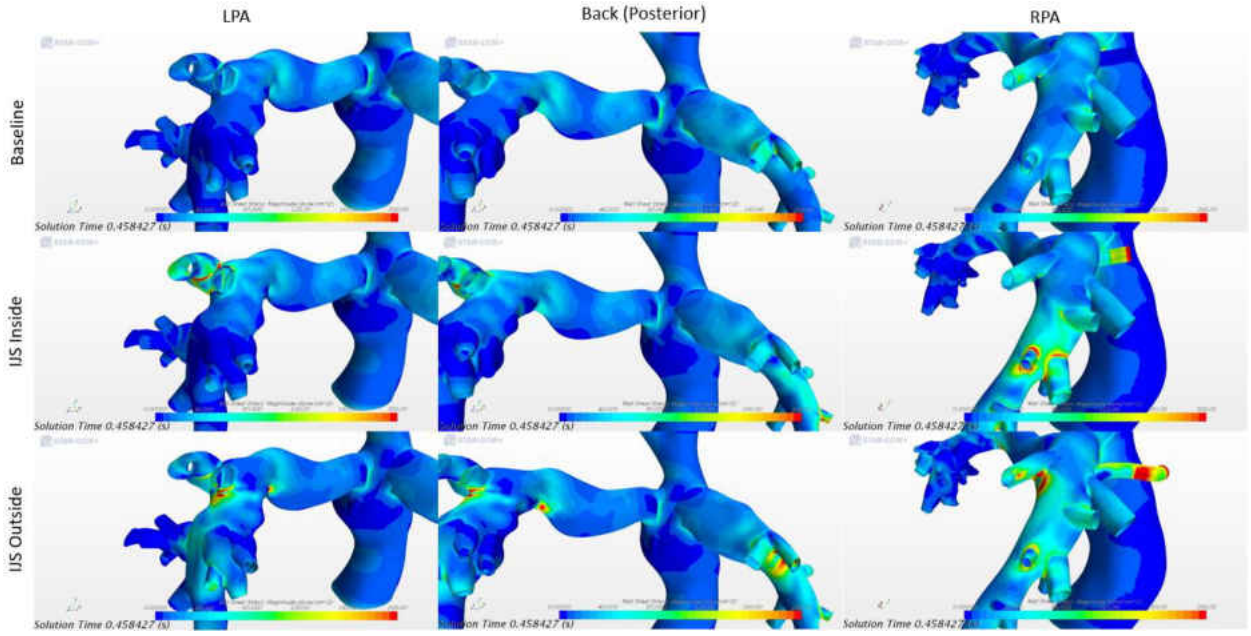

Figure 74: CHOP-1 Model: Wall Shear Stress at Early Diastole.

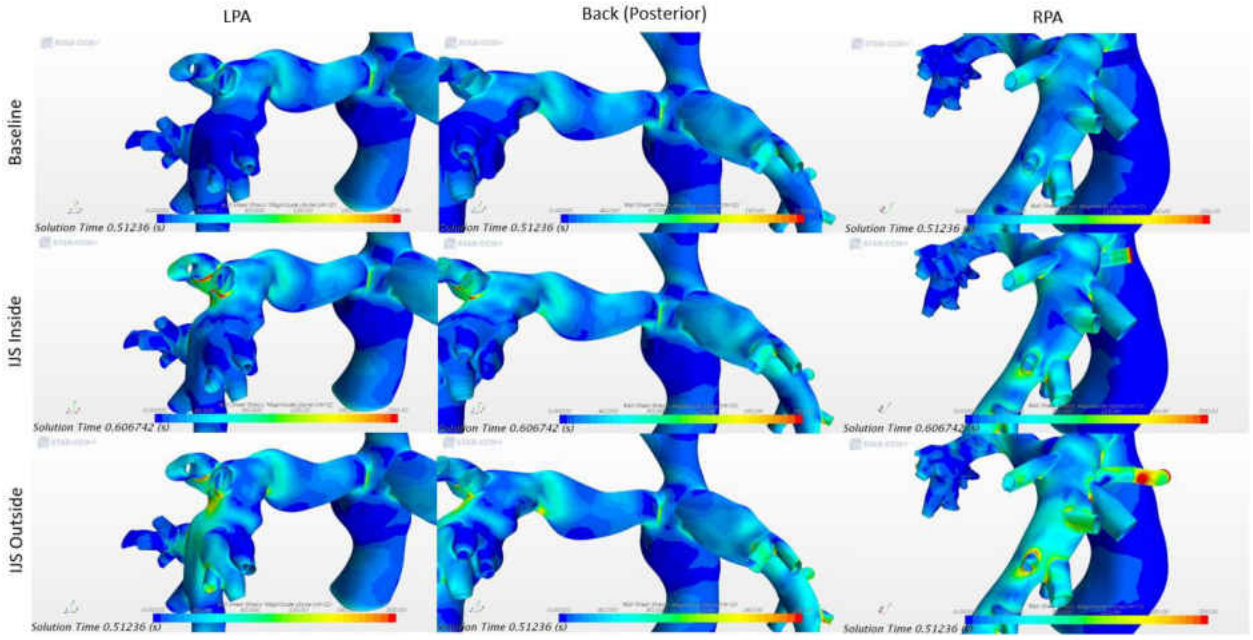

Figure 75: CHOP-1 Model: Wall Shear Stress at Mid Diastole.

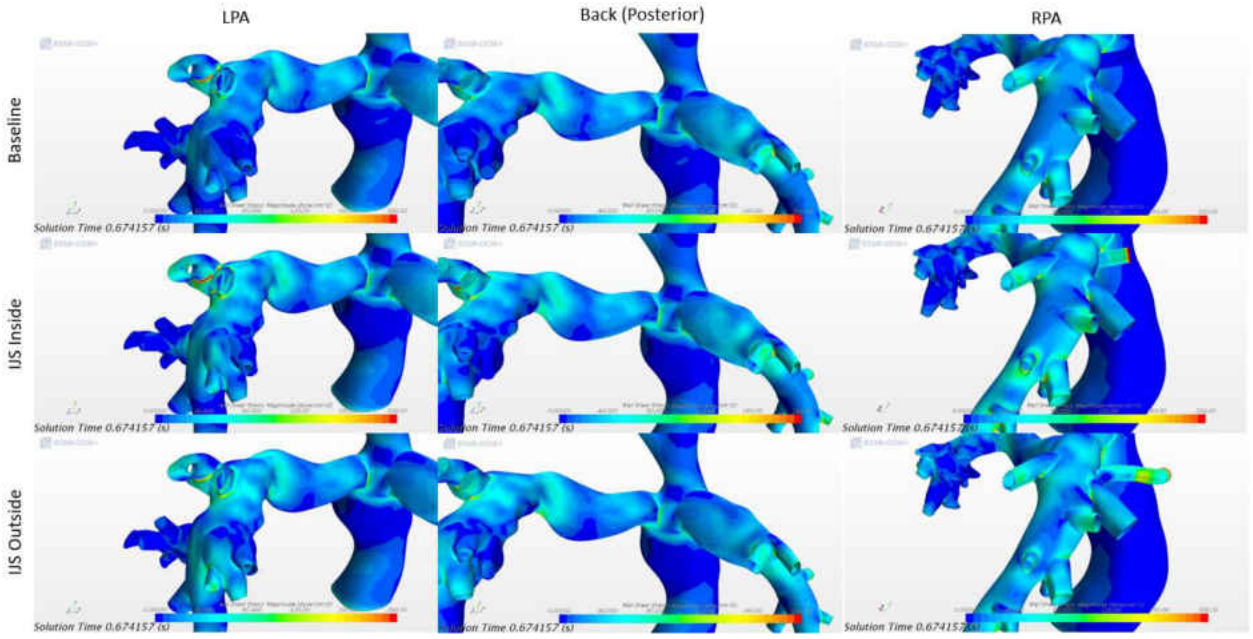

Figure 76: CHOP-1 Model: Wall Shear Stress at Late Diastole.

4.7 CHOP-6 Simulation

Two configurations for the CHOP-6 model were analyzed using multi-scale analysis. The two configurations include a baseline and IJS model. The converged CFD and LPM boundary conditions for the CHOP-6 models are displayed in Figure 77 and Figure 78. These plots show significant increases in flow and pressure pulsatility. The velocity streamlines for peak systole, early diastole, mid diastole, and late diastole are displayed in Figure 79 to Figure 82. The flow recirculation upstream of the nozzles during peak systole are elevated compared to the synthetic and CHOP-1 models, shown in Figure 79. The CHOP-6 model has similar geometrical measurements to the synthetic model, but the hemodynamics are quite different. The cardiac output is higher (1.45[L/min] to 1.21[L/min]), and the Qp/Qs converged to a slightly higher value (1.53 to 1.45). This increased IJS flow in a rigid body causes higher flow recirculation because the walls are constricting the flow field upstream.

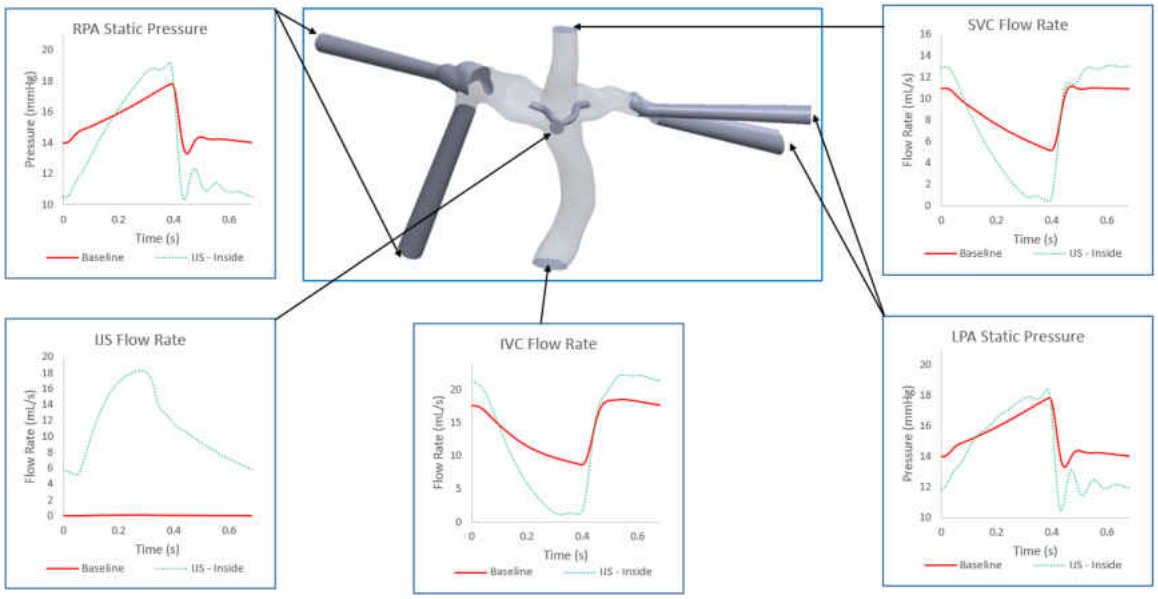

Figure 77: CHOP-6 Model: Converged CFD Boundary Conditions.

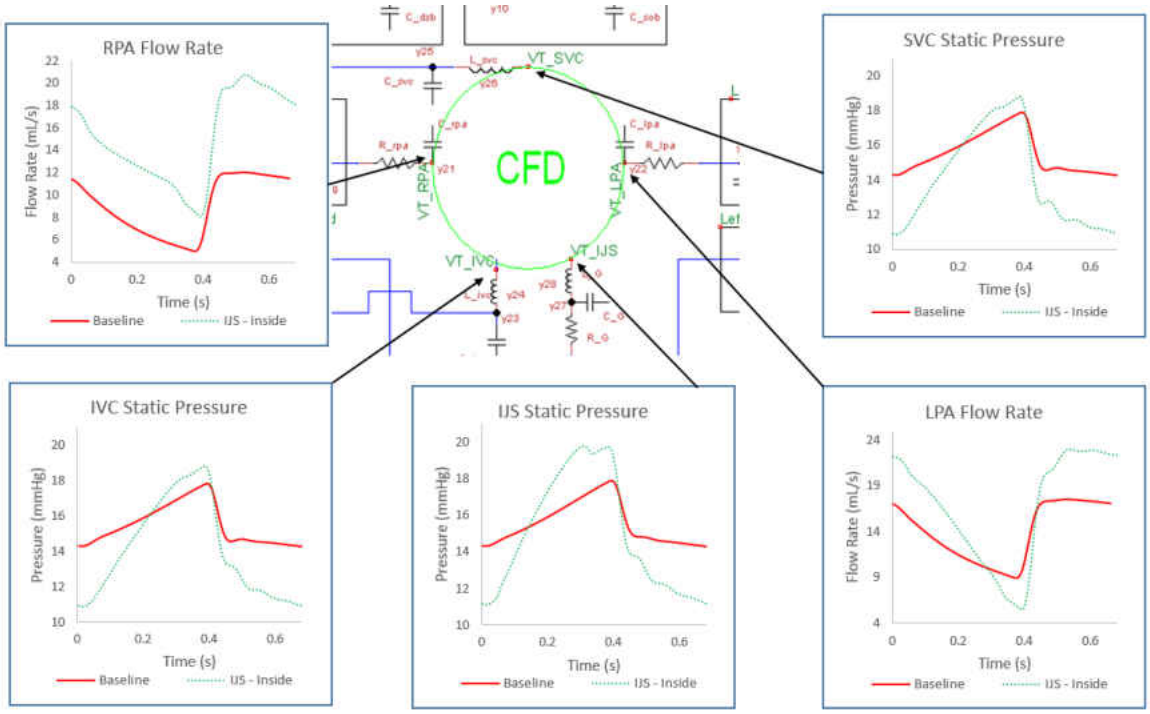

Figure 78: CHOP-6 Model: Converged LPM Boundary Conditions.

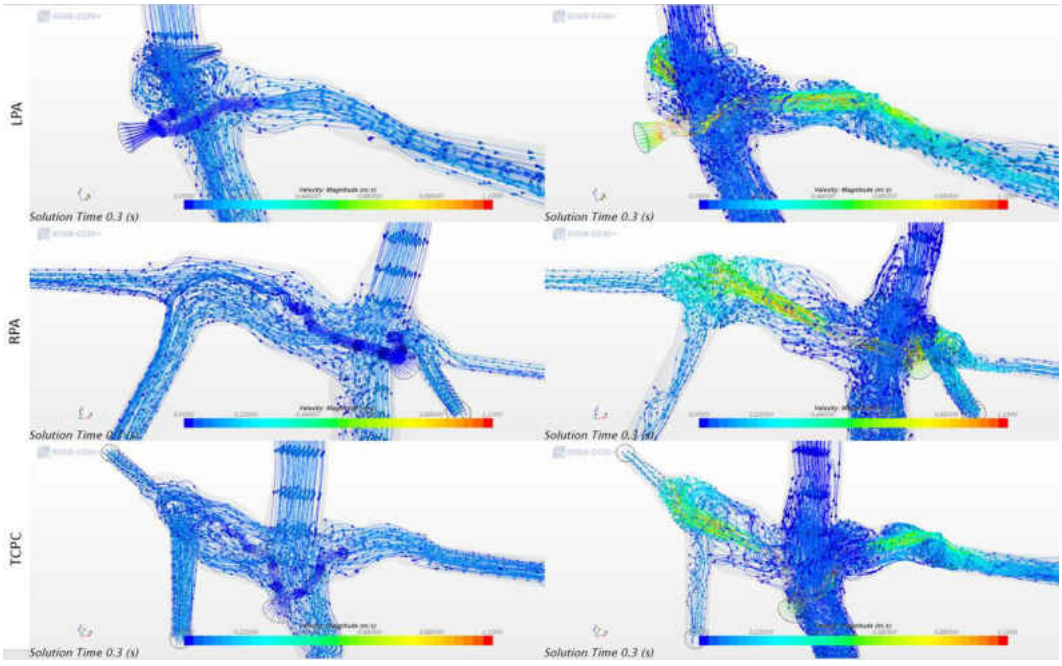

Figure 79: CHOP-6 Model: Velocity Streamlines at Peak Systole. Left: Baseline, Right: IJS.

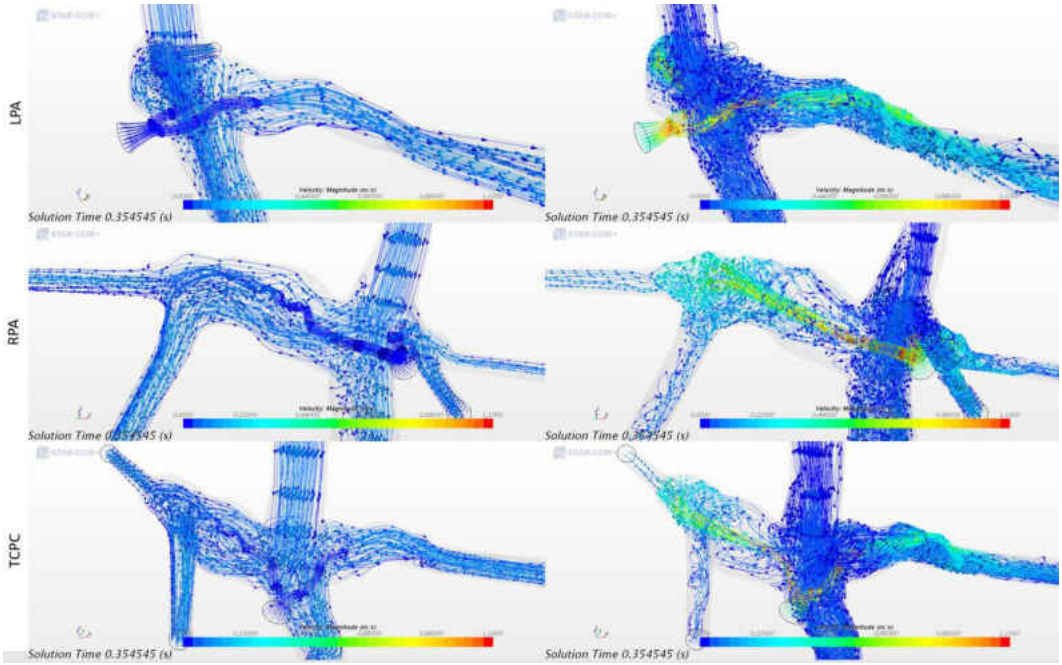

Figure 80: CHOP-6 Model: Velocity Streamlines at Early Diastole. Left: Baseline, Right: IJS.

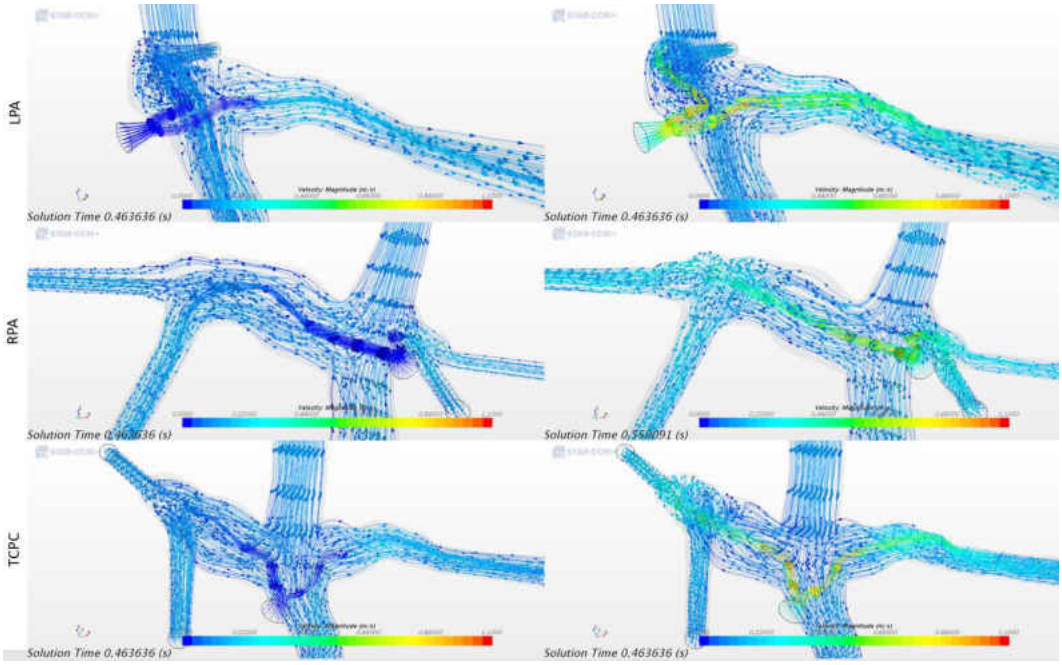

Figure 81: CHOP-6 Model: Velocity Streamlines at Mid Diastole. Left: Baseline, Right: IJS.

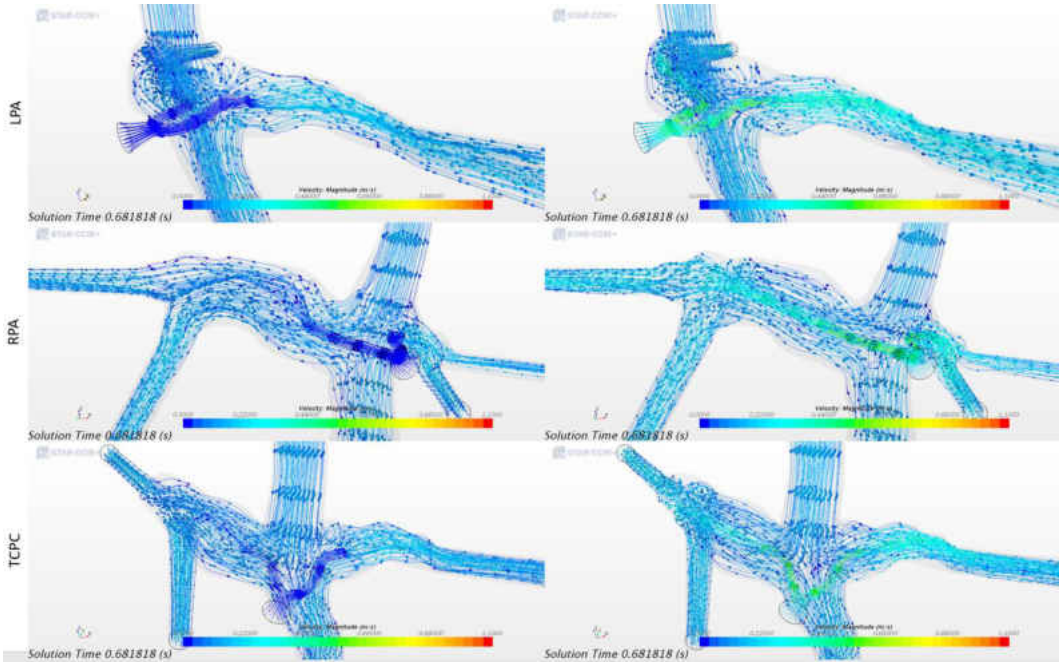

Figure 82: CHOP-6 Model: Velocity Streamlines at Late Diastole. Left: Baseline, Right: IJS.

The WSS for the CHOP-6 model is also plotted in Figure 83. The only concerning WSS concentrations appear at the RPA bifurcation where the IJS flow impinges. It is also lower at 150[dynes/cm^2], compared to the synthetic model showing 200[dynes/cm^2] in both the LPA and RPA bifurcations.

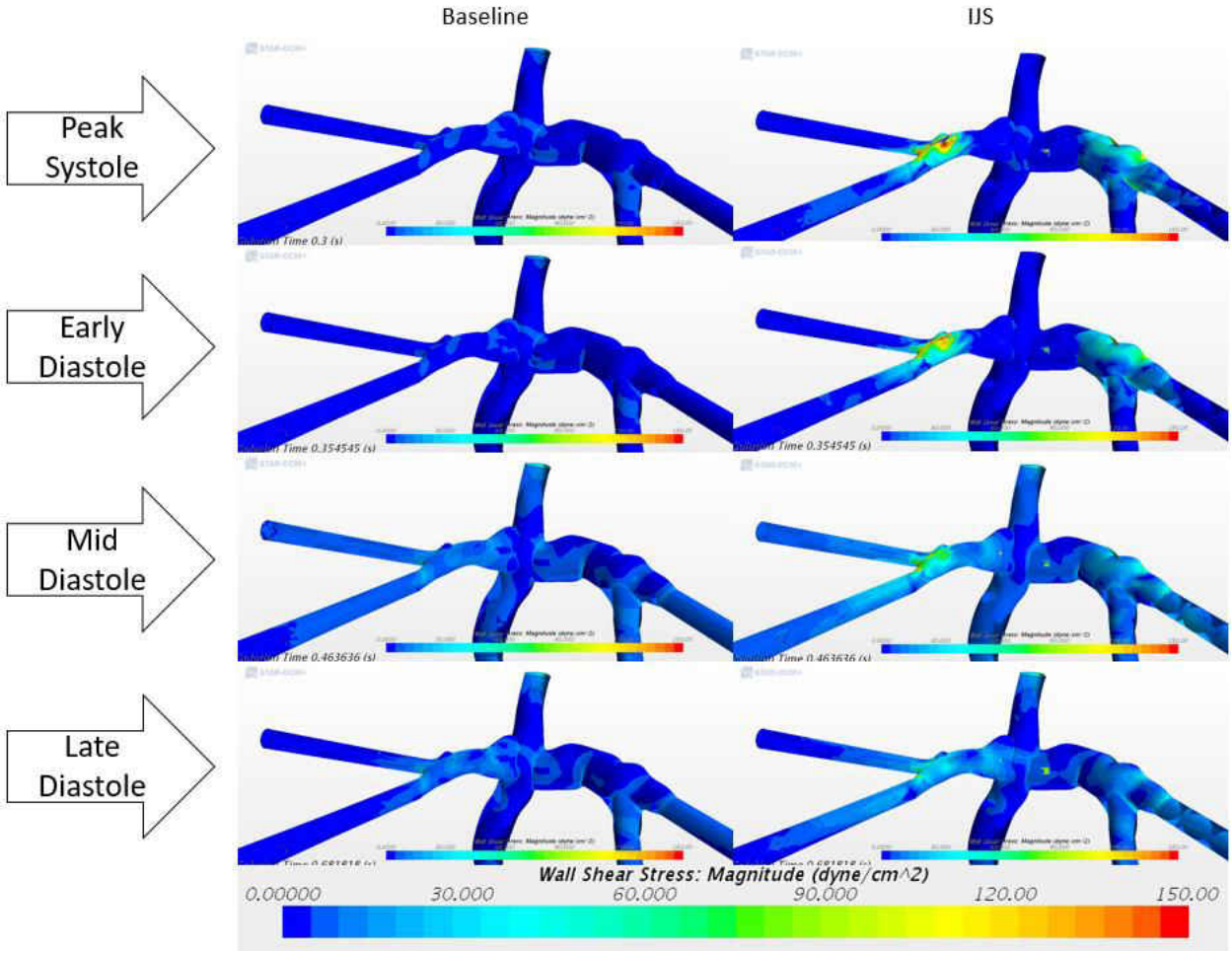

Figure 83: CHOP-6 Wall Shear Stress: Baseline vs. IJS. Left: Baseline, Right: IJS.

4.8 Comparison of Simulation Results

For the synthetic models, the IJS with PA expansion model out-performed the rest by providing the largest pressure drop in the IVC by 2.91[mmHg]. The IJS with 60% PVR reduction was also very close at 2.88[mmHg]. IVC pressure drop in the NES model was 2.52[mmHg]. This suggests that the entrainment effect from the IJS model causes a 0.36[mmHg] IVC pressure drop. Hence, the entrainment is 12.5% of the total effect while the PVR drop is the other 87.5%. This low contribution is a result of the low momentum transfer, about 18%. The PA expansion increased momentum transfer to 25%, but had a minor effect on the IVC pressure. The NES displayed virtually no momentum transfer, about 3%, which

was expected. Benefits of the IJS also include: **(1)** a 59% increase in pulmonary flow pulsatility, from 0.44 to 0.70, **(2)** a 65% increase in pressure pulsatility, from 0.31 to 0.51, **(3)** a 137% increase in pulse pressure, from 2.89[mmHg] to 6.87[mmHg], and **(4)** a 22% increase in systemic oxygen delivery, from 2.37[mL-O_2/s] to 2.88[mL-O_2/s]. The NES also provides comparable results (within 7%) with respect to pulsatility, pulse pressure, and systemic O_2delivery. Therefore, a 50% augmentation of the pulmonary flow, with no entrainment, will provide similar benefits.

The CHOP-1 model compares the inside IJS vs. the outside IJS configurations. The inner IJS configuration is slightly more efficient than the outer IJS, which is comparable to the tube entrainment study in section 4.1. Benefits of the IJS are less effective in the CHOP-1 model as compared to the synthetic and CHOP-6 models. Implementation of an IJS in the CHOP-1 model produced **(1)** an IVC pressure drop of 1.27[mmHg], **(2)** a 45% decrease in pulmonary flow pulsatility, **(3)** a 10% increase in pressure pulsatility, **(4)** a %2 increase in pulse pressure, and **(5)** a 7% decrease in systemic O_2 delivery. In this case, the pulmonary flow pulsatility and systemic O_2 delivery decreased. Causes for these differences between the synthetic and CHOP-1 models can be attributed to the model parameters. The CHOP-1 model has a larger cardiac output, larger vascular compliances, lower vascular resistances, and a slower heart rate as compared to the synthetic model. Vascular compliance is most likely the largest contributor to these differences because it effectively damps out the flow and pressure waves, resulting in loss of pulsatility. Entrainment also becomes less effective in larger tubes with lower flow resistance. The required driving pressure is lower, which results in lower entrainment rates [71]. There were also key differences in momentum transfer between the synthetic and CHOP-1 models. The momentum transfer in the synthetic model (~18%) was quite low compared to the CHOP-1 model (~50%). Even

though the momentum transfer was higher, the overall effect was lower. This is a direct result of the lower entrainment rate effect in large vessels.

The CHOP-6 model compares a baseline model with no IJS to an IJS model. The benefits of the CHOP-6 IJS are similar to the synthetic and CHOP-1 IJS models. The IVC pressure drops by 1.5[mmHg], which is slightly better than the CHOP-1 model at 1.2[mmHg]. However, it is worse than the synthetic IJS, which caused a 2.9[mmHg] IVC pressure drop. The lower IVC pressure drop is most likely due to the geometrical differences between the CHOP-6 and synthetic anatomical models. The CHOP-6 IJS shows high levels of flow recirculation upstream from the IJS nozzles, which reduces the entrainment effectiveness, displayed in Figure 79 and Figure 80. Although the CHOP-6 IJS is less effective for IVC pressure drop, the other benefits are slightly better than the synthetic IJS. **(1)** There is a 116% increase in pressure pulsatility, from 0.296 to 0.640, **(2)** a 96% increase in pulse pressure, from 4.53[mmHg] to 8.872[mmHg], and **(3)** a 15% increase in systemic O_2 delivery, from 3.253[mL-O_2/s] to 3.303[mL-O_2/s]. The results for all these multi-scale models are provided in Table 15 and Table 16.

Table 15: Multi-Scale Model Results. NES: No Entrainment Shunt, Ps: Static Pressure, CI: Cardiac Index, Qp: Pulmonary Flow, Qs: Systemic Flow, FP: Pulmonary Flow Pulsatility, PP: Pulmonary Pressure Pulsatility, PulP: Pulmonary Pulse Pressure, O2-sys: Systemic Oxygen Delivery, Ps-Drop: IVC Pressure Drop.

		mmHg	L/min/m^2		L/min			mmHg	mL O2/s	mmHg
Model	Setup	Ps IVC	CI	Qp/Qs	Qs	FP	PP	PulP	O2-sys	Ps-Drop
Synthetic (Ages 2-4)	Baseline	16.417	2.207	1.003	1.133	0.441	0.306	2.885	2.368	-
	No PVR Reduction	18.633	2.620	1.457	0.943	0.397	0.207	3.822	2.207	-2.217
	IJS - 60% PVR	13.528	3.151	1.450	1.147	0.602	0.485	6.454	2.917	2.888
	NES - 60% PVR	13.895	3.204	1.529	1.108	0.650	0.517	6.907	2.840	2.521
	IJS - 10.7% PA Expansion	13.510	3.218	1.518	1.121	0.700	0.510	6.865	2.878	2.907
CHOP1 (24yr)	Baseline	17.089	1.861	0.999	3.972	0.984	0.464	7.588	12.359	-
	60% PVR - Inside IJS	15.816	2.636	1.456	3.803	0.540	0.511	7.724	12.270	1.273
	60% PVR - Outside IJS	15.898	2.637	1.456	3.802	0.519	0.466	7.626	12.268	1.191
CHOP6 (10yr)	Baseline	15.556	1.414	1.001	1.385	0.774	0.296	4.530	3.253	-
	60% PVR Reduction IJS	14.091	1.902	1.539	1.238	0.640	0.640	8.872	3.303	1.464

Table 16: Multi-Scale Model Results Continued. NES: No Entrainment Shunt, E: Energy, MR: Momentum Ratio, MG: Momentum Gained.

		mL/s	mL/s	mL/s	mL/s	mL/s	-	-	-	kg-cm/s^2
Model	Setup	Flow RPA	Flow LPA	Flow SVC	Flow IVC	Flow IJS	Eout/Ein	LPA MR	RPA MR	MG
Synthetic (Ages 2-4)	Baseline	9.469	9.455	7.294	11.583	0.062	-	-	-	-
	No PVR Reduction	11.458	11.455	6.087	9.636	7.190	0.884	0.177	0.177	6.842
	IJS - 60% PVR	13.873	13.844	7.392	11.717	8.626	0.807	0.18	0.181	10.028
	NES - 60% PVR	14.244	14.002	7.138	11.336	9.795	0.958	0.035	0.037	4.476
	10.7% PA Expansion	14.250	14.118	7.228	11.463	9.699	0.957	0.266	0.247	9.398
CHOP1 (24yr)	Baseline	38.180	27.991	23.688	42.518	0.074	-	-	-	-
	60% PVR - Inside IJS	51.727	40.526	22.719	40.657	28.942	0.947	0.322	0.834	40.565
	60% PVR - Outside IJS	50.208	42.066	22.723	40.642	28.989	0.945	0.353	0.773	44.559
CHOP6 (10yr)	Baseline	9.094	14.014	8.868	14.215	0.053	-	-	-	-
	60% PVR Reduction IJS	15.115	16.650	7.873	12.762	11.172	0.975	0.277	0.217	11.053

CHAPTER 5: CONCLUSIONS, LIMITATIONS, AND FUTURE WORK

5.1 Conclusions and Limitations

A steady state optimization tool was developed and used to quickly carry out several CFD simulations of different IJS configurations. These simulations calculated the optimal IJS nozzle diameter (3[mm]), IJS nozzle distance to TCPC (15[mm]), and area ratio between the pulmonary artery and the nozzle (16). An automated 0D-3D tightly coupled multi-scale model was also developed to simulate the hemodynamic effects of the Fontan circulation. Synthetic and patient specific models were fitted with various optimized IJS configurations. With this "virtual" IJS implementation, the pressure in the IVC dropped by 1-3[mmHg]. This drop resulted from the combination of IJS entrainment and PVR reduction due to increased pulmonary flow. The goal was a 5[mmHg] drop, but the limitations on patient physiology seemed to make this unattainable. Limitations include: **(1)** heart function is limited to a Qp/Qs of 1.5, **(2)** the nozzle to pulmonary area ratio cannot be safely increased above 20 (nozzle diameter will be too small, which can cause thrombus and too much resistance for the ventricle), **(3)** the pulmonary arteries are collapsible at high transmural pressures, **(4**) PVR vs. flow relations are not well known, **(5)** the human body has a finite reservoir, and **(6)** there is no suction chamber for the IJS to be placed. It was also observed that the CHOP-1 model displayed significantly lower IVC pressure drops than that of the synthetic and CHOP-6 models. The IJS becomes less effective in larger Fontan models with lower resistance. With low resistance models, the required driving pressure is lower which results in lower entrainment rates [71].

The benefits of the IJS include: **(1)** increased pulmonary pulse pressure, **(2)** increased pulmonary flow, **(3)** PVR reduction, **(4)** minimal stress concentrations, **(5)** increased systemic oxygen delivery, **(6)** decrease in IVC pressure, and **(7)** TCPC recirculation reduction. The increased pulmonary pulse pressure

and pulmonary flow can help develop the pulmonary vascular system [26][27][28][59], which is one of the leading causes of Fontan circulation failure. The inner IJS had an insufficient advantage over the outer IJS (less than 7% in the CHOP-1 model). Inner IJS implementations may be too extreme in clinical applications to overcome this 7% increase in efficiency. These benefits are subject to the multi-scale model limitations which did not account for **(1)** distensible vessel walls, **(2)** respiratory effects, **(3)** patient growth, **(4)** patient exercise, or **(5)** traumatic effects of clinical applications. From these cases, the major limitation is the rigid walls used for the CFD model. When attempting to entrain the flow to decrease IVC pressure, 50% more flow is introduced into the pulmonary arteries. This increase in mass flow requires an adjustment to account for this extra mass, or the pressure upstream will only increase (if the flow increases, and the resistance remains constant, the required driving pressure also increases, equation 3.2.7). The pulmonary vascular system will allow more flow by vasodilating the vasculature, but this happens downstream from the nozzle outside of the 3D domain. A local component to adjust for increased mass flow is required to maximize the entrainment effect. A dynamic expansion of the pulmonary artery walls will allow for flow augmentation which will, in theory, increase the entrainment rate.

The other major limiting factor is that the PVR vs. pulmonary flow model is modest. Ideally, the PVR would change dynamically with increased or decreased pulmonary flow. This PVR change would account for the augmenting pulmonary flow from the IJS. Since this relationship is not well known, the PVR was simply reduced based on average patient data. This simple reduction does not account for all the extra pulmonary flow being introduced to the pulmonary system. In a clinical situation, it is more likely that the PVR will actually decrease further due to the benefits the pulmonary system receives from increased pulsatility and pulse pressure [26][27][28][38]. In fact, there was a recent case study showing

a PVR drop over 70% just by mechanically assisting the pulmonary system [73]. Another issue is that the PVR model was created using data from patients with healthy PVR levels. Since PVR changes curvilinearly with increased flow [29], the PVR drop would be less in healthy patients, compared to patients with elevated PVR. Hypothetically, patients with elevated PVR would see higher PVR drops with the same increase of pulmonary flow, pulse pressure, and pulsatility (these effects will open the previously closed capillary beds in a sick pulmonary system).

5.2 Future Work

This proof of concept will help lead the way to more complex models. These models should include fluid structure interaction (FSI), respiratory effects, exercise effects, and a robust pulmonary vascular bed model. FSI will take the distensibility of the vessel walls into consideration, which will affect the momentum transfer due to higher volumetric flows. During normal Fontan operating conditions, the conduit sees small changes in vessel wall displacement. This could change dramatically with the introduction of an IJS. For respiratory effects, the lung resistance increases and decreases based on the respiratory cycle, which is slower than the heart cycle (1 respiratory cycle = 2-3 heart cycles). IJS implementation may be directly affected by lung capacity and respiratory rate. Exercise in a Fontan circulation decreases PVR and increases systemic flow rate. Implementation of an IJS will increase oxygen transport to the systemic system, which should lead to increased exercise capacity. Further studies are needed to validate this hypothesis. Pure PVR vs. flow models in healthy and Fontan patients are not available. Most models include other factors such as oxygen inhalation, exercise, and dobutamine administration. Once more patient data is available, a more accurate and robust PVR vs. flow model should be included in future simulations. Validation of this computational model is also being carried out in vitro by Das et al [75].

5.3 List of Current Publications

Journal:

- Marcus Ni, Ray Prather, Nicholas Voce, Alain Kassab, Eduardo Divo, and William DeCampli. Computational Investigation of a Self-Powered Fontan Circulation. *Computer Methods in Biomechanics and Biomedical Engineering. (in preparation)*
- Marcus Ni, Alain Kassab, and Eduardo Divo. Automated hybrid singularity superposition and anchored grid pattern BEM algorithm for the solution of inverse geometric problems. *Engineering Analysis with Boundary Elements* vol. 73, pp 69-78, Dec 2016.
- Ray Prather, Marcus Ni, Alain Kassab, Eduardo Divo, et al. Multi-Scale Pulsatile CFD Modeling of Thrombus Transport in a Patient-Specific LVAD Implantation. *International Journal of Numerical Methods for Heat and Fluid Flow*. (accepted for publication November 2016, to appear on-line April 2017 in Vol. 27, No. 5.)

Conference:

- Arka Das, Anthony M. Khoury, Jake Tibbets, Marcus Ni, Eduardo Divo, Alain Kassab, and William DeCampli. Laboratory Development of a Self-Powered Fontan for Treatment of Congenital Heart Disease. *Proceedings of the 2nd Thermal and Fluid Engineering Conference, TFEC2017. 4th International Workshop on Heat Transfer, IWHT2017*. April 2-5, 2017, Las Vegas, NV, USA.
- Marcus Ni, Eduardo Divo, Alain Kassab, William Decampli, et al. A tightly coupled multi-scale CFD analysis of the Fontan circulation. *VI International Conference on Computational Methods for Coupled Problems in Science and Engineering – Coupled Problems* 2015, Venice Italy.

- Stephen Guimond, Marcus Ni, Nicholas Voce, Alain Kassab, et al. Computational Fluid Dynamics Simulation of United Launch Alliance Delta IV Hydrogen Plume Mitigation Strategies. *AIAA Paper number AIAA-2015-0840. presented at the 53rd AIAA Aerospace Sciences Meeting, AIAA Science and Technology Forum*, Kissimmee Florida, 5-9 Jan, 2015.
- Marcus Ni, Alain Kassab, and Eduardo Divo. Automated hybrid singularity superposition and anchored grid pattern BEM algorithm for the solution of the inverse geometric problem. *International Conference on Inverse Problems in Science and Engineering*, Krakow Poland 2014.
- Priscilla Elfrey, G. Zacharewicz, and Marcus Ni. Smackdown: adventures in simulation standards and interoperability. *WSC '11 Proceedings of the Winter Simulation Conference*, pp 3963-3967, 2011.

APPENDIX A:
MULTISCALE MODEL PROGRAM INSTRUCTIONS

Setting up the StarCCM Model for Tightly Coupled Scheme

If the number of boundary conditions need to be changed, or the types of boundary conditions need to be changed, then the LPM program needs to be updated. The program should be updated by searching for the keyword “USER TODO”. This keyword will direct you to the sections of the RK code that must be updated for significant changes to the circulation.

To begin, The CFD model needs to be setup with the appropriate parameters (mesh, boundary conditions, solver parameters, etc.). The CFD initialization is a three-step process:

1) Initialize the flow field with simple initial conditions for pressure (like 14[mmHg] for the Fontan circulation).
2) Run the CFD with a 10 second time step using the table/time boundary conditions. This is a transient study, but the BC values should remain constant at t=0 for t=0 to t=10 seconds. This will help the actual transient study start off with a good initial guess for the flow field at t=0.
3) Clear the time history, then run at least 2 complete cycles using the closed loop LPM BCs with proper time steps (always clear the time history when starting a new cycle).

CFD outputs: The multi-scale model requires the CFD to output two different files:

1) CFDout.csv : These are the boundary conditions being passed to the LPM at each time step.
2) CFDoutIter.csv : These are the same BCs as CFDout, except it is recording at every iteration rather than every time step.

LPM inputs: The multi-scale model also requires 3 files to start the iterative process between the LPM and CFD.

1) Fontan_prev.csv : This is the closed loop LPM solution for the CFD input. Last row of this data should be labeled as END, and should contain all zeros with no comma after the zeros.
2) last_state.csv : Apply the initial conditions here.
3) Tight_BC_Transfer.csv : Closed loop solution for the LPM input. This is what the LPM is referencing when it is looking at the previous cycle's solution. It is also used for under-relaxing the CFD data being passed to the LPM.

Some files need to be manipulated:

1) Path_to_LPM : Needs to be updated to reflect the proper path to the LPM program. It is located in the folder containing the C++ Unix based RK solver.
2) user_defined_funcs.cpp : The parameter, "d_percentage", is used to control the under-relaxation. Zero would be full relaxation, while one would be no relaxation. It is recommended to start between 0.05 and 0.1, then slowly increase to about 0.5. By this point the model should be converged.
3) Java macro file : Update the paths, update the solver parameters, and update the StarCCM+ file name under the function "SaveSim()".

Continuing the solution from a previous cycle: As an example, if you would like to start from cycle 4, the procedure would be (it should be noted that when replacing these files, they need to keep the name of the file they are replacing. Example: delete "last_bc.csv" and rename "last_bc_3.csv" to "last_bc.csv") :

1) Replace "last_bc.csv" with "last_bc_3.csv".
2) Replace "last_state.csv" with "last_state_3.csv".
3) Replace "Tight_BC_Transfer.csv" with "Tight_BC_Cycle_4.csv".
4) Replace "Fontan_prev.csv" with "Fontan_3.csv".

5) Change the Java macro to start from cycle 4.

6) Change the starting sim file to cycle 3.

Noise Canceling Scheme

Complete details of the noise canceling scheme from section 3.4.3 is presented:

1) Read in data from the CFD or LPM.

2) Create a value for t=0, it should be equal to the last value of the previous cycle.

3) Calculate the average Δx_i for each boundary where $\Delta x_i = x_i - x_{i+1}$.

4) Calculate the SPD (equation 3.5.12) for all interior points of the cycle.

5) If there is a SPD value that is above the specified accepted range, check the next points SPD value until there are two consecutive SPD values that are acceptable. The "bad" SPD values should be replaced by quadratically interpolating between the nearest "good" points.

The SPD range for the Fontan boundary conditions are as follows:

1) Flow boundary conditions:
    a. 0.25 < t < 0.45: SPD < 10.
    b. Else: SPD < 4.
2) Pressure boundary conditions:
    a. 0.25 < t < 0.45: SPD < 15.
    b. Else: SPD < 5.

Importing from VTP to StarCCM+ or STL

1) Open the VTP file using a paraview program. I used Salome – www.salome-platform.org .When using Salome, use the paravis section to import the VTP file, then export to VRML.
2) Import the VRML file into 3-MATIC and make sure to scale the model properly with the correct units. Then export to STL.
3) Import STL file into StarCCM+. Make sure to check the scaling units again.

Conversions

$$P_{dynamic}\left[Pa\right] = 529.9996e^{-12}\frac{\dot{V}\left[mL/s\right]^2}{A[m^2]^2}$$ A = Area, V = Volumetric flow rate, ρ=1060 kg/m^3

$$P_{dynamic}\left[mmHg\right] = 3.975326e^{-12}\frac{\dot{V}\left[mL/s\right]^2}{A[m^2]^2}$$ A = Area, V = Volumetric flow rate, ρ=1060 kg/m^3

$$943.396\left[mL/s\right] = 1.0\left[kg/s\right]$$

$$16.666667\left[mL/s\right] = 1.0\left[L/\min\right]$$

$$1.0\left[mL-mmHg/s\right] = 133.322368\left[mW\right]$$

APPENDIX B:
WORKING ON THE UNIX CLUSTER

Calling an Executable on UNIX:

As an example, the program to be called is named “RK_Fontan”. You can run this program with the command “./RK_Fontan”. This requires you to be calling the function from the directory in which it is located. The “ . “ represents the current directory. It is also possible to call it from any location if the complete path is known, “/path-to-file/RK_Fontan”.

Useful UNIX Commands:

cd	Change directory
cd ..	Previous directory
ls	List contents of folder
qsub	Submit batch file job
qstat	Check batch jobs that are running
qdel	Delete batch job
qhost	Check the node usage
licenses	Check available licenses

Useful EMACS Commands:

C-h t	Internal tutorial
C-x C-f	Find file
C-x C-x	Quit and save everything
M-x compile	Compile code
M-x gdb	C++ compiler
C-g	Abort operation
C-h r	EMACS manual
C-x Ret f undecided-unix	Convert DOS file to UNIX file

APPENDIX C:
LPM CIRCUIT DIAGRAMS AND EQUATIONS

Full Fontan Circuit

ODEs

$$\dot{y}_0 = \frac{1}{c_{ra}}\left(I_{in} - \frac{y_0 - y_1}{R_{tric}} Hev \right)$$

$$\dot{y}_1 = \frac{1}{c_{rv(t)}}\left(\frac{y_0 - y_1}{R_{tric}} Hev - y_1 \frac{dc_{rv(t)}}{dt} - \frac{y_1 - y_2}{R_{pv}} Hev \right)$$

$$\dot{y}_2 = \frac{1}{c_{ao}}\left(\frac{y_1 - y_2}{R_{pv}} Hev - \frac{y_2 - y_{27}}{R_G} - y_3 \right)$$

$$\dot{y}_3 = \frac{1}{L_{ao}}\left(y_2 - y_3 R_{ao} - V1(y) \right)$$

$$\dot{y}_4 = \frac{1}{c_{lbab}}\left(\frac{V1(y) - y_4}{R_{da}} - y_5 \right)$$

$$\dot{y}_5 = \frac{1}{L_{lbab}}\left(y_4 - y_5 R_{lbab} - y_6 \right)$$

$$\dot{y}_6 = \frac{1}{c_{lbvb}}\left(y_5 - \frac{y_6 - y_{23}}{R_{lbvb}} \right)$$

$$\dot{y}_7 = \frac{1}{c_{corab}}\left(\frac{V1(y) - y_7}{R_{cora}} - \frac{y_7 - y_8}{R_{corab}} \right)$$

$$\dot{y}_8 = \frac{1}{c_{corvb}}\left(\frac{y_7 - y_8}{R_{corab}} - \frac{y_8 - y_0}{R_{corvb}(t)} \right)$$

$$\dot{y}_9 = \frac{1}{c_{sob}}\left(\frac{V1(y) - y_9}{R_{sub}} - y_{10} \right)$$

$$\dot{y}_{10} = \frac{1}{L_{sob}}\left(y_9 - y_{10} R_{sob} - y_{11} \right)$$

$$\dot{y}_{11} = \frac{1}{c_{dsb}}\left(y_{10} - \frac{y_{11} - y_{25}}{R_{dsb}} \right)$$

$$\dot{y}_{12} = \frac{1}{c_{cob}}\left(\frac{V1(y) - y_{12}}{R_{carotid}} - y_{13} \right)$$

$$\dot{y}_{13} = \frac{1}{L_{cob}}\left(y_{12} - y_{13} R_{cob} - y_{14} \right)$$

$$\dot{y}_{14} = \frac{1}{c_{dcb}}\left(y_{13} - \frac{y_{14} - y_{25}}{R_{dcb}} \right)$$

$$\dot{y}_{15} = \frac{1}{c_{rlung}}\left(\frac{y_{21} - y_{15}}{R_{rpa}} - y_{16} \right)$$

$$\dot{y}_{16} = \frac{1}{L_{rlung}}\left(y_{15} - y_{16} R_{rlung} - y_{17} \right)$$

$$\dot{y}_{17} = \frac{1}{c_{rpvb}}\left(y_{16} - \frac{y_{17} - y_0}{R_{rpvb}} \right)$$

$$\dot{y}_{18} = \frac{1}{c_{Llung}}\left(\frac{y_{22} - y_{18}}{R_{lpa}} - y_{19} \right)$$

$$\dot{y}_{19} = \frac{1}{L_{Llung}}\left(y_{18} - y_{19}R_{Llung} - y_{20}\right)$$

$$\dot{y}_{20} = \frac{1}{c_{lpvb}}\left(y_{19} - \frac{y_{20} - y_0}{R_{lpvb}}\right)$$

$$\dot{y}_{21} = \frac{1}{c_{rpa}}\left(\frac{V2(y) - y_{21}}{R_{rpa2}} - \frac{y_{21} - y_{15}}{R_{rpa}}\right)$$

$$\dot{y}_{22} = \frac{1}{c_{rpa}}\left(\frac{V2(y) - y_{22}}{R_{lpa2}} - \frac{y_{22} - y_{18}}{R_{lpa}}\right)$$

$$\dot{y}_{23} = \frac{1}{c_{ivc}}\left(\frac{y_6 - y_{23}}{R_{lbvb}} - y_{24}\right)$$

$$\dot{y}_{24} = \frac{1}{L_{ivc}}\left(y_{23} - y_{24}R_{ivc} - V2(y)\right)$$

$$\dot{y}_{25} = \frac{1}{c_{svc}}\left(\frac{y_{11} - y_{25}}{R_{dsb}} + \frac{y_{14} - y_{25}}{R_{dcb}} - y_{26}\right)$$

$$\dot{y}_{26} = \frac{1}{L_{svc}}\left(y_{25} - y_{26}R_{svc} - V2(y)\right)$$

$$\dot{y}_{27} = \frac{1}{c_G}\left(\frac{y_2 - y_{27}}{R_G} - y_{28}\right)$$

$$\dot{y}_{28} = \frac{1}{L_G}\left(y_{27} - y_{28}R_{ijs} - V2(y)\right)$$

$$I_{in} = \frac{y_{17} - y_0}{R_{rpvb}} + \frac{y_{20} - y_0}{R_{lpvb}} + \frac{y_8 - y_0}{R_{corvb}}$$

$$V1(y) = \frac{y_3 + \frac{y_4}{R_{da}} + \frac{y_9}{R_{sub}} + \frac{y_7}{R_{cora}} + \frac{y_{12}}{R_{carotid}}}{\frac{1}{R_{da}} + \frac{1}{R_{sub}} + \frac{1}{R_{cora}} + \frac{1}{R_{carotid}}}$$

$$V2(y) = \frac{y_{26} + y_{24} + y_{28} + \frac{y_{22}}{R_{lpa2}} + \frac{y_{21}}{R_{rpa2}}}{\frac{1}{R_{lpa2}} + \frac{1}{R_{rpa2}}}$$

If it is open loop

$$\dot{y}_{21} = \frac{1}{c_{rpa}}\left(VTrpa(t) - \frac{y_{21} - y_{15}}{R_{rpa}}\right)$$

$$\dot{y}_{22} = \frac{1}{c_{rpa}}\left(VTlpa(t) - \frac{y_{22} - y_{18}}{R_{lpa}}\right)$$

$$\dot{y}_{24} = \frac{1}{L_{ivc}}\left(y_{23} - VTivc(t)\right)$$

$$\dot{y}_{26} = \frac{1}{L_{svc}}\left(y_{25} - VTsvc(t)\right)$$

$$\dot{y}_{28} = \frac{1}{L_G}\left(y_{27} - VTijs(t)\right)$$

Simple IJS Circuit

ODEs

$$\dot{y}_0 = \frac{1}{c_{ra}}\left(I_{in} - \frac{y_0 - y_1}{R_{tric}} Hev \right)$$

$$\dot{y}_1 = \frac{1}{c_{rv(t)}}\left(\frac{y_0 - y_1}{R_{tric}} Hev - y_1 \frac{dc_{rv(t)}}{dt} - \frac{y_1 - y_2}{R_{pv}} Hev \right)$$

$$\dot{y}_2 = \frac{1}{c_{ao}}\left(\frac{y_1 - y_2}{R_{pv}} Hev - \frac{y_2 - y_{12}}{R_{G1}} - y_3 \right)$$

$$\dot{y}_3 = \frac{1}{L_{ao}}\left(y_2 - y_3 R_{ao} - V1(y) \right)$$

$$\dot{y}_4 = \frac{1}{c_{sys1}}\left(\frac{V1(y) - y_4}{R_{sub}} - y_5 \right)$$

$$\dot{y}_5 = \frac{1}{L_{sys}}\left(y_4 - y_5 R_{sys1} - y_6 \right)$$

$$\dot{y}_6 = \frac{1}{c_{sys2}}\left(y_5 - \frac{y_6 - y_7}{R_{sys2}} \right)$$

$$\dot{y}_7 = \frac{1}{c_{con}}\left(\frac{y_6 - y_7}{R_{sys2}} - \frac{y_7 - V2(t)}{R_{in}} \right)$$

$$\dot{y}_8 = \frac{1}{c_{lung}}\left(\frac{V2(y) - y_8}{R_{out}} - \frac{y_8 - y_9}{R_{lung}} \right)$$

$$\dot{y}_9 = \frac{1}{c_{pvb}}\left(\frac{y_8 - y_9}{R_{lung}} - \frac{y_9 - y_0}{R_{pvb}} \right)$$

$$\dot{y}_{10} = \frac{1}{c_{corab}}\left(\frac{V1(y) - y_{10}}{R_{cora}} - \frac{y_{10} - y_{11}}{R_{corab}} \right)$$

$$\dot{y}_{11} = \frac{1}{c_{corvb}}\left(\frac{y_{10} - y_{11}}{R_{corab}} - \frac{y_{11} - y_0}{R_{corvb}} \right)$$

$$\dot{y}_{12} = \frac{1}{c_{graft}}\left(\frac{y_2 - y_{12}}{R_{G1}} - \frac{y_{12} - V2(y)}{R_{G2}} \right)$$

$$I_{in} = \frac{y_{17} - y_0}{R_{rpvb}} + \frac{y_{20} - y_0}{R_{lpvb}} + \frac{y_8 - y_0}{R_{corvb}}$$

$$V1(y) = \frac{y_3 + \frac{y_{10}}{R_{cora}} + \frac{y_4}{R_{sub}}}{\frac{1}{R_{sub}} + \frac{1}{R_{cora}}}$$

$$V2(y) = \frac{\frac{y_7}{R_{in}} + \frac{y_{12}}{R_{G2}} + \frac{y_8}{R_{out}}}{\frac{1}{R_{out}} + \frac{1}{R_{in}} + \frac{1}{R_{G2}}}$$

If it is open loop

$$\dot{y}_7 = \frac{1}{c_{con}}\left(\frac{y_6 - y_7}{R_{sys2}} - iTin \right)$$

$$\dot{y}_8 = \frac{1}{c_{lung}}\left(iTout - \frac{y_8 - y_9}{R_{lung}} \right)$$

$$\dot{y}_{12} = \frac{1}{c_{graft}}\left(\frac{y_2 - y_{12}}{R_{G1}} - iTijs\right)$$

Full Fontan Circuit (Closed Loop)

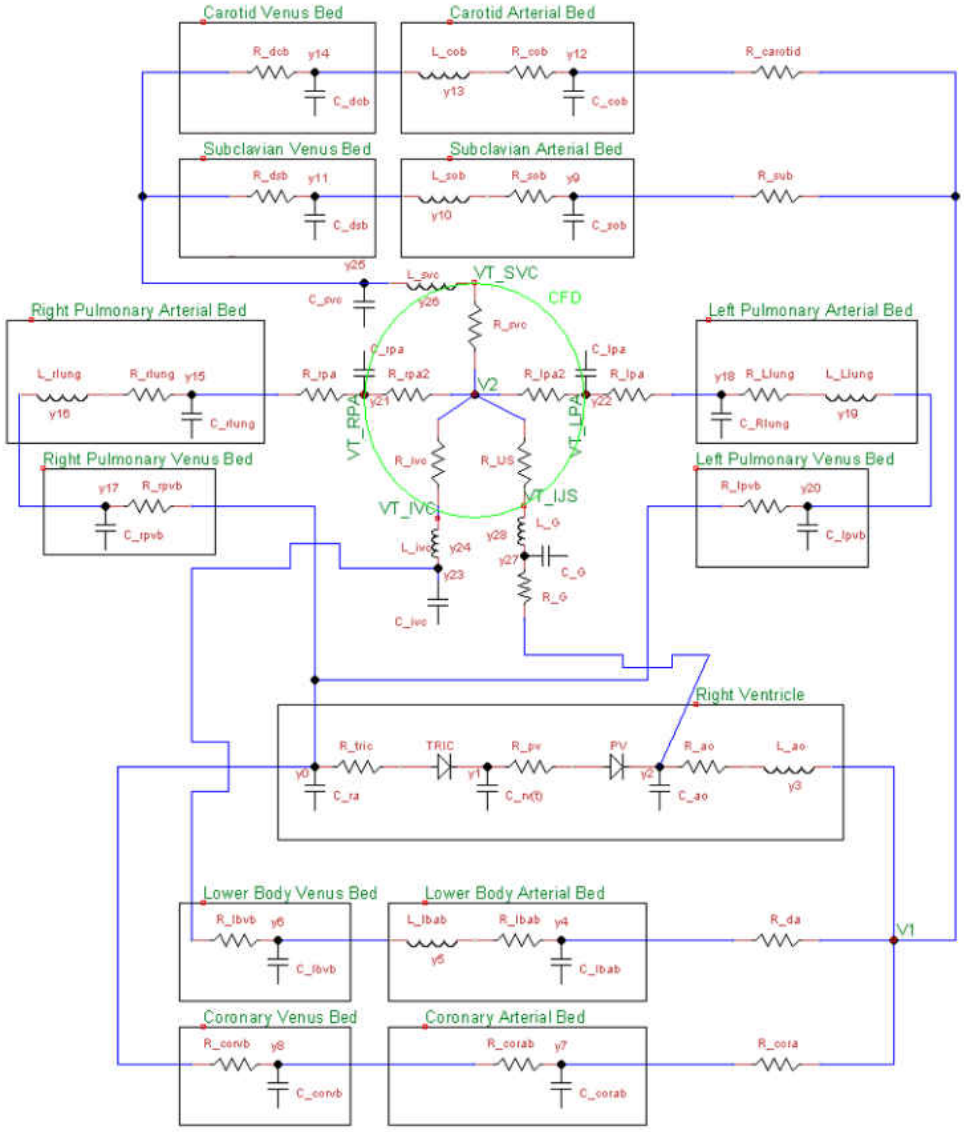

Figure 84: Full Fontan Circuit Diagram (Closed Loop).

Full Fontan Circuit (Open Loop)

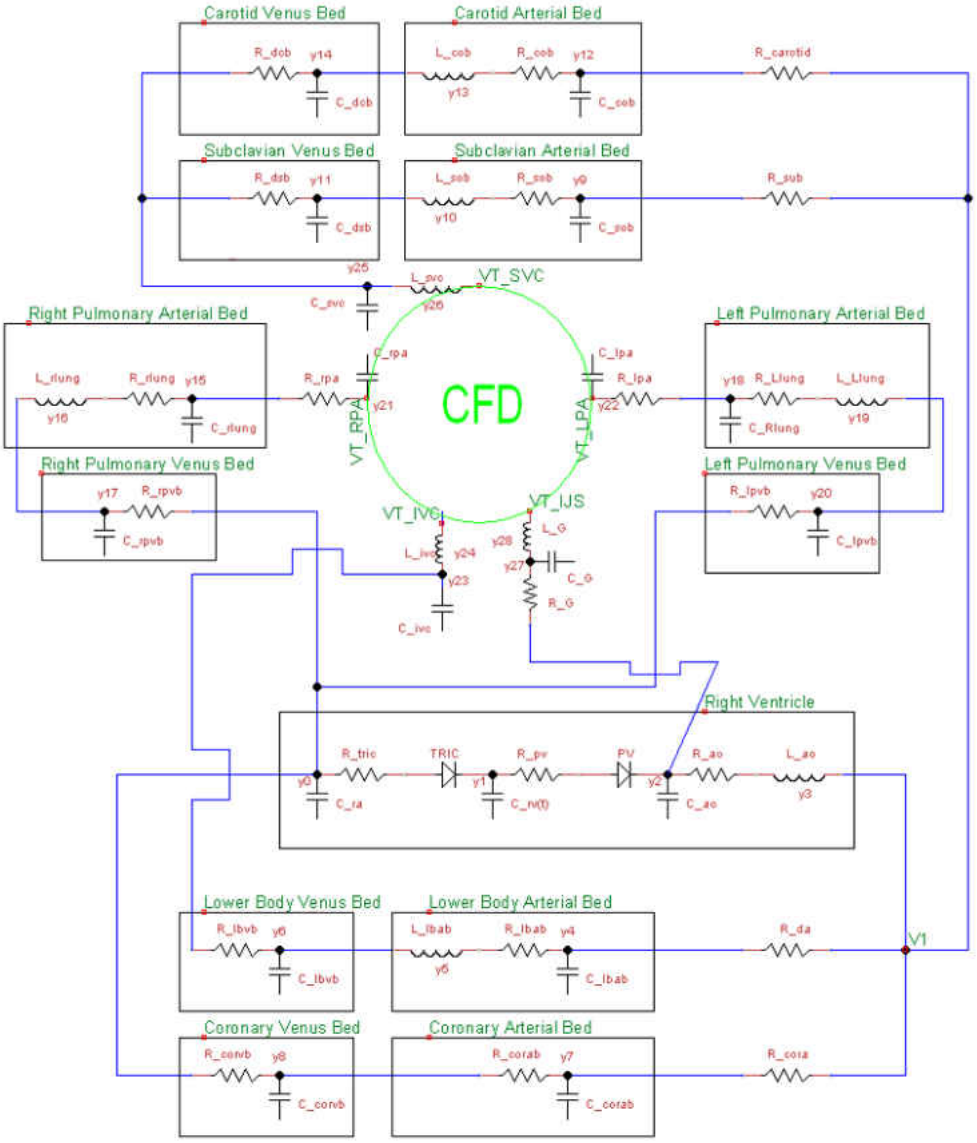

Figure 85: Full Fontan Circuit Diagram (Open Loop).

Table 17: Full Fontan Circuit Parameters for the Multi-Scale Models.

Full Fontan Circuit Parameters							
Parameter	Synthetic	CHOP-1	CHOP-6	Parameter	Synthetic	CHOP-1	CHOP-6
C_RA	0.13605442	0.26666667	0.13605442	R_AO	0.15	0.1125	0.15
C_AO	0.03324384	0.05402124	0.03324384	R_LBAB	4.213434	1.0533585	2.808956
C_LBAB	0.06206	0.161356	0.06206	R_LBVB	0.486234	0.1215585	0.324156
C_LBVB	1.69362	4.403412	1.69362	R_SOB	14.004478	4.9715897	9.8031346
C_CORAB	0.001554808	0.002526563	0.001554808	R_DSB	1.62078	0.5753769	1.134546
C_CORVB	0.020810768	0.033817498	0.020810768	R_COB	14.004478	4.9715897	9.8031346
C_SOB	0.0708736	0.1727544	0.0708736	R_DCB	1.62078	0.5753769	1.134546
C_DSB	0.87784	2.139735	0.87784	R_RLUNG	1.000512	0.148224	0.83376
C_COB	0.0708736	0.1727544	0.0708736	R_LLUNG	1.000512	0.18528	0.83376
C_DCB	0.87784	2.139735	0.87784	R_LPVB	0.026328	0.004388	0.02194
C_RLUNG	0.016312	0.0344591	0.016312	R_RPVB	0.026328	0.004388	0.02194
C_LLUNG	0.016312	0.0344591	0.016312	R_LPA	0.02	0.02	0.02
C_LPVB	0.355	0.7499375	0.355	R_RPA	0.02	0.02	0.02
C_RPVB	0.355	0.7499375	0.355	R_SVC	0.01	0.004937	0.01
C_IVC	0.008	0.007142857	0.008	R_IVC	0.01	0.001721	0.01
C_SVC	0.008	0.007142857	0.008	R_LPA2	0.019	0.020159	0.019
C_LPA	0.005	0.0005	0.005	R_RPA2	0.019	0.016308	0.019
C_RPA	0.005	0.005	0.005	R_IJS	0.0736	0.035633	0.0936
C_G	0.00005	0.000001	0.00005	R_G	1000	1000	1000
L_AO	0.003	0.0015	0.003	R_DA	0.389	0.389	0.389
L_LBAB	0.01069	0.018173	0.01069	R_SUB	0.35726525	0.053589788	0.35726525
L_SOB	0.02138	0.03207	0.02138	R_CAROTID	0.68283688	0.10242553	0.68283688
L_COB	0.02138	0.03207	0.02138	R_CORA	0.39	0.39	0.39
L_RLUNG	0.01	0.01	0.01	R_TRIC	0.0001	0.0001	0.0001
L_LLUNG	0.01	0.01	0.01	R_PV	0.03	0.03	0.03
L_IVC	0.005	0.001	0.005				
L_SVC	0.005	0.001	0.005				
L_G	0.05	0.001	0.05				

Table 18: Full Fontan Initial Conditions for the Multi-Scale Models

Full Fontan Initial Conditions			
Ics	Synthetic	CHOP-1	CHOP-6
y0	3.818249398	6.985832903	3.873322806
y1	3.815620047	6.978260165	3.870595295
y2	63.75235219	58.00561355	47.27273107
y3	2.151378676	4.301882321	1.961418799
y4	61.31539428	50.83839895	44.99359436
y5	9.350576099	27.83642282	8.554609901
y6	22.07101531	22.58618003	21.15801299
y7	63.32838618	57.0865857	46.94553261
y8	62.33153382	55.15263979	46.48695699
y9	64.06932849	57.91131049	47.57244584
y10	2.983381005	6.846550634	2.662946288
y11	22.38893912	24.37351552	21.59387505
y12	64.69422901	58.25890956	48.12615073
y13	3.035948141	6.925728988	2.730388788
y14	22.28066841	24.33300084	21.49002772
y15	15.01898423	13.88678008	15.20596589
y16	10.93832039	47.74019296	13.30530878
y17	4.09420928	7.172636014	4.153433795
y18	15.01898423	14.05317941	15.20596589
y19	10.93832039	39.01602664	13.30530878
y20	4.09420928	7.134280591	4.153433795
y21	15.23753358	14.84254259	15.47143828
y22	15.23753358	14.83441178	15.47143828
y23	15.56292447	15.66567065	15.85040347
y24	13.39112102	56.93160793	16.39130348
y25	15.52562576	15.75637806	15.81988239
y26	8.408406101	29.88258765	10.10401918
y27	15.44499271	15.62335534	15.72350861
y28	0.048358803	0.042382187	0.03165695

Simple IJS Circuit (Closed Loop)

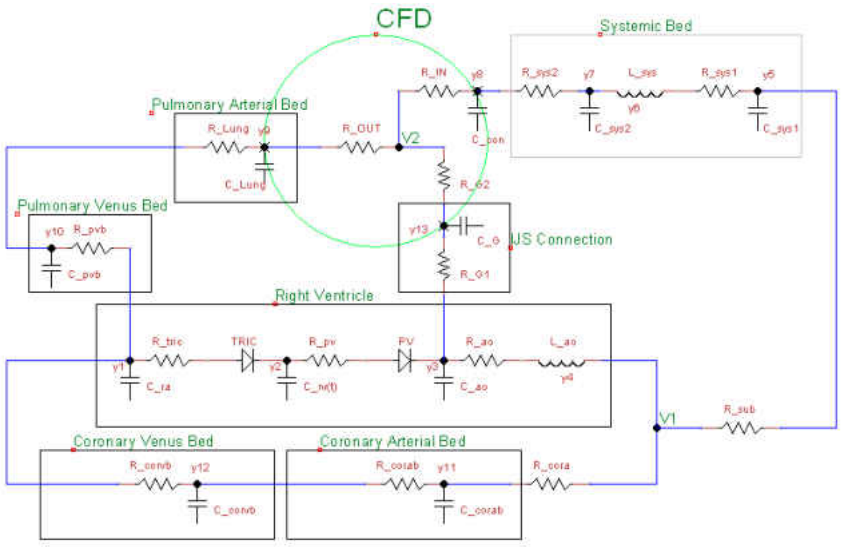

Figure 86: Simple IJS Circuit Diagram.

Table 19: Simple IJS Circuit Parameters and Initial Conditions for Multi-Scale Model Testing.

Simple IJS Circuit Parameters and Initial Conditions			
Circuit Parameter		Initial Conditions	
C_RA	0.1361	y0	3.18410354
C_AO	0.04155	y1	3.18204452
C_CORAB	0.001944	y2	46.6752387
C_CORVB	0.02601	y3	-0.3668062
C_SYS1	1.97736	y4	47.0389677
C_CON	0.01	y5	15.0807544
C_SYS2	1.97736	y6	29.6648819
C_LUNG	0.01019	y7	9.58572088
C_PVB	0.4437	y8	9.36864529
C_GRAFT	0.05	y9	3.47849281
L_AO	0.003	y10	46.3586825
L_SYS	0.02138	y11	43.6873975
L_LUNG	0.001	y12	12.5326821
R_TRIC	0.0001		
R_PV	0.03		
R_AO	0.15		
R_CORA	0.39		
R_SUB	0.2345		
R_SYS1	1.16101		
R_SYS2	1.16101		
R_LUNG	0.3209		
R_PVB	0.01646		
R_G1	50		

APPENDIX D: FLUID REGION EXTRACTION

Animation of CFD Results Using Blender

This section details the procedure for creating animated videos with Blender from scene pictures taken using StarCCM+. StarCCM+ has animation capabilities, but the options are limited. Blender has a wide variety of tools to help control animation quality, video output compression, and animation frames per second. The procedure for creating videos from scene pictures are as follows:

- Open Blender and navigate to the “Video Sequence Editor”.
- Press “Shift + a” and select image.
- Navigate to the location of the pictures to be animated and import these pictures.
- Use the “Output” tab on the right pane to edit video output parameters such as frames per second (FPS), video compression, frames to be used, etc.
- Control the playback length by editing FPS and frames to be used.
- Select the location that the video should be saved to and click “Animate”.

NOTES: For our animations, we gathered 50 pictures for each heart cycle and set the FPS to 10. These parameters created 5 second videos.

Smoothing a Rough Surface Mesh Using Blender

Patient-specific geometry models are created by gathering surface data from MRI scans. In most cases, the surface that is extracted from these scans are rough or jagged. Blender can be used to smooth these surfaces out before being imported into SolidWorks for fluid region construction (creating a fluid region from the surface mesh). The procedure is explained below:

- Import an STL or other surface mesh file into Blender.

- Clean the model by removing any extra detached surfaces. Select any cell on the surface that is being kept and use “Inverse Selection” to select and delete detached surfaces.
- Navigate to edit mode and select the wrench tool in the right pane.
- Add a smoothing modifier and edit the repeater until desired model is achieved.
- Export to STL (this is a SolidWorks and StarCCM+ compatible file).

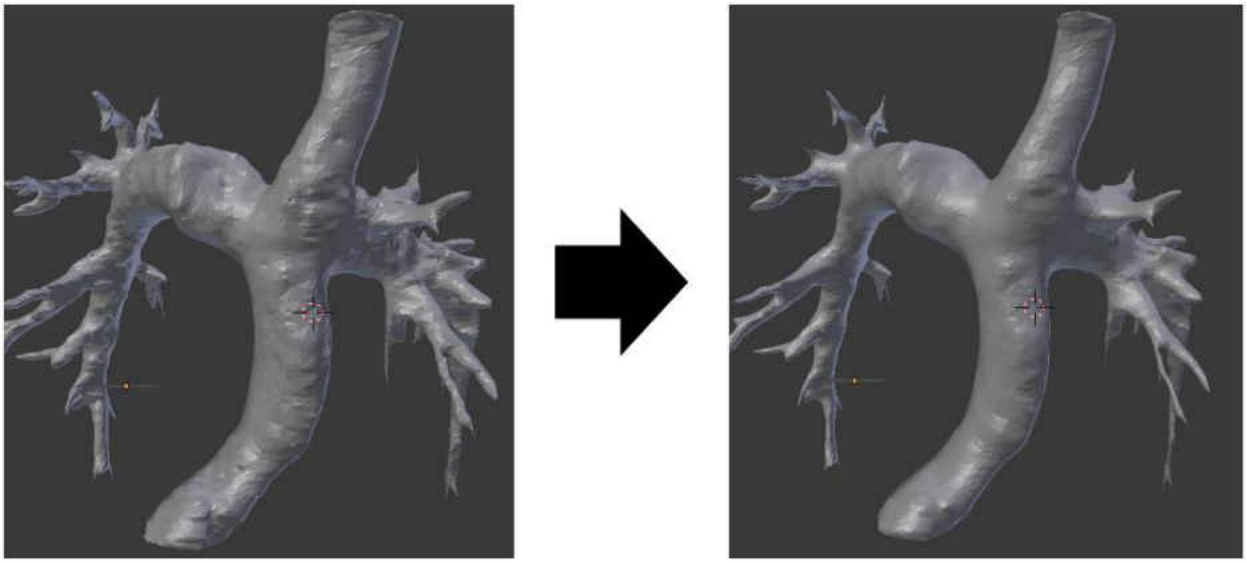

Figure 87: Smoothing of the CHOP-6 Model Using Blender. Left:Rough Model Imported from CT Scans. Right:Blender Smoothed CHOP 6 Model.

Extracting Fluid Region from Surface Mesh Files Using SolidWorks

This section provides a method to extract the fluid volume from the STL model created by the Blender smoothing technique mentioned in section 3.1.3. Getting the fluid region in SolidWorks allows the user to create of many different configurations efficiently. This technique was used to attach different IJS configurations to the patient-specific model quickly and efficiently. The procedure is outlined below:

- Import the mesh surface into SolidWorks.
- Use the curve wizard to make cuts along the desired profile.
- Edit these curves to smooth out any jagged edges.
- Loft across desired profiles and repeat for the entire model.

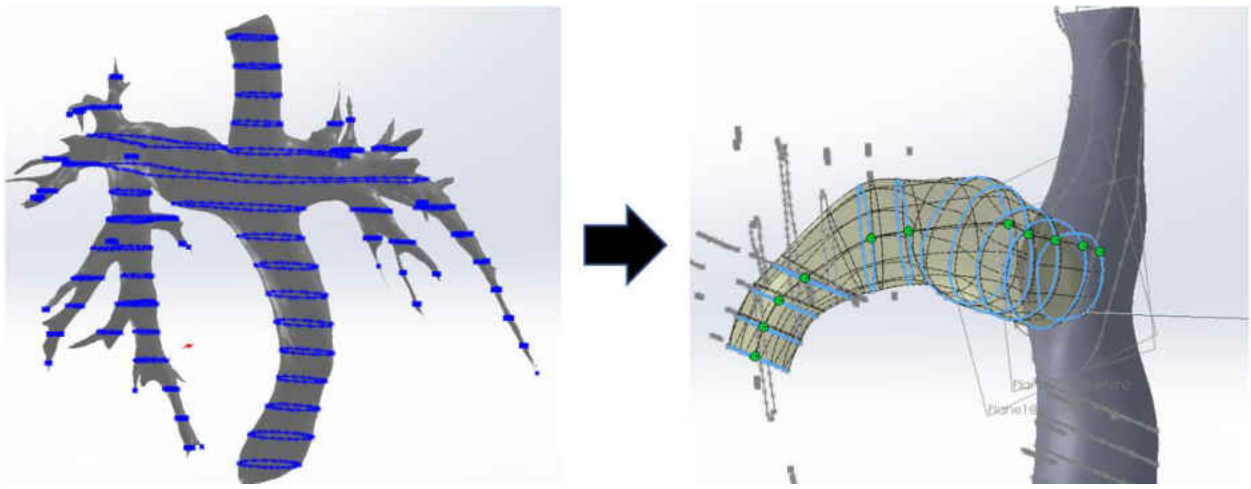

Figure 88: Fluid Region Construction on CHOP 6 Using SolidWorks. Left:Curve Cuts Using Curve Wizard. Right:Lofting Across the Curve Cuts.

REFERENCES

[1] Ceballos A, Argueta-Morales R, Divo E, Osorio R, Caldarone C, Kassab A, and DeCampli W. Computational Analysis of Hybrid Norwood Circulation with Distal Aortic Arch Obstruction and Reverse Blalock-Taussig Shunt *Ann. Thoracic Surgery.* 2012; 94: 1540-1550.

[2] Ceballos A, Divo E, Argueta-Morales R, Calderone C, Kassab A, and DeCampli W. A Multi-Scale CFD Analysis of the Hybrid Norwood Palliative Treatment for Hypoplastic Left Heart Syndrome: effect of the reverse Blalock-Taussig shunt diameter. *ASME 2013 IMECE*, vol. 3B: Biomedical and Biotechnoly Engineering.

[3] Migliavacca F, Kilner P, Pennati G, Dubini G, Pietrabissa R, Fumero R, and de Leval M. Computational Fluid Dynamic and Magnetic Resonance Analyses of Flow Distribution Between the Lungs After Total Cavopulmonary Connection. *IEEE Transactions on Biomedical Engineering.* 1999; 46: 393-399.

[4] Alexi-Meskishvili V, Ovroutski S, Ewert P, Dahnert I, Berger F, Lange P, and Hetzer R. Optimal conduit size or extracardiac Fontan Operation. *European Journal of Cardio-thoracic Surgery.* 2000; 18: 690-695.

[5] de Leval M, Dubini G, Migliavacca F, Jalali H, Camporini G, Redington A, and Pietrabissa R. Use of Computational Fluid Dynamics in the Design of Surgical Procedures: Application to the Study of Competitive Flows in Cavopulmonary Connections. *Thoracic and Cardiovascular Surgery.* 1996; 111: 502-513.

[6] Hsia T, Migliavacca F, Pittaccio S, Radaelli A, Dubini G, Pennati G, and de Leval M. Computational Fluid Dynamic Study of Flow Optimization in Realistic Models of the Total Cavopulmonary Connections. *Journal of Surgical Research.* 2004; 116: 305-313.

[7] Itatani K, Miyaji K, Tomoyasu T, Nakahata Y, Kuniyoshi O, Takamoto S, and Ishii M. Optimal Conduit Size of the Extracardiac Fontan Operation Based on Energy Loss and Flow Stagnation. *The Society of Thoracic Surgions*. 2009; 88: 565-573.

[8] Greenfield J and Fry D. Relationship Between Instantaneous Aortic Flow and the Pressure Gradient. *Circulation Research*. 1965; 17: 340-348.

[9] Kroll M, Hellums D, McIntire L, Schafer A, and Moake J. Platelets and Shear Stress. *The Journal of the American Society of Hematology*. 1996; 88: NO 5, 1525-1541.

[10] Mardsen A, Vignon-Clementel I, Chan F, Feinstein J, and Taylor C. Effects of Exercise and Respiration on Hemodynamic Efficiency in CFD Simulations of the Total Cavopulmonary Connection. *Annals of Biomedical Engineering.* 2007; 35: 250–263.

[11] Long C, Hsu M, Bazilevs Y, Feinstein J, and Marsden A. Fluid–structure interaction simulations of the Fontan procedure using variable wall properties. *Int. J. Numer. Meth. Biomed. Engng*. 2012; 28: 513–527.

[12] CD-Adapco a Siemens Business, StarCCM+ 11.04.010 User Guide, 2016.

[13] Argueta-Morales R, Tran R, Ceballos A, Osorio R, Clark W, Divo E, Kassab A, and DeCampli W. Mathematical modeling of patient-specific ventricular assist device implantation to reduce particulate embolization rate to cerebral vessels. *Journal of Biomechanical Egineering*. 2014; 136(7): 8.

[14] Quarteroni A, Ragni S, and Veneziani A. Coupling between lumped and distributed models for blood flow problems. *Computing and Visualization in Science*. 2001; 4: 111-124.

[15] Esmaily-Moghadam M, Hsia T, and Mardsen A. The assisted bidirectional Glenn: A novel surgical approach for first-stage single-ventricle heart palliation. *The Journal of Thoracic and Cardiovascular Surgery*; 149: 699-705.

[16] Bove E, Migliavacca F, de Leval M, Balossino R, Pennati G, Lloyd T, Khambadkone S, Hsia T, and Dubini G. Use of mathematical modeling to compare and predict hemodynamics effects of the modified Blalock-Taussig and right ventricle-pulmonary artery shunts for hypoplastic left heart syndrome. *The Journal of Thoracic and Cardiovascular Surgery*; 136: 312-320.

[17] Hsia T, Cosentino D, Corsini C, Pennati G, Dubini G, and Migliavacca F. Use of mathematical modeling to compare and predict hemodynamic effects between hybrid and surgical Norwood palliations for hypoplastic left heart syndrome. *Circulation.* 2011; 124: S204-S210.

[18] Schiavazzi D, Kung E, Mardsen A, Baker C, Pennati G, Hsia T, Hlavacek A, and Dorfman A. Hemodynamic effects of left pulmonary artery stenosis after superior cavopulmonary connection: A patient-specific multiscale modeling study. *The Journal of Thoracic and Cardiovascular Surgery*. 2015; 149: 689-696.

[19] Esmaily-Moghadam M, Bazilevs Y, and Mardsen A. A new preconditioning technique for implicitly coupled multidomain simulations with applications to hemodynamics. *Comput Mech*. 2013; 52: 1141-1152.

[20] Quarteroni A, and Veneziani A. Analysis of a geometrical multiscale model based on the coupling of ODEs and PDEs for blood flow simulations. *Multiscale Model. Simul*. 2003; 1: 173-195.

[21] Esmaily-Moghadam M, Bazilevs Y, Hsia T, Vignon-Clementel I, and Mardsen A. A comparison of outlet boundary treatments for prevention of backflow divergence with relevance to blood flow simulations. *Comput Mech*. 2011; 48: 277-291.

[22] Lagana K, Balossino R, Migliavacca F, Pennati G, Bove E, de Leval M, and Dubini G. Multiscale modeling of the cardiovascular system: application to the study of pulmonary and coronary perfusions in the univentricular circulation. *Journal of Biomechanics*. 2005; 38: 1129-1141.

[23] Sankaran S, Moghadam M, Kahn A, Tseng E, Guccione J, and Mardsen A. Patient-specific multiscale modeling of blood flow for coronary artery bypass graft surgery. *Annals of Biomedical Engineering.* 2012; 40: 2228-2242.

[24] Shachar G, Fuhrman B, Wang Y, Lucas R, and Lock J. Rest and exercise hemodynamics after the Fontan procedure. *Circulation*. 1982; 65: 1043-1048.

[25] Graham R, Skoog C, Oppenheimer L, Rabson J, and Goldberg H. Critical closure in the canine pulmonary vasculature. *Circulation Research*. 1982; 50: 566-572.

[26] Gewillig M. Congenital heart disease the Fontan circulation. *Heart. 2005*; 91: 839-846.

[27] Gewillig M, Brown S, Eyskens B, Heying R, Ganame J, Budts W, Gerche A, and Gorenflo M. State-of-the-art congential the Fontan circulation: who controls the cardiac output? *Interactive CardioVascular and Thoracic Surgery*. 2010; 10: 428-433.

[28] Gewillig M, and Brown S. The Fontan circulation after 45 years: update in physiology. *Heart*. 2016; 102: 1081-1086.

[29] Naeije R, and Chesler N. Pulmonary circulation at exercise. *Compr Physiol*; 2(1): 711-741.

[30] Henaine R, Vergnat M, Bacha E, Baudet B, Lambert V, Belli E, and Serraf A. Effects of lack of pulsatility on pulmonary endothelial function in the Fontan circulation. *J Thorac Cardiovasc Surg.* 2013; 146: 522-9.

[31] Mori H, Park I, Yamagishi H, Nakamura M, Ishikawa S, Takigiku K, Yasukochi S, Nakayama T, Saji T, and Nakaishi T. Sildenafil reduces pulmonary vascular resistance in single ventricular physiology. *International Journal of Cardiology.* 2016; 221: 122-127.

[32] Goldstein B, Connor C, Gooding L, and Rocchini A. Relation of systemic venous return, pulmonary vascular resistance, and diastolic dysfunction to exercise capacity in patients with single ventricle receiving Fontan palliation. *Am J Cardiol.* 2010; 105: 1169-1175.

[33] Reeves J, Linehan J, and Stenmark K. Distensibility of the normal human lung circulation during exercise. *Am J Physiol Lung Cell Mol Physiol.* 2005; 288: L419-L425.

[34] Schmitt B, Steendijk P, Ovroutski S, Lunze K, Rahmanzadeh P, Maarouf N, Ewert P, Berger F, and Kuehne T. Pulmonary vascular resistance, collateral flow, and ventricular function in patients with a Fontan circulation at rest and during Dobutamine stress. *Circ Cardiovasc Imaging.* 2010; 3: 623-631.

[35] Rivera I, Mendonca M, Andrade J, Moises V, Campos O, Silva C, and Carvalho A. Pulmonary venous flow index as a predictor of pulmonary vascular resistance variability in congenital heart disease with increased pulmonary flow: A comparative study before and after oxygen inhalation. *Echocardiography*. 2013; 30: 952-960.

[36] Forton K, Motohi Y, Deboeck G, Faoro V, and Naeije R. Effects of body position on exercise capacity and pulmonary vascular pressure-flow relationships. *J Appl Physiol*. 2016; 121: 1145-1150.

[37] Grosse-Wortmann L, Dragulescu A, Drolet C, Charturvedi R, Kotani Y, Mertens L, Taylor K, Rotta g, Arsdell G, Redington A, and Yoo S. Determinants and clinical significance of flow via the fenestration in the Fontan pathway: A multimodial study. *International Journal of Cardiology*. 2013; 168: 811-817.

[38] Gewillig M, and Goldberg D. Failure of the Fontan circulation. *Heart Failure Clin*. 2014; 10: 105-116.

[39] Rodefeld M, Frankel S, and Giridharan G. Cavopulmonary assist: (Em)powering the univentricular Fontan circulation. *Semin Thorac Cardiovasc Surg Pidiatri Card Surg Annu*. 2011; 14: 45-54.

[40] Delorme Y, Anupindi K, Kerlo A, Shetty D, Rodefeld M, Chen J, and Frankel S. Large eddy simulation of powered Fontan hemodynamics. *Journal of Biomechanics*. 2013; 46: 408-422.

[41] Corno A, Vergara C, Subramanian C, Johnson R, Passerini T, Veneziani A, Formaggia L, Alphonso N, Quarteroni A, and Jarvis J. Assisted Fontan procedure: animal and in vitro models and computational fluid dynamics study. *Interactive CardioVascular and Thoracic Surgery*. 2010; 10: 679-684.

[42] Valdovinos J, Shkolyar E, Carman G, and Levi D. In vitro evaluation of an external compression device for Fontan mechanical assistance. *Artificial Organs*. 2014; 38(3): 199-207.

[43] Pekkan K, Frakes D, Zelicourt D, Lucas C, Parks J, and Yoganathan A. Coupling pediatric ventricle assist devices to the Fontan circulation: Simulations with a lumped-parameter model. *ASAIO Journal*. 2005; 51: 618-628.

[44] Northvale Korting, Venturi/Fluid Jet, http://www.northvalekorting.co.uk/venturi-fluid-jet .

[45] Itatani K, Miyaji K, Qian Y, Liu J, Miyakoshi T, Murakami A, Ono M, and Umeza M. Influence of surgical arch reconstruction methods on single ventricle workload in the Norwood procedure. *J Thorac Cardiovasc Surg*. 2012; 144: 130-138.

[46] Kung E, Baretta A, Baker C, Arbia G, Biglino G, Corsini C, Schievano S, Vignon-Clementel I, Dubini G, Pennati G, Taylor A, Dorfman A, Hlavacek A, Mardsen A, Hsia T, and Migliavacca F. Predicitive modeling of the virtual Hemi-Fontan operation for second stage single ventricle palliation: Two patient-specific cases. *Journal of Biomechanics*. 2013; 46: 423-429.

[47] Bove E, de Leval M, Migliavacca F, Balossino R, and Dubini G. Toward optimal hemodynamics: computer modeling of the Fontan circuit. *Pediatr Cardiol*. 2007; 28: 477-481.

[48] Luo C, Ramachandran D, Ware D, Ma T, and Clark J. Modeling left ventricular diastolic dysfunction: classification and key indicators. *Theoretical Biology and Medical Modelling*. 2011; 8: 14.

[49] Mardsen A, Bernstein A, Reddy V, Shadden S, Spilker R, Chan F, Taylor C, and Feinstein J. Evaluation of a novel Y-shaped extracardiac Fontan baffle using computational fluid dynamics. *J Thorac Cardiovasc Surg*. 2009; 137: 394-403.

[50] Whitehead K, Pekkan K, Kitajima H, Paridon S, Yoganathan A, and Fogel M. Nonlinear power loss during exercise in single-ventricle patients after the Fontan : insights from computational fluid dynamics. *Circulation.* 2007; 116: I-165-I-171.

[51] De Zelicourt D, Mardsen A, Fogel M, and Yoganathan. Imaging and patient specific simulations for the Fontan surgery: Current methodologies and clinical applications. *Progress in Pediatric Cardiology*, 2010; 30: 31-44.

[52] Sundareswaren K, Zelicourt D, Pekkan K, Jayaprakash G, Kim D, Whited B, Rossignac J, Fogel M, Kanter K, and Yoganathan A. Anatomically Realistic Patient-Specific Surgical Planning of Complex Congenital Heart Defects Using MRI and CFD. *Proceedings of the 29th Annual International Conference of the IEEE EMBS*, August 23—26, 2007.

[53] Socci L, Gervaso F, Migliavacca F, Pennati G, Dubini G, Ait-Ali L, Festa P, Amoretti F, Scebba L, and Luisi V. Computational fluid dynamics ina model of the total cavopulmonary connection reconstructed using magnetic resonance images. *Cariol Young*. 2005; 15: 61-67.

[54] Bove E, de Leval M, Migliavacca F, Guadagni G, and Dubini G. Computational fluid dynamics in the evaluation of hemodynamic performance of cavopulmonary connections after the Norwood procedure for hypoplastic left heart syndrome. *J Thorac Cardiovasc Surg*. 2003; 126: 1040-7.

[55] Hijazi Z, Fahey J, Kleinman C, Kopf G, and Hellenbrand W. Hemodyanmic Evaluation Before and After Closure of Fenestrated Fontan: An Acute Study of Changes in Oxygen Delivery. *Circulation*. 1992; 86: 196-202.

[56] Moghadam M, Vignon-Clementel I, Figliola R, and Mardsen A. A modular numerical method for implicit 0D/3D coupling in cardiovascular finite element simulations. *Journal of Computational Physics*. 2013; 244: 63-79.

[57] Pagnamenta A, Fesler P, Vandinivit A, Brimioulle S, Naeije R. Pulmonary vascular effects of dobutamine in experimental pulmonary hypertension. *Crit Care Med*. 2003; 31: 1140-1146.

[58] Geleijnse M, Fioretti P, and Roelandt J. Methodology, Feasibility, Safety and Diagnostic Accuracy of Dobutamine Stress Echocardiography. *J Am Coll Cardiol*. 1997; 30: 595-606.

[59] Marshall H, Swan H, Burchell H, and Wood E. Effect of Breathing Oxygen on Pulmonary Artery Pressure and Pulmonary Vascular Resistance in Patients with Ventricular Septal Defect. *Circulation*. 1961; 23: 241-252.

[60] Zamir M, Sinclaor P, and Wonnacott T. Relation between diameter and flow in major branches of the arch of the aorta. *J. Biomech*. 1992; 25: 1303-1310.

[61] Shimizu S, Kawada T, Une D, Fukumitsu M, Turner M, Kamiya A, Shishido T, and Sugimachi M. Partial cavopulmonary assist from the inferior vena cava to the pulmonary artery improves hemodynamics in failing Fontan circulation: a theoretical analysis. *J Physiol Sci*. 2016; 66: 249-255.

[62] Kung E, Pennati G, Migliavacca F, Hsia T, Figliola R, Mardsen A, and Giardini A. A simulation Protocol for Exercise Physiology in Fontan Patients Using a Closed Loop Lumped-Parameter Model. *Journal of Biomechanical Engineering*. 2014; 136: 081007-1 to 081007-14.

[63] Houlind K, Stenbog E, Emmertsen K, Hansen O, Rybro L, and Hjortdal V. Pulmonary and caval flow dynamics after total cavopulonary connection. *Heart*. 1999; 81: 67-72.

[64] Kocyildirim E, Dur O, Soran O, Tuzun E, Miller M, Housler G, Wearden P, Fossum T, Morell V, and Pekkan K. Pulsatile venouse waveform quality in Fontan circulation-clinical implications, venous assist options and the future. *Anadolu Kardiyol Derg*. 2012; 12: 420-6.

[65] Petrofski J, Hoopes C, Bashore T. Mechanical ventricular support lowers pulmonary vascular resistance in a patient with congential heart disease. *Ann Thorac Surg*. 2003; 75: 1005-1007.

[66] Zhou J, Esmaily-Moghadam M, Conover T, Hsia T, Mardsen A, and Figliola R. In Vitro Assessment of the Assisted Bidirectional Glenn Procedure for Stage One Single Ventricle Repair. *Cardiovascular Engineering and Technology*. 2015; 6: 256-267.

[67] Fontan F, Baudet E. Surgical repair of tricuspid atresia. *Thorax*. 1971; 26: 240-8.

[68] Mukherjee D, Biswas M, and Mitra A. Hydrodynamics of Liquid-Liquid Dispersion in Ejectors and Vertical Two Phase Flow. *The Canadian Journal of Chemical Engineering.* 1988; 66: 896-907.

[69] Brahim A, Prevost M, and Bugarel R. Momentum Transfer in a Vertical Down Flow Liquid Jet Ejector: Case of Self Gas Aspiration and Emulsion Flow. *Int J Multiphase Flow*. 1984; 10: 79-94.

[70] Kandakure M, Gaikar V, and Patwardhan. Hydrodynamic aspects of ejectors. *Chemical Engineering Science*. 2005; 60: 6391-6402.

[71] Yadav R and Patwardhan A. Design aspects of ejectors: Effects of suction chamber geometry. *Chemical Engineering Science*. 2008; 63: 3886-3897.

[72] Hjortdal V, Emmertson K, Stenbog E, Frund T, Schmidt M, Kromann O, Sorensen K, and Pedersen E. Effects of Exercise and Respriation on Blood Flow in Total Cavopulmonary Connection: A Real-Time Magnetic Resonance Flow Study. *Circulation*. 2003; 108: 1227-1231.

[73] Petrofski J, Hoopes C, Bashmore T, Russel S, and Milano C. Mechanical Ventricular Support Lowers Pulmonary Vascular Resistance in a Patient With Congenital Heart Disease. *Ann Thorac Surg*. 2003; 75: 1005-1007.

[74] Tang B, Pickard S, Chan F, Tsao P, Taylor C, and Feinstein J. Wall shear stress is decreased in the pulmonary arteries of patients with pulmonary arterial hypertension: An image-based, computational fluid dynamics study. *Pulmonary Circulation*. 2012; 2: 470-476.

[75] Das A, Koury A, Tibbets J, Ni M, Divo E, Kassab A, and DeCampli W. Laboratory Development of a Self-Powered Fontan for Treatment of Congenital Heart Disease. *Proceedings of the 2nd Thermal and Fluid Engineering Conference, TFEC2017. 4th International Workshop on Heat Transfer, IWHT2017*. April 2-5, 2017, Las Vegas, NV, USA.